



Skolkovo Institute of Science and Technology

Skolkovo Institute of Science and Technology

PEROVSKITE MIXED OXIDES AS CATALYSTS OF OXYGEN EVOLUTION
REACTION
Doctoral Thesis

by

SERGEI V. POROKHIN

DOCTORAL PROGRAM IN MATERIALS SCIENCE AND ENGINEERING

Supervisor
Professor Artem M. Abakumov
Co-advisor
Assistant Professor Victoria A. Nikitina

Moscow - 2022

© Sergei Porokhin 2022

I hereby declare that the work presented in this thesis was carried out by myself at Skolkovo Institute of Science and Technology, Moscow, except where due acknowledgement is made, and has not been submitted for any other degree.

Candidate (Sergei Porokhin)

Supervisor (Prof. Artem Abakumov)

Abstract

Electrochemical water splitting is considered as a sustainable and ecologically friendly energy storage technology providing clean energy for the future. The materials containing 3d transition metals, such as Ni-Fe-based compounds, are a worthy alternative to precious metal-based electrocatalysts, showing promising catalytic activity for the oxygen evolution reaction (OER) in alkaline media. In this work, Ca-doped Ni/Fe-mixed perovskites were synthesized using ultrasonic spray pyrolysis technique. A modified approach of synthesis with sorbitol as fuel and ozone as oxidizer results in chemically homogeneous hollow spheres with specific surface area as high as $\sim 15 \text{ m}^2 \text{ g}^{-1}$. The crystal structure and the chemical composition were determined with powder X-ray diffraction, electron diffraction, aberration-corrected scanning transmission electron microscopy, energy-dispersive X-ray mapping, ^{57}Fe Mössbauer spectroscopy, iodometric titration and X-ray photoelectron spectroscopy. Being employed as a catalyst for OER in 1M NaOH, the $\text{La}_{0.6}\text{Ca}_{0.4}\text{Fe}_{0.7}\text{Ni}_{0.3}\text{O}_{2.9}$ perovskite demonstrates a superior specific and mass activities. The enhanced activity of $\text{La}_{0.6}\text{Ca}_{0.4}\text{Fe}_{0.7}\text{Ni}_{0.3}\text{O}_{2.9}$ compared to that of undoped $\text{LaFe}_{0.7}\text{Ni}_{0.3}\text{O}_3$ was rationalized from a comparison of DFT-calculated electronic structures. The Ca doping increases Ni and Fe oxidation states, enhances covalency of the Ni/Fe-O bonds, shifts the center of O 2p band closer to the Fermi level thus decreasing formation energy of the oxygen vacancies. This provokes faster leaching of A-site cations and restructuring of the surface layers of perovskite into Ni-Fe (oxy)hydroxides, which strongly interact with Fe ions in the electrolyte. As a result, the electrocatalytic activity of the perovskite materials is greatly enhanced. In order to assess the effect of the most

common impurity in alkaline electrolytes on the stability and activity of perovskite catalyst, OER experiments were conducted with the deliberate addition of Fe ions to the electrolyte followed by *ex situ* studies using transmission electron microscopy. The restructuring of the perovskite surface layer into $\text{Ni}_{0.5}\text{Fe}_{0.5}\text{O}_x(\text{OH})_{2-x}$ was discovered, as a result of interaction of Fe ions in electrolyte with the perovskite surface after the OER.

KEYWORDS: spray pyrolysis, oxygen evolution reaction, water splitting, perovskite, lattice oxygen mediated mechanism

Publications

1. Porokhin, S. V., Nikitina, V. A., Aksyonov, D. A., Filimonov, D. S., Pazhetnov, E. M., Mikheev, I. V., & Abakumov, A. M. Mixed-Cation Perovskite $\text{La}_{0.6}\text{Ca}_{0.4}\text{Fe}_{0.7}\text{Ni}_{0.3}\text{O}_{2.9}$ as a Stable and Efficient Catalyst for the Oxygen Evolution Reaction. *ACS Catalysis* 11.13 (2021): 8338-8348.
2. Porokhin S. V., Nikitina V. A., Abakumov A. M. Enhancement of Catalytic Activity and Stability of $\text{La}_{0.6}\text{Ca}_{0.4}\text{Fe}_{0.7}\text{Ni}_{0.3}\text{O}_{2.9}$ Perovskite with ppm Concentration of Fe in the Electrolyte for the Oxygen Evolution Reaction. *Materials* 14.21 (2021): 6403.

List of Conferences

1. Порохин С.В., «Синтез, структура, каталитические свойства $\text{La}_{1-x}\text{Ca}_x\text{Fe}_{0.7}\text{Ni}_{0.3}\text{O}_{3-\delta}$ и механизм реакции выделения кислорода» // Международная научная студенческая конференция MNSK 12-23 апреля 2021, Томск-Новосибирск, УДК 544.6. Online oral presentation.
2. Порохин С.В., Никитина В.А., Абакумов А.М., «Электрокатализаторы для реакции выделения кислорода в щелочной среде на основе перовскитов состава $\text{La}_{1-x}\text{Ca}_x\text{Fe}_{1-y}\text{Ni}_y\text{O}_{3-\delta}$ ($x=0, 0.3, 0.5; y=0.3, 0.5$)» // IV Российский конгресс по катализу 20-25 сентября 2021, Казань, Россия. Oral presentation.
3. S.V. Porokhin, V.A. Nikitina, E.R. Savinova, A.M. Abakumov, «Catalytic properties of perovskite composition $\text{La}_{1-x}\text{Ca}_x\text{Fe}_{0.7}\text{Ni}_{0.3}\text{O}_3$ for oxygen evolution reaction» // 15th international meeting fundamental problems of solid state ionics, 2020 November 30-December 07, Chernogolovka, Russia, book of abstracts, P-395. Oral presentation.
4. S.V. Porokhin, A.M. Abakumov, «Optimization of spray pyrolysis synthesis and measurements of catalytic properties for Ca-doped $\text{LaFe}_x\text{Ni}_y\text{O}_3$ perovskites» // 4th international conference of young scientists “Topical problems of modern electrochemistry and electrochemical materials science” 15-18 September 2019, Moscow Region, Russia. Poster presentation.
5. S.V. Porokhin, A.M. Abakumov, «Synthesis, morphology and catalysts properties of $\text{LaFe}_x\text{Ni}_y\text{O}_3$ doped Ca» // International Scientific Conference of Students, PhD students and Young Scientists "Lomonosov-2019" April 8-12 2019, Moscow, Russia. Poster presentation.
6. S.V. Porokhin, Y.E. Shakhova, A.M., Abakumov. «Morphology and catalysts properties of Ca-doped $\text{LaFe}_{0.25}\text{Ni}_{0.75}\text{O}_3$ » // 14th Conference with the international participation of the international "Physico-chemical problems of renewable energy" 13-16 September 2018 Chernogolovka, Russia, book of abstract, P.87. Oral presentation.
7. Порохин С.В. «Получение и исследование морфологии $\text{LaFe}_{0.25}\text{Ni}_{0.75}\text{O}_3$ » // V Всероссийский конкурс научных докладов студентов «Функциональные материалы: разработка, исследование, применение» 23 мая 2018, Тамбов, Россия. Poster presentation.

Acknowledgments

I express my deep gratitude and sincere appreciation to my supervisors Prof. Artem M. Abakumov and Prof. Victoria A. Nikitina for their support and help with the analysis of the obtained data. I also thank Prof. Elena R. Savinova for collaboration, support, and valuable comments about experiments performed at Strasbourg University.

I thank Dr. Maria Kirsanova and Mr. Kirill Dosaev for their help with the experimental arrangement for synthesis and the electrochemical measurements. Also, I would like to thank our lab engineer Artem Zaikin.

I would like to acknowledge my colleagues who carried out some of the experiments presented in the Thesis. SEM images were obtained by Dr. Yaroslava Shakhova, TEM images were acquired by Prof. Artem Abakumov, X-ray photoelectron spectroscopy measurements were performed by Dr. Egor Pazhetnov, DFT calculations were performed by Prof. Dmitry Aksyonov. Mössbauer spectroscopy data were registered by Dr. Dmitry Filimonov, and Inductively Coupled Plasma Spectroscopy data were obtained by Dr. Ivan Mikheev (Lomonosov Moscow State University).

Finally, I thank my family, wife and friends for their support during my PhD and good company.

The PhD candidate contribution

All samples were synthesized by the author and characterized by X-ray powder diffraction and electrochemical measurements, surface area analysis and iodometric titration were also performed by the author. Preparation of samples for further analysis using electron microscopy, X-ray photoelectron spectroscopy, Mössbauer spectroscopy and Inductively Coupled Plasma Spectroscopy was performed by the author. The TEM images for cycled samples were taken with the participation of the author. Data management and analysis was carried out with the help of supervisors. Contributions of co-authors were listed in the acknowledgements section.

Table of Contents

Abstract	3
Publications.....	5
List of Conferences.....	6
Acknowledgments.....	7
The PhD candidate contribution	8
List of Symbols, Abbreviations	12
1. Introduction	14
2. Literature review and formulation of the problem	15
2.1 Water electrolysis: background and motivation	15
2.2 Electrochemical water splitting.....	18
2.3 Electrolyzers for water splitting.....	19
2.4 Oxide materials as OER catalysts	22
2.4.1 Perovskite synthesis.....	26
2.5 Kinetics and mechanisms of oxygen evolution reaction on oxide surfaces.....	32
2.6 Descriptors of activity in OER.....	34
2.7 Lattice oxygen mediated mechanism.....	39
2.8 (Oxy)hydroxides as active OER surface in alkaline media	48
2.9 Electron microscopy study of electrocatalytic surfaces after the OER.....	52
2.10 Conclusions from the literature review.....	57
3. Methodology	59
3.1 Synthesis of perovskite catalysts (basic method).....	59
3.1.1 Synthesis of perovskite catalysts (modified method)	59

3.1.2 Perovskite surface treatment	60
3.2 Powder X-ray diffraction	60
3.3 Electron microscopy	61
3.4 Surface area analysis.....	61
3.5 ⁵⁷ Fe Mössbauer spectroscopy.....	62
3.6 X-ray photoelectron spectroscopy	62
3.7 Oxygen content analysis	63
3.8 Catalyst ink deposition.....	63
3.9 Electrochemical measurements.....	64
3.9.1 Reference electrode calibration.....	66
3.9.2 Rotating ring disk electrode calibration.....	66
3.10 Inductively coupled plasma mass spectroscopy/atomic emission spectroscopy ..	67
3.11 DFT details.....	68
4. Results and discussion	70
4.1 Optimization of spray pyrolysis synthesis	70
4.2 Synthesis of La _{1-x} Ca _x Fe _{0.7} Ni _{0.3} O _{3-δ} (x = 0, 0.3, 0.5) samples	73
4.2.1 Characterization of La _{0.6} Ca _{0.4} Fe _{0.7} Ni _{0.3} O _{2.9}	83
4.3 Electrochemical performance in the OER	87
4.3.1 Effects of catalyst loading and oxide/carbon ratio.....	91
4.4 Catalyst stability.....	94
4.4.1 Catalyst stability under potentiostatic and galvanostatic measurement conditions	101
4.5 DFT+U calculations.....	107

4.6 Catalyst activity and stability in the electrolyte with trace amounts of Fe	111
5. Conclusions.....	120
Appendix.....	121
Bibliography	125

List of Symbols, Abbreviations

Term – definition

ABF-STEM– annular bright field scanning transmission electron microscopy;

AEM – adsorbate evolution mechanism;

AEMWE – anion exchange membrane water electrolysis;

BET– Brunauer–Emmett–Teller;

BJH – Barrett-Joyner-Halenda;

CVs – cyclic voltammograms;

DFT – density functional theory;

ECSA – electrochemical surface area;

ED – electron diffraction;

GC – glassy carbon;

GDL – gas diffusion layer;

GGA – generalized gradient approximation;

HAADF-STEM – high angle annular dark field scanning transmission electron microscopy;

HR-TEM – high-resolution TEM;

ICP-AES – inductively coupled plasma atomic emission spectroscopy;

ICP-MS – inductively coupled plasma mass spectroscopy;

LCFN3 – $\text{La}_{0.7}\text{Ca}_{0.3}\text{Fe}_{0.7}\text{Ni}_{0.3}\text{O}_{3-\delta}$ (nominal composition);

LCFN5 – $\text{La}_{0.5}\text{Ca}_{0.5}\text{Fe}_{0.7}\text{Ni}_{0.3}\text{O}_{3-\delta}$ (nominal composition);

LCFN5_m – $\text{La}_{0.6}\text{Ca}_{0.4}\text{Fe}_{0.7}\text{Ni}_{0.3}\text{O}_{2.9}$;

LCFN5_m S – LCFN5_m soaked in 1M NaOH;

LFN – $\text{LaFe}_{0.7}\text{Ni}_{0.3}\text{O}_3$ (nominal composition);

LOER – lattice oxygen evolution reaction;

LOM – lattice oxygen-mediated mechanism;

MEA – membrane-electrode assembly;

OER – oxygen evolution reaction;

ORR – oxygen reduction reaction;

PDOS – projected density of states;

PEMWE – proton exchange membrane water electrolysis;

PXRD – powder X-ray diffraction;

RDE – rotating disk electrode;

RHE – reversible hydrogen electrode;

RRDE – rotating ring-disk electrode;

STEM-EDX – scanning transmission electron microscopy energy-dispersive X-ray;

TEM – transmission electron microscopy;

TOF_{tm} – turnover frequency (transition metals);

USP – ultrasonic spray pyrolysis;

VC – Vulcan carbon XC72R;

WE – water electrolysis;

XPS – X-ray photoelectron spectroscopy;

1. Introduction

Deployment of alternative renewable energy sources will reduce the anthropogenic impact on the environment and dependence on fossil fuel. The use of hydrogen as an energy carrier is a very promising direction of alternative energetics. The production of hydrogen with minimum carbon footprint is possible by water electrolysis (WE), using energy from solar panels, wind turbines and nuclear power plants. As a typical electrochemical device, an electrolysis cell consists of three major parts: anode, cathode and electrolyte. On the anode side, energy efficiency losses are associated with the sluggish kinetics of the Oxygen Evolution Reaction (OER), which is kinetically more hindered compared to Hydrogen Evolution Reaction (HER) at the cathode. Currently, transition metal oxides/(oxy)hydroxides and noble metals are extensively investigated and used as prototype catalysts for OER. But noble metals are expensive and poorly suitable for widespread commercial use, while transition metal-based electrocatalysts are significantly cheaper, yet their intrinsic activity and stability under the electrocatalytic conditions are still insufficient and require further enhancement as well as the fundamental understanding of the electrocatalytic mechanisms [1],[2]. In addition, bare (oxy)hydroxides have poor electrical conductivity, which limits their high efficiency with a thick electrocatalyst layer due to ohmic losses and, accordingly, it is problematic to create a high-performance electrolyzer capable of operating at high currents [3],[4] and therefore (oxy)hydroxides are used in the form of thin films in combination with a conductive substrate [5],[6],[7]. The perovskite structured transition metal oxides are among the best model materials for electrocatalytic research and further commercial

applications, as they are low-cost materials with a promising high catalytic activity, in addition, their electrical conductivity is higher, which will potentially allow the creation of high-performance electrolyzers [8],[9],[10]. NiFe-based perovskites are of particular interest for alkaline water splitting, because NiFe-based compounds have historically been recognized as good anode reaction electrocatalysts in industrial alkaline electrolyzers [11],[12],[13]. However, the mechanism of OER on NiFe-based perovskites is still far from being well-understood, which imposes restrictions on the design of durable and efficient electrocatalysts. Thus, in this work we focused on obtaining Ni-Fe-based perovskites, increasing their electrocatalytic properties and studying the active centers on the surface of an electrocatalyst in controlled electrochemical experiments. The correct determination of active centers and detailed characterization of the active surface under the relevant experimental conditions are important for understanding the OER reaction mechanism and predicting electrocatalytic properties, which will further help in the development of efficient, low-cost and stable electrocatalysts for WE.

2. Literature review and formulation of the problem

2.1 Water electrolysis: background and motivation

Issues related to sustainable energy sources have arisen in recent decades due to the increase in greenhouse gas emissions and the persistent ecological footprint of the fossil fuels such as coal and oil as the main source of energy. The tremendous economic growth based on fossil fuels in the last decades, accompanied by increased energy

consumption led to environmental problems, which involve all aspects, from personal to global. For instance, quality of air in big cities is a lot worse than in suburban areas, and this is ultimately impacting people's health and quality of life [14]. In the global aspect, climate change due to the anthropogenic factor from human actions is decisive for the growth of the average temperature on the planet [15]. One of the possible adequate strategies in the current situation is increasing the energy efficiency of technologies based on renewable resources.

The strategy to reduce harmful emissions and improve living standards through the introduction of energy-efficient technologies using renewable energy sources is becoming a determining factor in the plans of leading countries (the Paris agreement). So, dated August 5, 2021, the Government of Russian Federation (GRF) approved the «Concept for the development of hydrogen energy in the Russian Federation» which includes long-term initiatives until 2035. These initiatives include considerations related to the production of hydrogen fuel from water electrolysis (WE). In the forced scenario of the development of this strategy, the target price for 1 kg of H₂ is expected to be less than 2 US dollars by 2050, which would make the cost of hydrogen produced with renewable energy competitive with the cost of hydrogen produced from fossil fuels. Today, WE technologies cannot compete with steam reforming (0.5-1.7 US\$/kg H₂), due to higher production costs (4-8 US\$/kg H₂) [16],[17], however, increasing energy efficiency of WE coupled with drop in the renewable electricity cost are expected to change this trend.

A global strategy to tackle the climate crisis through concrete action and innovation (including developing efficient WE) was recently presented at Hydrogen Shot

Summit on June 7, 2021, governed by the U.S. Department of Energy (DOE). DOE reclaims to reduce the cost of clean hydrogen by 80% - achieving 1 US\$/kg [18]. The European Fuel Cells and Hydrogen Joint Undertaking (FCH JU) shares a similar position in reduction of cost of hydrogen from WE [19]. Potentially, the implementation of the global "hydrogen strategy" will lead to the fact that in 2050 hydrogen will meet 18% of the total global energy demand [18]. And here, for decarbonization, it is important that the fraction of hydrogen production by WE occupies a significant part.

WE produces sustainable energy resources such as hydrogen and oxygen. Hydrogen is perfect for energy conversion and storage technologies, while oxygen is a useful co-product that can be used in the medical sector and chemical production/metallurgy as a strong oxidizer. Alkaline or acidic WE typically produces high purity gases (H_2 and O_2), which in some cases can be used without further purification. Currently, the promising application of hydrogen is the adoption of fuel cell technology in the transport sector: for electric vehicles, trucks, trains, ships, and even airplanes. Additionally, hydrogen is now widely used in methanol, ammonia, and steel production. All these markets can easily adsorb billions of tons of hydrogen. Currently, about 5% of hydrogen is produced by using alternative processes including electrolysis, while most of the world's hydrogen supply currently comes from the reformation of fossil fuels: steam methane reforming, oil reforming and coal gasification, where CO_2 is a co-product [17],[20], which aggravates existing ecological risks.

2.2 Electrochemical water splitting

The WE process in alkaline solution comprises two half-reactions: the HER $2\text{H}_2\text{O} + 2\text{e}^- \rightarrow \text{H}_{2(\text{g})} + 2\text{OH}^-$ at the cathode and the OER $4\text{OH}^- \rightarrow 2\text{H}_2\text{O} + \text{O}_{2(\text{g})} + 4\text{e}^-$ at the anode. WE was discovered in 1789 by Adriaan van Troostwijk and Johan Deiman, and in 1888 Pavel Lachinov proposed an industrial method for the production of hydrogen and oxygen by the electrolytic method [21]. The OER is a critical step (rate-determining reaction) in the water splitting process due to the sluggish kinetics compared to that of HER at the same operation conditions [22],[23]. OER is a four-electron transfer reaction with three reaction intermediates (adsorbed OH^* , O^* , and OOH^*), while the HER requires only two electrons with a single reaction intermediate (adsorbed hydrogen atom H^*). Efficient OER electrocatalysts are needed to increase the overall WE energy conversion efficiency, reduce the energy losses and lower the associated costs.

The thermodynamic voltage for water splitting is 1.23 V (ΔE_{therm}) at standard conditions (25 °C and 1 bar). However, commercial electrolyzers typically operate at much higher voltages. The typical operational cell voltage for anion and polymer exchange membrane electrolysis are ~1.85 V and ~1.75 V for 400 mA cm⁻² current density at 50–60 °C, respectively [24],[25],[26]. The cell voltage (ΔE) includes anodic (η_{anodic}) and cathodic (η_{cathodic}) overpotentials, and the ohmic resistance of the electrolysis cell (IR): $\Delta E = \Delta E_{\text{therm}} + \eta_{\text{anodic}} + \eta_{\text{cathodic}} + IR$. Thus, (ΔE) is typically far from the thermodynamic value (1.23 V). This motivates researchers to search for new approaches in the structural/chemical design of electrocatalysts to reduce total overpotential and approach the thermodynamic limit for WE.

2.3 Electrolyzers for water splitting

Electrolyzers for water splitting operate either in alkaline or in acidic media. The alkaline water electrolyzers (AWE) are characterized by low cost of the electrode materials, long-term stability and robust performance, as this technology has been proposed more than 100 years ago. Electrode materials for AWE are typically in a form of alloy-plated steel materials based on abundant low-cost transition metals such as Fe, Ni, Co [27],[28],[29]. The immersed electrodes usually operate in concentrated 20-40 wt.% KOH liquid electrolyte being separated by a thick (up to 2 mm) diaphragm (Figure 1a). Porous materials like ZIRFO PERL UTP 500 (mesh polyphenylene sulfide fabric, which is symmetrically coated with a mixture of a polymer and zirconium oxide), nickel oxide or asbestos are used for diaphragms [30],[13],[31]. AWEs typically function in highly corrosive environments and deliver limited current densities due to high internal cell resistance and detrimental to energy conversion efficiency crossover of H₂ and O₂, which is insufficiently suppressed by the diaphragm [32].

Recently, a zero-gap electrolysis cell design was employed. A zero-gap electrolysis cell consists of a membrane-electrode assembly (MEA) and includes anode and cathode layers of catalysts with an ionomer (binder), which are deposited on a gas diffusion layer (GDL). GDL is typically Ti, Ni, or stainless steel in a form of foam/mesh on carbon paper [33]. The non-porous ion-exchange membrane, which is selectively permeable to hydrated protons or hydroxide ions, is placed between the GDL and pressed to form MEA. This device architecture decreases the distance between the two electrodes to the membrane thickness and hence reduces ohmic losses (IR) of the cell [34] and

improves the separation of O₂ and H₂, thus providing compact design with higher energy efficiency.

The AWE with anion exchange membranes in zero-gap cell design are called Anion Exchange Membrane Water Electrolyzers (AEMWE) [25] (Figure 1c). Such electrolyzers can operate in low-concentrated alkaline solutions or even with distilled water as feed, which can be supplied to the anode or to both electrodes [13],[26]. It is similar to Proton Exchange Membrane Water Electrolyzers (PEMWE, Figure 1b), but replaces the acidic membrane with a basic one and enables the use of non-platinum group metal catalysts and cheaper MEA materials in contrast to PEMWEs, which use Ir, Pt and mainly Ti for GDL [35]. Figure 1 shows different types of WE cells.

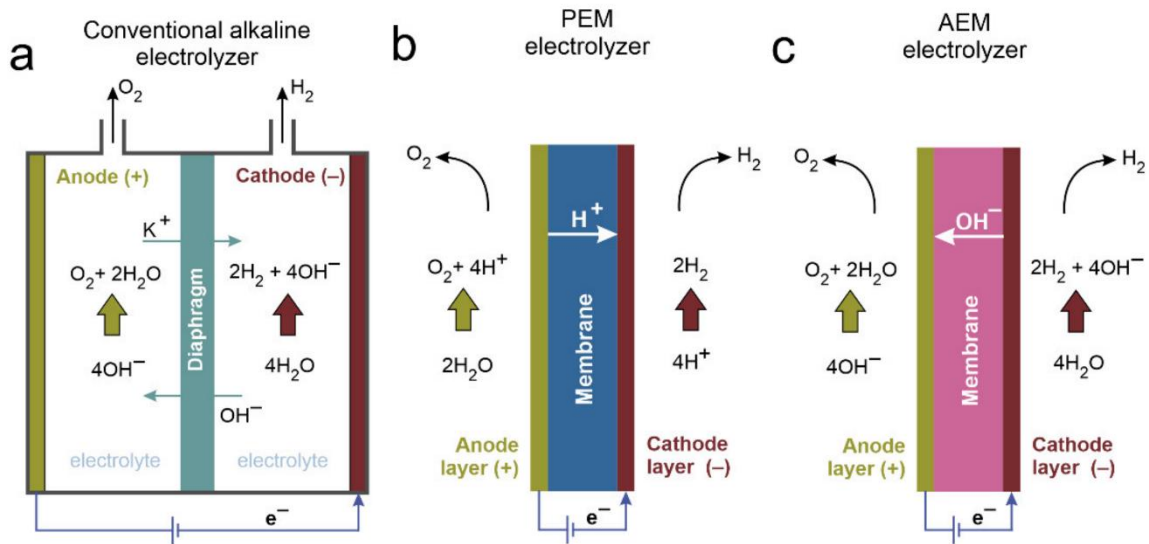


Figure 1. Water electrolysis cells: (a) conventional AWE (b) Proton Exchange Membrane Water Electrolyzer (PEMWE). (c) Anion Exchange Membrane Water Electrolyzer (AEMWE). Reprinted from ref. [29]. Copyright 2021 by the authors. Licensee MDPI, Basel, Switzerland.

However, PEMWE, which use a proton exchange membrane, exhibit higher current densities ($> 2 \text{ A cm}^{-2}$) and higher efficiency due to the lower ohmic loss of the cell compared to that of AEMWE [36],[37].

To increase the WE efficiency, an increased pressure in the electrolyzer is usually used, for example, AWE, PEMWE and AEMWE may operate at pressures up to 30, 76 and 30 bar respectively. Operating temperature is also increased ranging from 45 to 90 °C [26],[38].

Table 1 presents AEMWE, its components, and its characteristics. Clearly, the electrolyzers based on noble metal oxides and Ni-Fe mixed oxides demonstrate the best performance.

Table 1 AEMWE components and cell working parameters, adapted from ref. [26].

Anode	Membrane	Cathode	Ionomer/ binder	Water feed	Cell: Voltage, V/ Current density, A cm^{-2} / T, °C
IrO_2	A-201 Tokuyama	Pt black	AS-4	Deionized water	1.8/ 0.399/ 50
NiFe_2O_4	Sustainion 37–50	NiFeCo	Nafion	1 M KOH	1.9/ 1/ 60
$\text{Ni}_{0.75}\text{Fe}_{2.25}\text{O}_4$	Sustainion 37–50	Pt/C	—	1 M KOH	1.8/ 1.3/ 45 ref. [39]
Ni–Fe	(xQAPS)	Ni–Mo	(xQAPS)	Ultrapure water	1.85/ 0.4/ 70
Ni	A-201 Tokuyama	Ni	—	1 M KOH	1.9/ 0.15/ 50
IrO_2	FAA-3-50	Pt/C	FAA-3-Br	1 M KOH	1.9/ 1.5/ 70
NiCo_2O_4 on steel mesh	Homemade not specified	Powder Acta 4030	Homemade, not specified	DI-water	1.86/ 0.4/ 60
CuCoO_x on Ni foam	A-901 Tokuyama	Ni/(CeO_2 – La_2O_3)/C on carbon paper	I2	1% K_2CO_3	2.1/ 0.5/ 50
$\text{Li}_{0.21}\text{Co}_{2.79}\text{O}_4$	From Cranfield University	Nickel nanopowders	QPDTB- OH^-	1M KOH	2.05/ 0.3/ 45 ref. [40]

Commercial manufacturers usually do not disclose the compositions of the electrode materials which they use in the production of AEMWE. In addition, the number of manufacturers is currently small, and this does not allow full assessment of the market for electrocatalytic materials.

One of the currently commercially available AEMWE developed by Enapter uses CuCoO_x (Acta 3030) as the anode and $\text{Ni/CeO}_2\text{-La}_2\text{O}_3/\text{C}$ (Acta 4030) as the cathode. It operates at 0.47 A cm^{-2} current density at an average cell voltage of 2.0 V (voltage loss 0.1 mV h^{-1}) with a 1% $\text{K}_2\text{CO}_3/\text{KHCO}_3$ electrolyte at 50°C [41],[42]. Another AEMWE manufacturer, Proton Onsite, with a LiCoO_2 anode and a Pt/C cathode demonstrates 0.4 A cm^{-2} at an average voltage of 2.0 V for 1000 hours using 1% KHCO_3 electrolyte [43]. Thus, the most promising compounds based on Ni-Fe mixed oxides are not yet available in commercial electrolyzers with an anion exchange membrane, which is probably related to difficulties in achieving attractive durability and performance [44] due to a rather complex pattern of degradation of catalytic materials during WE and the OER mechanism itself.

2.4 Oxide materials as OER catalysts

In general, noble metal oxides such as IrO_2 and RuO_2 , as well as compounds based on them, are considered as the most active OER catalysts both under acidic and alkaline WE, but they are scarce (0.1 ppb for Ru and 0.05 ppb for Ir in the Earth crust) and expensive (19000 US\$/kg for Ru and 133000 US\$/kg for Ir; access 14.12.2021)

[45],[46], which impedes wide dissemination of the WE technology. The cost of transition metals is incomparably lower (e.g. metallic nickel costs ca. 24 US\$/kg). Moreover, stability issues related to Ru dissolution is an additional limiting factor in wide application of precious metal-based WE electrocatalysts [47]. Clearly, cheaper, stable and more efficient catalysts materials are highly desirable.

Among other materials, oxides with perovskite structure with the general formula of $(A,A')(B,B')O_{3-\delta}$ (A, A' – rare-earth or alkali-earth cations, B, B' – transition metal cations), have shown promising catalytic activity in alkaline media [48], [49],[9],[10],[50]. Additionally, their catalytic properties can be tuned by varying chemical composition through substitutions. The perovskite materials bearing 3d transition metals have been extensively studied during the last decades as potential OER catalysts in alkaline media (Figure 2). For lanthanum-based perovskite compositions, the following sequence of OER activity was established $V \approx Cr < Mn < Fe < Co \approx Cu < Ni$, with the nickel-based composition being the most active [51]. However, the A-site metal can also adjust the catalytic properties. For instance, when Y is at the A-site, $YCoO_3$ perovskite has better performance compared to $YNiO_3$, but still inferior in activity to $LaNiO_3$. The $(Ca/Sr)CoO_3$ and $(Ca/Sr)FeO_3$ compounds could provide higher OER activity compared to $LaCoO_3$ or $LaFeO_3$, whereas the activity of $CaFeO_3$ and $SrCoO_3$ will be higher than that of $LaNiO_3$ [51],[52] (Figure 2a).

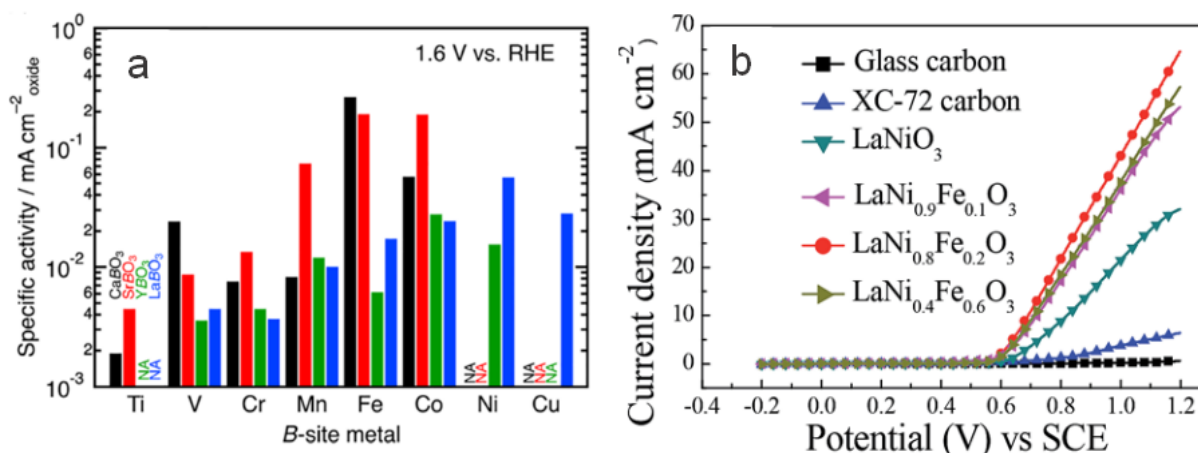


Figure 2. (a) Specific activities for perovskite oxides at 1.6 V vs RHE in 0.1M KOH. Reprinted from ref. [51]. Copyright 2018, American Chemical Society. (b) Polarization curves of $\text{LaNi}_{1-x}\text{Fe}_x\text{O}_3$ ($x = 0, 0.1, 0.2, 0.6$). Reprinted from ref. [53] Copyright 2015, The Royal Society of Chemistry.

Changing the Ni:Fe ratio on B-site also changes the catalytic properties (Figure 2b). Zhang *et al.* [53] established an optimal Ni:Fe ratio of 8:2 for La-based perovskites, Figure 2b, which was later confirmed by Wang *et al.* [54]. It has been demonstrated for Ni, Fe, and Co-based systems that bimetallic mixed compounds exhibit enhanced OER activity compared to monometallic oxides [12]. Under certain conditions, Ni-Fe systems even outperform the compounds based on noble elements, such as Ir and Ru in terms of mass and specific activity [55],[56],[57],[58]. This synergistic effect for Ni and Fe was observed in oxides, hydroxides, and perovskites with different Ni:Fe content [59],[60],[61],[62],[63],[64],[65]. Guo *et al.* [66] demonstrated enhanced catalytic activity of the $\text{LaNi}_{0.5}\text{Fe}_{0.5}\text{O}_3$ perovskite compared to LaNiO_3 and LaFeO_3 , which was further improved by heterovalent Sr doping at the A- site. Wang *et al.* [67] investigated the $\text{La}_{0.5}\text{Sr}_{0.5}\text{Ni}_x\text{Fe}_{1-x}\text{O}_{3-\delta}$ ($x = 0.8, 0.5, 0.4, 0.2$) system and observed that the nominal $\text{Ni}_{0.4}\text{Fe}_{0.6}$ ratio has the highest OER activity. Li *et al.* [68] studied a similar system with a

fixed Ni:Fe stoichiometry: $\text{La}_{1-x}\text{Sr}_x\text{Ni}_{0.8}\text{Fe}_{0.2}\text{O}_{3-\delta}$ ($x=0, 0.1, 0.3, 0.5$), and reported on significant activity improvement with Sr doping (the lowest OER overpotential was demonstrated by the sample with a maximal Sr content). However, Sr-doping leads to the formation of secondary phases, which raises questions on the homogeneity of the obtained perovskites.

Table 2 collects OER activities of some relevant complex mixed oxides, with experimental parameters such as mass loading, oxide to carbon ratio in the electrode used for the electrochemical measurements, electrolyte composition and temperature. It should be noted that each of these parameters can significantly affect the assessment of the activity value. Various metrics are used in the literature to determine activity: overpotential at a specific current density or current density at a given overpotential. The normalization of these values to the mass loading of the active component and to the specific surface area makes it possible to better understand the nature of the catalytic activity of the compounds and evaluate it [69]. It is worth noting, that direct comparison of activity across various studies is limited and should be taken with care, due to different experimental conditions and measurement protocols. However, such a comparison still allows us to assess the potential of the double A/B-site substitution approach in perovskites as a property tuning method to further enhance the catalyst activity in OER. As follows from inspecting data from Table 2, mixed perovskites with double substitution, such as $\text{La}_{0.4}\text{Sr}_{0.6}\text{Ni}_{0.5}\text{Fe}_{0.5}\text{O}_{3-\delta}$, show the highest activity in OER.

Table 2. Comparison of the specific and mass OER activities at 1.61 V.

Catalyst	Total mass loading ($\mu\text{g cm}^{-2}$)	oxide: carbon weight ratio	Electrolyte	T ($^{\circ}\text{C}$)	iR-corr.	S_{BET} (m^2g^{-1})	Specific activity ($\text{mA cm}^{-2}_{\text{oxide}}$)	Mass activity ($\text{A g}^{-1}_{\text{oxide}}$)	Tafel slope b (mV dec^{-1})	Ref.
$\text{La}_{0.5}\text{Sr}_{0.5}\text{Mn}_{0.5}\text{Co}_{0.5}\text{O}_3$	30	Sibunit-152 (1:1)	1 M NaOH	25	+	10.2	0.13	~13	53	[70]
LaNiO_3	51	nitrogen-doped mesoporous carbon NC (3:7)	0.1 M KOH	r.t.	+	11	1.6	180	42	[71]
LaNiO_3 - 600	408	no carbon	0.1M KOH	r.t.	+	25.2	0.02	~4	84	[72]
$\text{LaFe}_{0.5}\text{Ni}_{0.5}\text{O}_3$ nanorods	408	carbon powder	1 M KOH	r.t.	+	31.7	0.15	47	64	[54]
IrO_2	51	VC (1:4)	0.1 M KOH	r.t.	+	14.5	~1.1	~165	88	[73]
Ni-Fe LDH* (Ni:Fe 45:55)	51	no	0.1 M KOH,	r.t.	?	27	~2.2	~600	37	[61]
Ni-Fe LDH -Bulk	70	No	1M KOH	r.t.	?	NA	NA	~360	67	[74]
LaNiO_3/Ni (foam)	23000	no	1M KOH	r.t.	+	NA	NA	~1	NA	[75]
$\text{La}_{0.5}\text{Sr}_{0.5}\text{Ni}_{0.4}\text{Fe}_{0.6}\text{O}_{3-\delta}$	400	no	1 M KOH,	r.t.	+	14.9	0.44	66	NA	[67]
$\text{La}_{0.5}\text{Sr}_{0.5}\text{Ni}_{0.8}\text{Fe}_{0.2}\text{O}_3$	464	Super P (1:1)	0.1M KOH	r.t.	+	~5.8	1.2	~68	NA	[68]
$\text{La}_{0.4}\text{Sr}_{0.6}\text{Ni}_{0.5}\text{Fe}_{0.5}\text{O}_{3-\delta}$	250	nitric acid-treated carbon black (XC-72) (1:2)	1M KOH	r.t.	+	9.8	~3.8*	~375*	52.8	[66]
$\text{La}_{0.6}\text{Sr}_{0.4}\text{Co}_{0.2}\text{Fe}_{0.8}\text{O}_{3-\delta}$	50	Acetylene Black (5:1)	0.1M KOH	r.t.	+	19	0.1	~17	75	[76]

*LDH - layered double hydroxides

2.4.1 Perovskite synthesis

As this thesis is devoted to the electrocatalytic properties of perovskite-type mixed oxides, in this part of the literature review we discuss methods and synthesis conditions (T_{drying} – the temperature of gel drying and T_{ann} – the temperature of powder

annealing) for Ni- and/or Fe-based perovskites with La³⁺ substitution for Ca²⁺ or Sr²⁺.

The literature data for the relevant materials are collected in Table 3.

Table 3. Synthesis conditions of Ni-Fe based perovskites, phase purity and surface area.

Sample	Method of synthesis and parameters	Phase purity	BET surface area, m ² g ⁻¹	Ref.
La _{0.6} Ca _{0.4} Fe _{1-x} Ni _x O ₃ (0.0 ≤ x ≤ 1.0)	Sol-Gel (SG), T _{drying} = 250 °C, T _{ann} =700 °C in air for 10 h	x > 0.7: A ₂ BO ₄ -type impurities; x=0.5: NiO impurity; x≤0.3: phase pure	22 - 29	[77]
La _{0.5} Ca _{0.5} Fe _{0.7} Al _{0.3} O ₃	Solid-state: carbohydrate-mechanochemical method. Oxides milled for 24 h with ethylene glycol, T _{drying} =300 °C, then T _{ann} =1000 °C / 24 h.	Al ₂ O ₃ impurity	4	[78]
LaNi _{0.5} Fe _{0.5} O ₃ x=0.25, 0.5	SG, T _{drying} = 150 °C, T _{ann} =700 °C / 5h	Phase pure	7.10	[79]
LaNi _{0.6} Fe _{0.4} O ₃	Combustion spray pyrolysis at unknown T, then T _{ann} =800 °C	Phase pure	8.0	[80]
La _{1-x} Sr _x Ni _{0.8} Fe _{0.2} O ₃ (x = 0, 0.1, 0.3, 0.5)	SG, T _{drying} = 260 °C , T _{ann} =900 °C / 5 h	x=0.5, 0.3: NiO and LaSrNiO ₄ impurities	2.5 - 5	[81]
La _{0.5} Sr _{0.5} Ni _x Fe _{1-x} O ₃ (x=0.8, 0.5, 0.4,0.2)	SG, T _{ann} =850 °C / 3 h	NiO and LaSrNiO ₄ impurities	14.2 - 15.7	[67]
La _{0.6} Ca _{0.4} Fe _{0.8} Ni _{0.2} O ₃	SG, T _{ann} =1000°C 1 h then treatment in 10% H ₂ -Ar at 700 °C / 10 h	Ni impurities	N/A	[82]
La _{0.4} Ca _{0.6} Fe _{0.8} Co _{0.2} O ₃	Citrate pyrolysis method. T _{drying} =200 °C, then T _{ann} = 900 °C / 5 h	Phase pure	2.6	[83]
La _{0.5} Ca _{0.5} FeO ₃ La _{0.75} Ca _{0.25} FeO ₃	Nitrate combustion method T _{ann} = 800 °C under dry air	N/A	1.1- 1.8	[84]
La _{1-x} Ca _x FeO ₃ (x = 0.0, 0.1, 0.2, 0.3, 0.4)	SG. T _{drying} =70 then 250°C, T _{ann} =700 °C / 6 h.	Phase pure for SG	19 - 38	[85]
	Co-precipitation of the nitrates, aging at pH 10, 48 h. T _{drying} =110 °C. T _{ann} = 700 °C / 6 h	Traces of CaCO ₃ for Co-precipitation x=0.2 and higher	8 - 21	
La _{0.5} Ca _{0.5} Fe _{0.7} Ni _{0.3} O ₃	SG (citrate acid and polyethylene glycol), T _{drying} = 80 °C then 120 °C / 24 h. T _{ann} =750 °C / 5 h	trace amounts of CaCO ₃	N/A	[86]
La _{0.6} Ca _{0.4} Fe _{1-x} Ni _x O ₃ (x = 0.1, 0.2, 0.3)	SG: nitrate salts and citric acid were dissolved in distilled water + ethylene glycol. T _{drying} =70 °C. T _{ann} =600 °C / 12 h	Phase pure	N/A	[87]
La _{1-x} Ca _x Fe _{0.8} Ni _{0.2} O ₃ (0 ≤ x ≤ 0.9)	SG. Same as above	x≥0.5: Ca ₂ Fe ₂ O ₅ impurity; x≤0.7: La ₂ O ₃ and CaO impurities	NA	[88]

It is worth noting, that some of the described materials were used as catalysts in different electrocatalytic oxidation processes (for oxidation of methanol, ethanol, dimethyl ether, see ref. in Table 3), which highlights wide possibilities of using Fe-Ni perovskites as catalysts.

Perovskite synthesis is possible via many synthetic methods including solid-state, sol-gel (SG), co-precipitation and spray pyrolysis (SP). Soft chemistry methods make it possible to obtain catalysts powders with a relatively large surface area. For the synthesis, precursors of the corresponding metal salts/oxides are used, the temperature and annealing time are in the range from 600 to 1000 °C, and from 3 to 24 hours, respectively. The BET surface area for the resulting perovskite materials varies from 1.1 to 38.6 m²g⁻¹, depending on the synthetic route.

Among the others we can highlight the SP method, which has several advantages for the synthesis of the electrocatalysts. This method makes it possible to obtain spherical porous/hollow particles in a controlled manner [89],[90], which exposes more active surface, compared to rod and cubic morphologies, which results in a higher catalytic activity [91]. Moreover, the SP method allows obtaining catalyst powders in a continuous production process, with facile control of the composition due to the good mixing of the precursors at the molecular level in the spray solution, which is important for obtaining complex double-substituted perovskite oxides.

Different nebulizers can be used to generate the spray (e.g. ultrasonic, pneumatic and electrostatic atomizers). The pyrolysis process could occur in a furnace, heating

plate, or in flame. In this work, we chose the ultrasonic method for SP, due to optimal droplet size with uniform size distribution and spraying rate.

The ultrasonic SP (USP) method offers a synthesis approach to produce nanostructured materials with a unique morphology. The formation of liquid droplets consists of two processes which occur simultaneously: the first one is generation of capillary waves at the liquid-gas interface, which breaks at the crest of the wave at a certain amplitude (which is provided by the ultrasonic generator) and form liquid drops. Another process is cavitation, i.e. the formation of bubbles in a liquid that can grow to tens of μm , and then implosively collapse [92],[93]. After the collapse (periodic hydraulic shocks) the stored energy is released in a very short time, which ruptures the liquid-gas interface and the liquid micron-sized droplets are formed on the surface of a liquid (Figure 3).

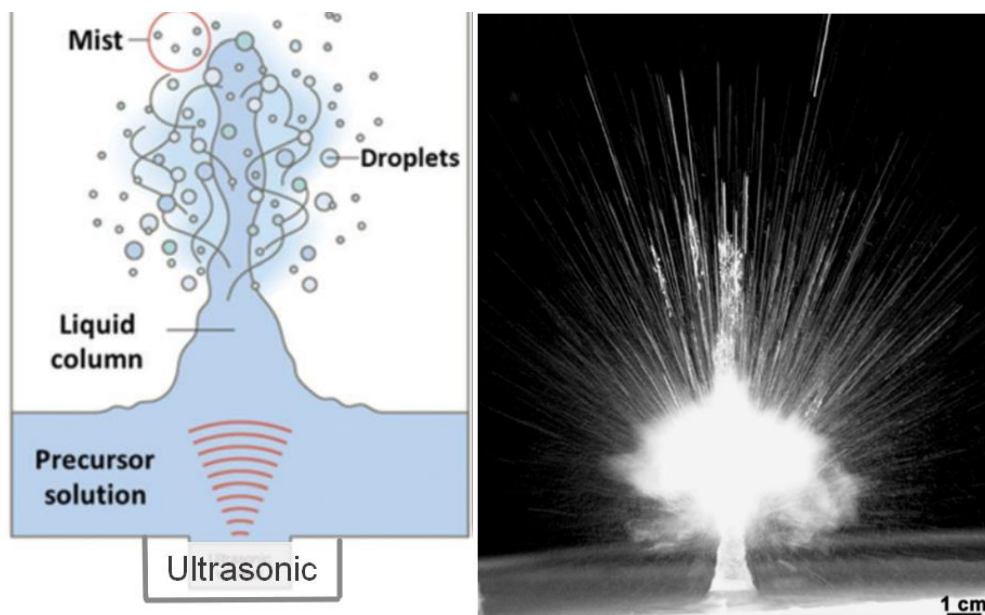


Figure 3. Scheme of spraying with the formation of a capillary wave is presented without cavitation bubbles in the solution for simplicity. However, cavitation bubbles periodically explode and cause hydraulic shocks that break the liquid-gas interface, causing additional spraying (left) reprinted from ref.[94]. Copyright 2019, The Royal Society of Chemistry, and photograph (right) of an ultrasonic fountain and mist produced at 1.7 MHz. Reprinted from ref. [95]. Copyright 2005, American Chemical Society.

Typically, a piezoelectric generator is used to atomize a liquid, which creates oscillations of a certain frequency. The resulting mist is then carried by the gas flow to the hot zone of the furnace, where the aerosols are thermally decomposed and eventually a solid phase is formed. The simple model process involves the following steps: droplet generation, evaporation of solvents, diffusion of solutes, precipitation, decomposition, and densification [96].

The size of droplet which detached from liquid surface can be described by the Lang equation, which establishes the relationship between the ultrasonic frequency and the diameter of droplets [97]:

$$D = 0.34 \left(\frac{8\gamma\pi}{\rho v^2} \right)^{1/3}, \quad (1)$$

where D is the diameter of the droplet (m), γ is the surface tension (N m^{-1}), ρ is the solution density (kg m^{-3}), v is the ultrasonic frequency (MHz).

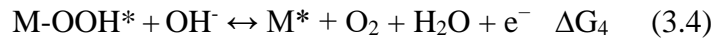
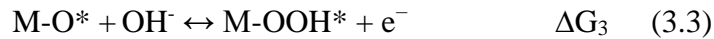
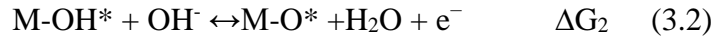
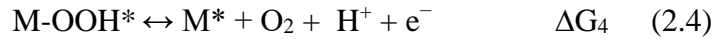
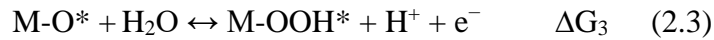
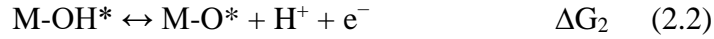
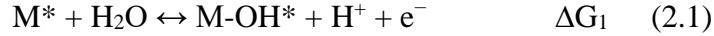
For example, spherical water particles with an initial diameter of $\sim 5 \mu\text{m}$ are obtained at a frequency of ~ 2 MHz. In the hot zone of the furnace, the solvent evaporates and contracts, and further heating leads to phase formation (supersaturation on the surface of the droplet). The porosity and morphology in the SP synthesis method depends on the nature of the precursors as well as the pyrolysis temperature, since at higher temperatures the evaporation rate of a solvent is fast and droplet shrinks rapidly, which leads to dense solid particles [98]. The formation of dense solid particles or hollow shells depends on the rate of solvent evaporation and on the solubility of the precursor, which, in turn, depend on the viscosity and surface tension [93]. Additionally, methods based on the decomposition of organic substances, such as sucrose, glucose, etc., with CO , CO_2 , H_2 , H_2O being released, can be applied to change the morphology of the particle. The volatile species create holes and pores in the particles [99].

Moreover, USP synthesis allows to obtaining porous carbon powders, that have comparable electrocatalytic performance with the well-known Vulcan Carbon XC-72, which is actively used in conjunction with metals and oxides in the reaction of oxygen evolution and reduction. As well as mixtures of porous transition metal oxide particles with carbon can be obtained in one stage using USP with sucrose as a carbon source and metal salts pyrolyzed in the H_2/N_2 gas stream [100]. Although such features of spray pyrolysis method as obtaining a mixture of a catalyst with carbon are not considered in

this thesis, they can be used in the future to simplify preparation of highly efficient catalysts.

2.5 Kinetics and mechanisms of oxygen evolution reaction on oxide surfaces

In recent literature, it was established that the OER can proceed through two different mechanisms: the conventional adsorbate evolution mechanism (AEM) and the lattice-oxygen-mediated (LOM) mechanism [101],[49]. AEM is typically assumed to involve four concerted proton-electron transfer (CPET) reactions centered on the active sites (metal cation), as described in equations below for acidic (2.1)–(2.4) and alkaline (3.1)–(3.4) conditions, respectively [101],[48]:



Every reaction step involves a kinetic energy barrier with the slowest step being referred to as the rate-determining step (RDS).

In AEM, in alkaline solution, OH^- first adsorbs on the surface and forms OH^* intermediate (eq. 3.1). The adsorbed OH^* species then undergoes subsequent deprotonation to form O^* (eq. 3.2). The following O–O bond formation step allows O^* to react with another OH^- to form the HOO^* intermediate (eq. 3.3). In the final step, O_2 is evolved through the deprotonation of HOO^* with the regeneration of the surface metal active site (eq. 3.4).

Each elementary step requests ideally 1.23 eV to form the next intermediate, as shown in Figure 4 for ideal catalysts, but real catalysts usually have a higher energy barrier for a certain step.

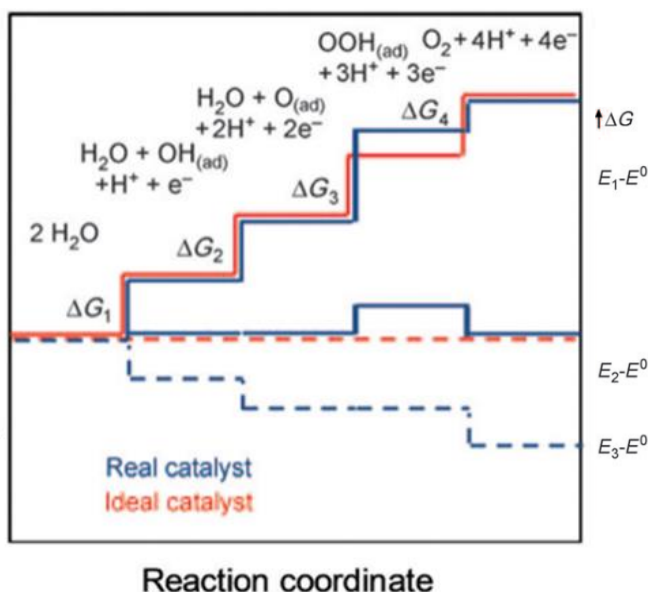


Figure 4. Gibbs free energies (vertical axis) of reactive species and intermediates versus reaction coordinate, for ideal (red) and real (blue) catalyst at different electrode potentials ($E_1 < E_2 < E_3$); ($E^0 = 1.23 \text{ V}$ standard OER potential). Reprinted from ref. [102]. Copyright 2010, Wiley-VCH Verlag GmbH&Co. KGaA, Weinheim.

The OER might be limited by any of these four reaction steps. The most positive Gibbs free energy determines the overpotential. At the potential $E_1 - E^0$ all steps are uphill and the reaction is unfavorable. At the potential $E_2 - E^0$ red dashed line shows that for an ideal catalyst there is no uphill in free energy at equilibrium potential = 1.23V, while for a real catalyst (blue line) the step ΔG_3 is uphill i.e. additional overpotential is needed to overcome this energy barrier and launch the reaction. At a higher potential $E_3 - E^0$ all reaction steps are downhill in free energy and the reaction proceeds freely.

2.6 Descriptors of activity in OER

It is worth noting that there were a lot of attempts to find appropriate specific descriptors, which correlate with the activity in OER. In 1955, the pioneers Ruettschi and Delahay observed a correlation between the OER activity and the energy of the bond strength ($M-OH_{\text{adsorbed}}$) for metals [103], which was confirmed later by Subbaraman *et al.* for (oxy)hydroxide systems, where activity follows the order $Ni > Co > Fe > Mn$, with increasing strength of the $M-OH_{\text{adsorbed}}$ interaction [104]. In early work, Trasatti reported the enthalpy change of the transition of the oxide from a lower to a higher oxidation state as a descriptor, where the smaller overpotentials were demonstrated by the oxides of Ir, Ru, and the higher by transition metals [105].

Other descriptors are related to electronic structure (for complex oxides), like the number of d electrons on transition metal. This descriptor was proposed by Bockris and Otagawa in 1984, as they found a correlation between the OER activity and the electronic

structure for ABO_3 perovskite materials (Figure 5a) [106]. They observed an increase in the OER activity with changing the B-site cations in the following order: $V < Cr < Mn < Fe < Co < Ni$. Additionally, substituting La^{3+} for Sr^{2+} was shown to provide a positive effect on the OER activity, due to the increased number of oxygen vacancies (adjusting B-OH bond strength). For Sr-doped mixed oxides, Matsumoto and Sato also highlighted the importance of degree of overlapping between the d -orbitals of the transition metal and oxygen p -orbitals [107].

In 2011 Norskov and Rossmeisl groups analyzed large range of complex oxides through calculation of scaling relations between the adsorption free energies of different adsorbates (intermediates): O^* , OH^* , and OOH^* for certain crystal plane orientation [48]. They assumed, that all intermediate steps are described as single proton transfers, coupled with single electron transfers with four intermediate steps, and found that the difference of binding energies ΔG on the free energy diagram (similarly to Figure 4) between OOH^* and OH^* species ($\Delta G^0_{OOH^*} - \Delta G^0_{OH^*}$) on the various oxides e.g. perovskites, rutiles, anatase, is approximately constant and equals ~ 3 eV on average, and it does not depend on where the binding energy of O^* level is located relative to OH^* or OOH^* . While for the ideal catalysts the difference should be 2.46 eV (i.e. 3.69-1.23 eV), it is not feasible in the real catalysts, and implies the impossibility of creating a catalyst with 100% efficiency. This relationship leads to volcano-shaped curve, in terms of OER overpotential, determined by the O^* adsorption energy, and allows predicting the electrocatalyst activities for a large range of oxides (Figure 5b). The OER kinetics for the materials on the left leg of the volcano in the Figure 5b (strong oxygen binding and the

O* energy level is placed closer to OH*, see Figure 4) are limited by the transformation of O* into OOH*, while the kinetics on the right leg (weak oxygen binding, the O* energy level is placed closer to HOO*) are limited by the transformation of OH* into O*. Based on this analysis, the steps ΔG_2 or ΔG_3 act as the potential RDS for most OER electrocatalysts, hence the difference $\Delta G_{O^*}^0 - \Delta G_{OH^*}^0$ or $\Delta G_{OOH^*}^0 - \Delta G_{O^*}^0$ was proposed as a universal descriptor to predict the activity of a material in OER.

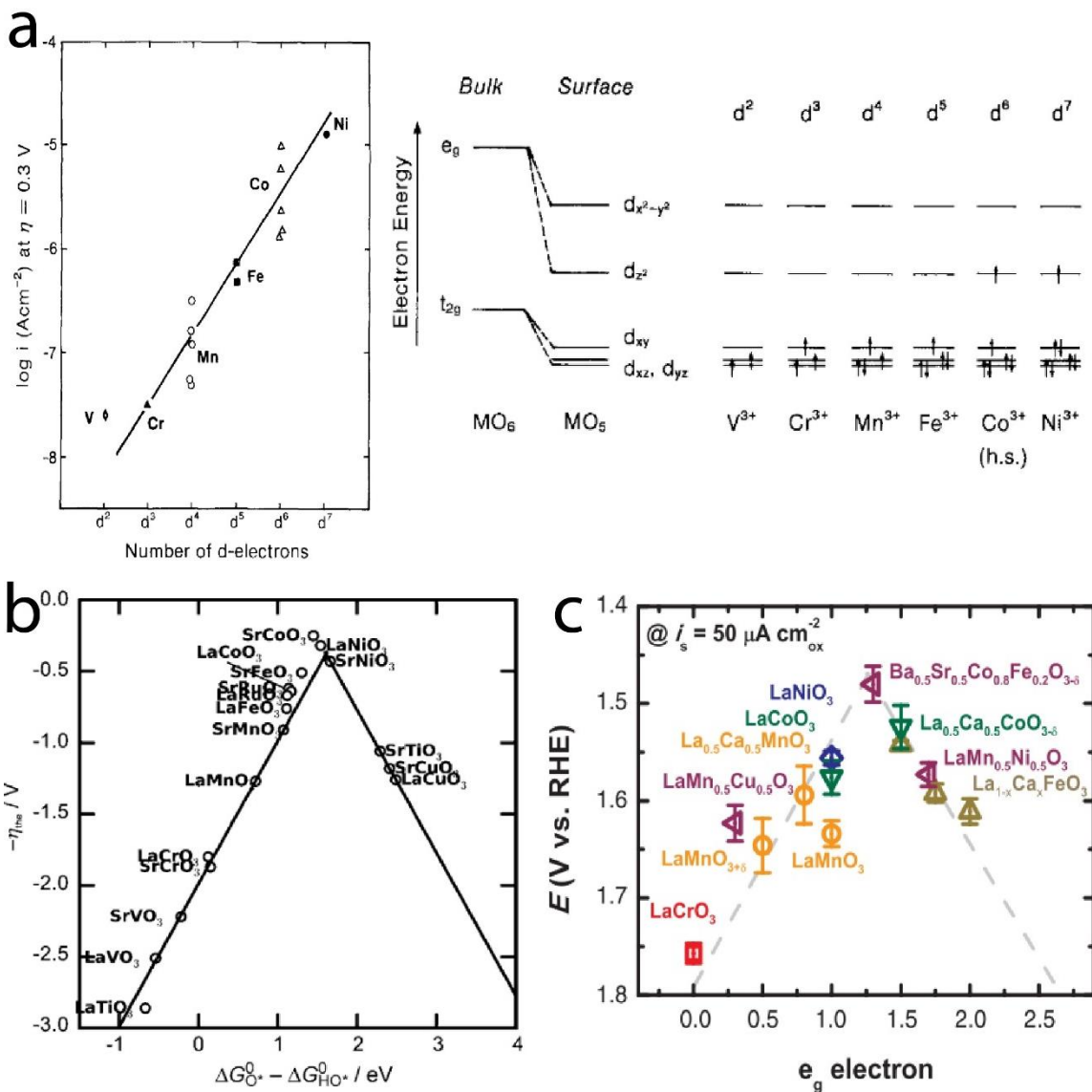


Figure 5. (a) OER current density on perovskites at 0.3 V overpotential vs number of d -electrons of B-cations in perovskites (left). Electronic structure, d -electron configuration of transition metal ions (M) at the surface of perovskites, the e_g levels split into $d_{x^2-y^2}$, d_{z^2} , the t_{2g} – into d_{xy} , d_{xz} , d_{yz} (right). Reprinted from ref. [106]. Copyrights 1984, ECS - The Electrochemical Society. (b) Volcano plot of the calculated overpotential (η) with the $\Delta G_{\text{O}^*}^0 - \Delta G_{\text{HO}^*}^0$ parameter as a descriptor. Reprinted from ref. [48]. Copyright 2011, Wiley-VCH Verlag GmbH&Co. KGaA, Weinheim. (c) Relationship between OER specific activity and e_g electron occupancy on B site transition metal for various perovskite catalysts. Reprinted from ref. [108]. Copyright 2011 by the American Association for the Advancement of Science.

Later, motivated by the success of the d -band theory as the activity descriptor for metal surfaces proposed by Bockris and Otagawa, descriptors based on the e_g electron occupancy were proposed (Figure 5c). For this purpose, the electronic configuration ($t_{2g}^x e_g^y$) is first determined based on the formal oxidation state of the transition metal at the B-site and their spin state. So, in the work ref. [108], the optimal value of the e_g electron occupancy was determined as ~ 1.2 , which should lead to optimal binding of the OER intermediates to the oxide surface and facilitate RDS (presumably 2 or 3 step). The determination of e_g orbital occupancy for oxides with two different B-site ions was based on a more active surface transition metal cation, under an assumption that the less active cation contributes negligibly. The analysis of the e_g orbital occupancy was chosen specifically [108], because the σ -bonded e_g orbitals have a stronger overlap with the O $2p$ orbitals of the oxygen-related adsorbate than the π -bonded t_{2g} orbitals. Presumably, it promotes more directly the electron transfer between surface cation and adsorbed reaction intermediates, which greatly influences the binding of oxygen-related intermediate species on B-sites and thus the OER activity [108]. In addition, for a more accurate prediction of the OER electrocatalytic properties based on the electronic structure, Shao-Horn's group also proposed descriptors such as $2p$ -band position relative to the Fermi level [10],[109], and metal-oxygen covalency (the energy difference between the metal $3d$ and oxygen $2p$ -band centers, also referred to as the charge-transfer energy [110]). These approaches simplified the whole complexity of OER process and do not consider real change in the surface of the electrocatalyst during the OER and the binding strength of reaction intermediates with the surface, just assuming some

correlation between catalytic activity for transition metal oxides and surface adsorbate binding energy of intermediates. In addition, it has also been shown that reducing the metal-oxygen covalency can reduce or even eliminate the energy barrier for electron transfer at the oxide-electrolyte interface, which facilitates the kinetics of OER [110]. Thus, such approaches make it possible to partially establish a connection between the bulk electronic structure and catalytic activity. They can be useful if the surface of electrocatalysts is stable (or has minor surface changes) during the OER and other comprehensive methods of analysis are used to evaluate and interpret electrochemistry. It was experimentally demonstrated that Ni-based lanthanum perovskite materials have the highest OER activity ($\text{Ni} > \text{Co} > \text{Mn} > \text{Fe} > \text{Cr}$). The wide application of DFT computational methods to rationalize the OER thermodynamics allowed establishing correlations between the activity and the electronic structure, and metal-oxygen covalency was proposed as one of the most appropriate activity descriptor (among the analysis of the bulk electronic structure) [51],[109],[110],[111],[112]. Yet, these approaches presume stable surface structure and do not account for possible surface structure evolution during OER, which might change the nature of the active sites.

2.7 Lattice oxygen mediated mechanism

The OER mechanism involving the oxygen atoms of the oxide crystal lattice is referred to as lattice oxygen-mediated mechanism and denoted in literature as LOM/LOER (lattice oxygen evolution reaction). In contrast to AEM, this mechanism

assumes that at least one of the four OER steps is not a concerted proton-electron transfer (CPET) (Figure 6a). This mechanism was first discussed for OER on perovskite materials in alkaline solution in 2016 for LaBO_3 (B is Ni, Fe, Co, Mn) by Rong *et al.* [113], for Sr-doped LaCoO_3 by Mefford *et al.* [9] and later in 2017 by Grimaud *et al.* [49]. It was suggested that the activation of the LOM mechanism occurs due to a decrease in the enthalpy of O vacancies formation, which depends on the nature of the B atoms and their nominal oxidation state. Thus, oxygen vacancies that are formed after the heterovalent substitution of La^{3+} for Sr^{2+} in Co-based perovskite make it possible to switch the mechanism from AEM to LOM. The increase in the degree of substitution was demonstrated to have a positive effect on the OER activity. This was rationalized by higher covalency of metal oxygen bonding (i.e. smaller energy difference between metal 3d-band and O 2p-band center, when oxidation state of Co is increased) and decreasing the O vacancies formation energy in Sr-substituted perovskite materials. Previously, Deml *et al.* in 2014 demonstrated the strong correlation between the oxygen vacancy formation energies (E_V) and the position of the O 2p band center relative to the Fermi level for the compositions $\text{La}_{1-x}\text{Sr}_x\text{Mn}_y\text{Al}_{1-y}\text{O}_3$, where an increase in the degree of Sr-substitution led to a shift in E_F closer to O 2p-band and a decrease in E_V , and an increase in E_V with increase in the Mn-substitution, when Sr-substitution is constant and $x(\text{Sr}) > x(\text{Mn})$, which leads to an increase in the position of E_F relative to the O 2p-band center. No change in E_V was observed with increasing Mn-substitution when $x(\text{Mn}) \geq x(\text{Sr})$ and E_F changed negligibly [114]. Studies on other perovskite compounds such as $\text{SrCoO}_{3-\delta}$, $\text{Ba}_{0.5}\text{Sr}_{0.5}\text{Co}_{0.8}\text{Fe}_{0.2}\text{O}_{3-\delta}$ also showed that a high content of oxygen vacancies, together

with close O $2p$ -band center to the Fermi level and high M-O covalency are typically associated with a higher OER activity, which was suggested to be a signature of LOM for these perovskite catalysts [109],[115]. The LOM mechanism implies a reversible formation of the surface oxygen vacancies associated with high surface exchange kinetics that results in a significant enhancement of catalytic activity in the OER [9],[73]. Thus, the primary role of heterovalent substitution of A-site cations (cations in lower oxidation state, e.g. +2) stems from decreasing the electron donation ability of the transition metal cations and implementing oxygen vacancies as a charge compensation mechanism. This leads to a shift of the O $2p$ -band towards the Fermi level and decreasing oxygen vacancy formation energy, which has positive effect on catalytic activity [109],[9].

The distinction in the LOM and AEM mechanisms was suggested to be rooted in the details of the complex oxide electronic structure. When the transition metal $3d$ band is located above the oxygen $2p$ band, the metal center of the oxides acts as the adsorption site and redox center, allowing water oxidation to follow AEM, with reaction intermediates originating from the electrolyte (eq 2.1-3.4). In the LOM mechanism, when the metal-oxygen covalency in the material is increased, the energy of the $3d$ band of the transition metal (see red projected density of states (PDOS) in Figure 6c) is shifted down into the O $2p$ -band (blue PDOS), resulting in the formation of a bond between the adsorbed intermediate $-O^*$ with the lattice O, followed by the release of OO and the generation of O-vacancies in the lattice (Figure 6c). This configuration has a lower Gibbs free energy compared to generally proposed adsorbed $-O$ intermediate in AEM (eq. 3.2), thus LOM pathway is energetically favorable [113],[9]. Importantly, it is assumed that

lattice oxygen is reversibly refilled with the OH^-_{aq} from the electrolyte and the perovskite surface is preserved [9],[49],[116].

One of the notable experimental observations in favor of LOM is the pH-dependence of the OER activity (on the RHE scale), which suggests the non-CPET steps during OER, compatible with LOM. Such pH-dependence of the catalytic activity was observed by Grimaud *et al.* (Figure 6b) for $\text{La}_{1-x}\text{Sr}_x\text{CoO}_{3-\delta}$ ($x \geq 0.4$), $\text{Pr}_{0.5}\text{Ba}_{0.5}\text{CoO}_{3-\delta}$ and $\text{SrCoO}_{3-\delta}$, for which up to 37 monolayers of oxide (~ 14 nm) were suggested to be involved in the LOER process (as confirmed by ^{18}O released from isotope labeled perovskites in the OER via online electrochemical mass spectroscopy) [49]. For undoped LaCoO_3 , the OER activity was pH-independent, which suggests an AEM [49].

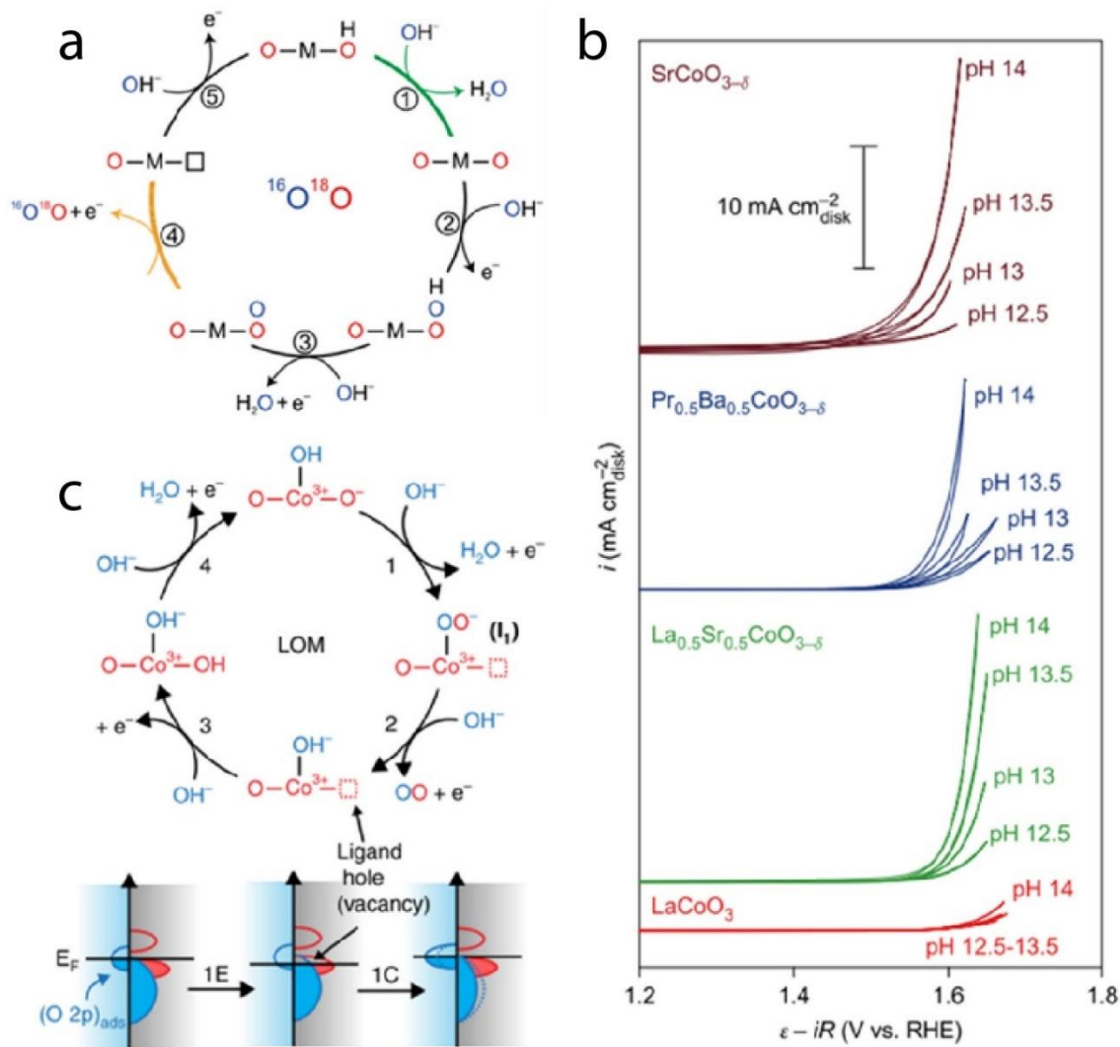


Figure 6. (a) Possible OER mechanism with the non-concerted proton-electron transfer that evolve $^{16}\text{O}^{18}\text{O}$ ($^{34}\text{O}_2$). Oxygen from the electrolyte in blue and from the oxide lattice in red, electron-transfer step in yellow, proton-transfer step in green. (b) pH-dependent CVs of perovskite electrocatalysts. Reprinted from ref. [49] with permission, copyright 2017, Macmillan Publishers Limited, part of Springer Nature. (c) Another possible OER mechanism, where lattice species are shown in red and electrolyte species are shown in blue. Below, in the PDOS diagrams, the electrolyte species are shown to the left of the energy axis (blue background) and the crystal PDOS are shown to the right (grey background). Step 1 of the LOM is separated into an electrochemical (1E) step in which the ligand hole is generated and a chemical step (1C) in which the lattice oxygen is exchanged into the adsorbed intermediate. Reprinted from ref. [9] licensed under a Creative Commons Attribution 4.0 International License.

It is worth noting that later research provided serious implications against LOM, as a major factor determining the enhanced electrocatalytic activity of Sr-doped perovskites. Recent work by Markovic group on the electrocatalytic activity of $\text{La}_{1-x}\text{Sr}_x\text{CoO}_3$ ($x = 0.3$) materials demonstrated that pH dependence of OER activity (on the RHE scale) is not related to the difference in OER mechanisms (CPET vs. non-CPET steps). The OER currents were shown to depend not on the solution pH directly, but primarily on the concentration of Fe ions in the alkaline electrolyte, which are a typical impurity in commercial KOH and NaOH solutions for water electrolysis [117],[118]. For purified Fe-free electrolytes or the same iron content across the different pH, no dependence of the OER activity on pH was observed for $\text{La}_{0.7}\text{Sr}_{0.3}\text{CoO}_3$ on the RHE scale (Figure 7a).

It was further suggested that the Fe impurities form active sites, which result in electrocatalytic activity enhancement [119]. A crucial point of this study is that the catalytic surface is not the Sr-doped LaCoO_3 surface itself, but the restructured (oxy)hydroxide surface layer (CoO_xH_y) formed during the OER. This restructured layer interacts with the trace amounts of Fe ions in the electrolyte, which creates dynamically stable active sites. The DFT data revealed that Fe adsorption energy on the perovskite surface is less negative compared to Fe adsorption energy on perovskite-supported CoOOH monolayer. This study seriously challenges the notion of LOM as a mechanism, which occurs on the pristine perovskite surface. Clearly, cation leaching, surface restructuring, and changes of the nature of the catalytically active site should be carefully considered before any conclusions about the electrocatalytic mechanisms can be drawn.

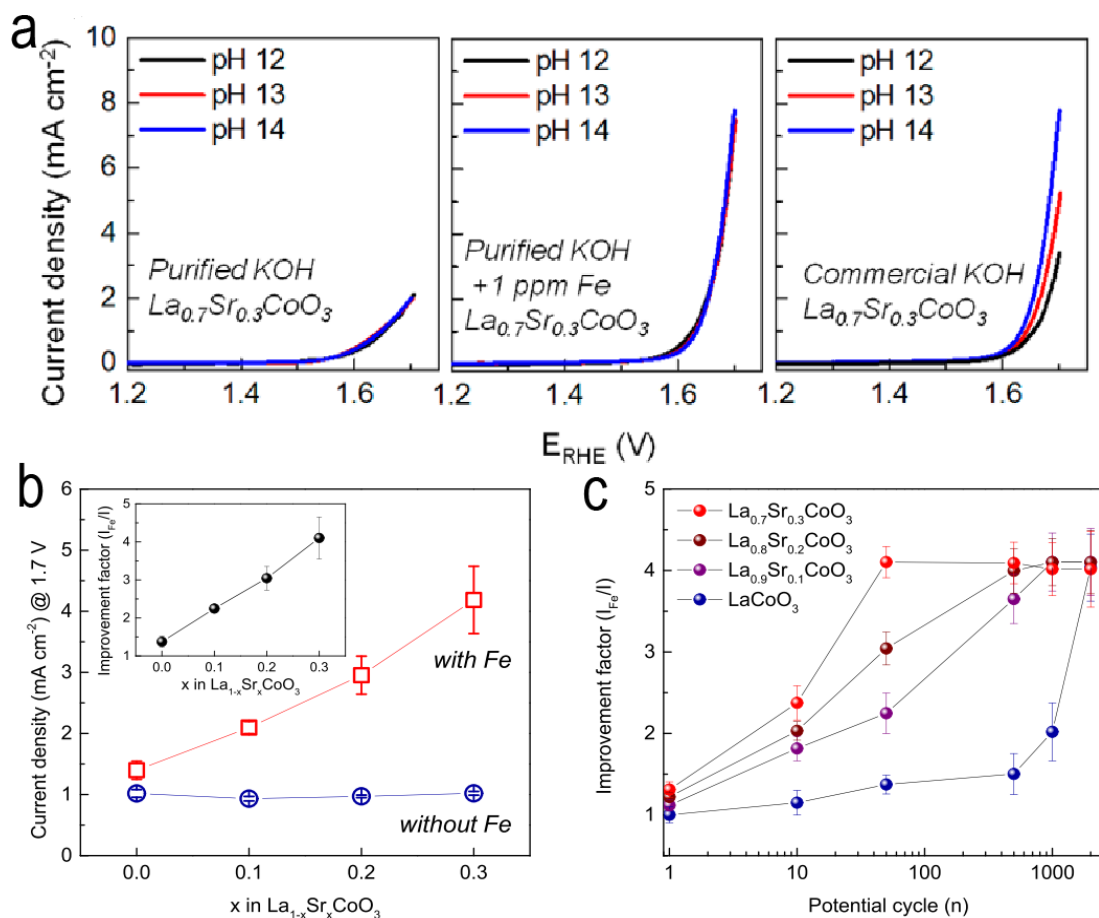


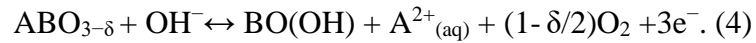
Figure 7. (a) OER at different pH in purified electrolyte, in the electrolyte with a fixed amount of $\text{Fe}_{(\text{aq})}$ and in the unpurified commercial electrolyte. (b) OER current density measured at 1.7 V vs RHE for $\text{La}_{1-x}\text{Sr}_x\text{CoO}_3$ samples pre-cycled 50 times up to 1.7 V as a function of the Sr-doping level for the electrolytes with and without 0.1 ppm of $\text{Fe}_{(\text{aq})}$. Inset shows the increase in currents for pre-cycled sample compared to the initial currents, due to the presence of Fe ions. (c) Fe-induced OER improvement factor (ratio between the current density with and without Fe ions in the electrolyte at 1.7 V) as a function of cycle number for $\text{La}_{1-x}\text{Sr}_x\text{CoO}_3$ ($x = 0.1, 0.2, 0.3$). Reprinted from ref. [119]. Copyright 2021, American Chemical Society.

Thus, an increase in the metal-oxygen covalency, O 2p shift relative to the Fermi level and decrease in the energy of vacancy formation due to the substitution of La^{3+} for Sr^{2+} in the perovskite structure, as noted in the above works, seemingly correlates with the rate of irreversible perovskite surface reconstruction (which apparently always takes place)

due to leaching of the A-site cation and the formation of an (oxy)hydroxide layer based on the B-site cation, which leads to a stronger interaction with Fe ions in the electrolyte. After all, as it turned out, even LaCoO_3 with a sufficiently large separation of the O $2p$ band from the Fermi level (~ 2.5 eV) [109] is able to change the surface during cycling (see further section 2.9). The continuous process of Fe (and B-site cations) dissolution/redeposition during OER on restructured perovskite surface prevents deeper amorphization of the electrocatalyst material and maintains high activity in OER. Markovic group demonstrated that the activation of Sr-doped $\text{La}_{1-x}\text{Sr}_x\text{CoO}_3$ depends on the synergy between the presence of trace amounts of $\text{Fe}_{(\text{aq})}$ in the electrolyte and the degree of Sr doping in the A-site. In the electrolyte purified from Fe ions, all samples, regardless of Sr doping amount, show essentially the same OER activity (notably, after longer cycling the differences will become noticeable due to irreversible surface structure changes). A significant difference in the OER activity is observed only in the presence of $\text{Fe}_{(\text{aq})}$ ions in the electrolyte, Figure 7b. Moreover, after more than 2000 cycles in the electrolyte with $\text{Fe}_{(\text{aq})}$ ions, regardless of the doping level, the activity of all the catalysts $\text{La}_{1-x}\text{Sr}_x\text{CoO}_3$ ($x = 0.1, 0.2, 0.3$) became the same (Figure 7c). These results highlight the importance of factors such as the number of cycles and concentration of trace Fe ions for an accurate analysis of the electrocatalytic mechanisms.

The fact that small amounts of Fe adsorbed from the electrolyte strongly affect the OER activity and stability of electrocatalysts has also been reported for the (oxy)hydroxides systems like $(\text{Ni,Fe,Co})\text{O}_x\text{H}_y$. For these electrocatalysts, enhanced activity can also be attributed to the formation of dynamically stable active centers

[120],[121]. Markovic's group carried out controlled experiments with $\text{Fe}_{(\text{aq})}$ ions in the electrolyte and emphasized that for perovskite catalysts the Fe species in the electrolyte are an essential component, since these species provide the dynamically stable active sites [120],[119]. Additionally, it should be noted that perovskites as $\text{Ba}_{0.5}\text{Sr}_{0.5}\text{Co}_{0.8}\text{Fe}_{0.2}\text{O}_{3-\delta}$ [122],[123], $\text{SrTi}_{0.1}\text{Fe}_{0.85}\text{Ni}_{0.05}\text{O}_{3-\delta}$ [124] and LaNiO_3 [125],[126] with a surface modified by (oxy)hydroxides demonstrated better catalytic properties and stability than bare perovskites without (oxy)hydroxide modification. Earlier in 2017 Fabbri *et al.* proposed a similar idea with dynamic reconstruction of the perovskite $\text{Ba}_{0.5}\text{Sr}_{0.5}\text{Co}_{0.8}\text{Fe}_{0.2}\text{O}_{3-\delta}$ surface during the OER, which is accompanied by the A-site cation dissolution and B-site cations dissolution/redeposition, which results in the growth of a self-assembled (Co/Fe) (oxy)hydroxide active layer [127]. Based on the knowledge available today, we can suggest that the LOER on perovskites is a part of an irreversible surface reconstruction process, which can be described by the following equation [127]:



After this initial surface reconstruction, the active surface is the formed B-site cation (oxy)hydroxide. This new active surface can be dynamically stable if the concentration of Fe species in electrolyte is sufficiently high (close to saturation limit, otherwise, with $\text{Fe}_{\text{aq}} \ll \text{Fe}_{\text{saturation}}$ cations will be leached/dissolved during OER and not redeposited).

2.8 (Oxy)hydroxides as active OER surface in alkaline media

As (oxy)hydroxide layers are presumably responsible for the OER activity enhancement under the alkaline conditions, it is essential to properly understand their electrochemical behavior. Investigation of nickel (oxy)hydroxides electrocatalytic properties is particularly important for revealing the nature of the electrocatalytic surfaces of Ni-based compounds. For instance, it was reported that pure metallic nickel surface becomes covered by thin layers of NiO or Ni(OH)₂ instantaneously upon immersion into 1M KOH electrolyte. On the anodic scan the peak labeled 'a' corresponds to the formation of α -Ni(OH)₂ (subsequent reduction corresponds to the cathodic peak 'a'), which is further irreversibly converted into β -Ni(OH)₂ (region B along the abscissa, Figure 8) [128]. β -Ni(OH)₂ is further oxidized to β -NiOOH, which is accompanied by the change in Ni oxidation state from 2+ to 3+. During the electrochemical cycling involving Ni²⁺(OH)₂/Ni³⁺OOH redox (region C in Figure 8) the thickness of the surface hydroxide and inner oxide layers (NiO between the hydroxide and the Ni substrate) increases [129].

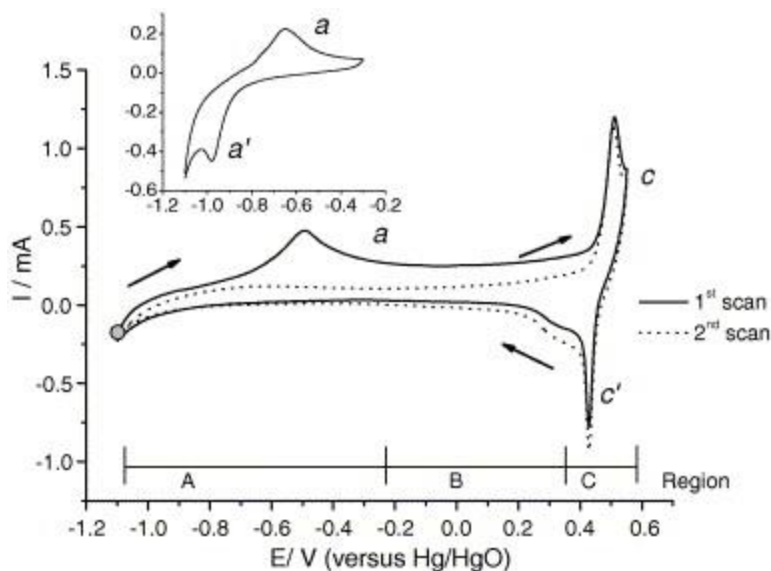


Figure 8. Cyclic voltammograms of Ni (1 1 1) in 1 M KOH. From ref. [128]. Copyright 2005, Elsevier B.V.

With an increase in the potential, β -NiOOH can transform into the γ -NiOOH. Such a chemical formula (γ -NiOOH) is widely used in the literature, however this designation is used for simplicity because γ -NiOOH structure has a large interlayer distance, and water molecules and alkali ions can intercalate into the (oxy)hydroxide, making it difficult to determine the exact composition. A more accurate representation to take into account the variable stoichiometry of the compound would be γ -NiOOH_xA_y*z(H₂O) (where A - alkali metal cations and the nickel oxidation state reaches +3.66 when $x = 0$, $y = 0.33$, $z = 1$), which indicates the existence of a significant number of nickel centers in the formal oxidation state of +4 [130],[131],[132]. Thus, the available experimental data indicate that the surface of metallic Ni is transformed into nickel oxide/hydroxide and further into (oxy)hydroxides upon cycling in alkaline solutions. Ni-

based perovskites are presumed to undergo similar surface transformations under the alkaline OER conditions [133],[134].

Ni-M double hydroxides (DH) (where M can be Cr, Mn, Fe, Co, Cu, and Zn) demonstrate enhanced OER activity when appropriate dopants are introduced. Diaz-Morales *et al.* found that the difference between the adsorption energies of O* and OH* for NiO model is slightly shifted by -0.1 eV from the optimal thermodynamic value and by +0.24 eV for NiOOH model, which opens wide possibilities for OER enhancing via doping, from the point of the difference in the adsorption energies of $\Delta G^0_{O^*} - \Delta G^0_{OH^*}$ [135]. They assumed two cases for DFT analysis of Ni-M DH, first when the second transition metal site was the active site, not Ni, the authors found that doping 50 at.% with Mn, Fe, Co results in optimal thermodynamic value of $\Delta G^0_{O^*} - \Delta G^0_{OH^*}$ for the increased OER activity, while Cr, Zn, Cu doping demonstrates less optimal $\Delta G^0_{O^*} - \Delta G^0_{OH^*}$ and should result in a higher overpotential (Figure 9a). The second case, when Ni itself was the active site, doping with Cr should lead to optimal adsorption energies $\Delta G^0_{O^*} - \Delta G^0_{OH^*}$ and, correspondingly, to an increase in the OER activity, while other elements provide less favorable $\Delta G^0_{O^*} - \Delta G^0_{OH^*}$. Further, electrochemical experiments are generally consistent with DFT analysis of adsorption energies ($\Delta G^0_{O^*} - \Delta G^0_{OH^*}$) and demonstrated that doping Ni DH with 50 at.% of Cr, Mn, and Fe enhances activity in OER, while doping with Co, Cu, and Zn results in an increase of the overpotential (Figure 9b) [135]. The Ni(OH)₂ (or equivalently NiOOH) doped samples demonstrated the following increasing trend in OER activity (50 at.% of doping element): Zn-Ni(OH)₂ < Co-Ni(OH)₂ < Cu-Ni(OH)₂ < undoped Ni(OH)₂ < Mn-Ni(OH)₂ < Cr-Ni(OH)₂ < Fe-

Ni(OH)₂ (Figure 9b). Another study by Burke *et al.* [136] reported the following trend in OER activity for (oxy)hydroxides: MnO_xH_y < NiO_xH_y < CoO_xH_y < FeO_xH_y < Co-FeO_xH_y < Ni-FeO_xH_y (Figure 9c). In both studies, the best performance was established for Ni-Fe compositions. Similar observation is also valid and for mixed LaNi_xFe_{1-x}O₃ perovskites, which have a better performance compared to LaNiO₃ and LaFeO₃ [66],[79].

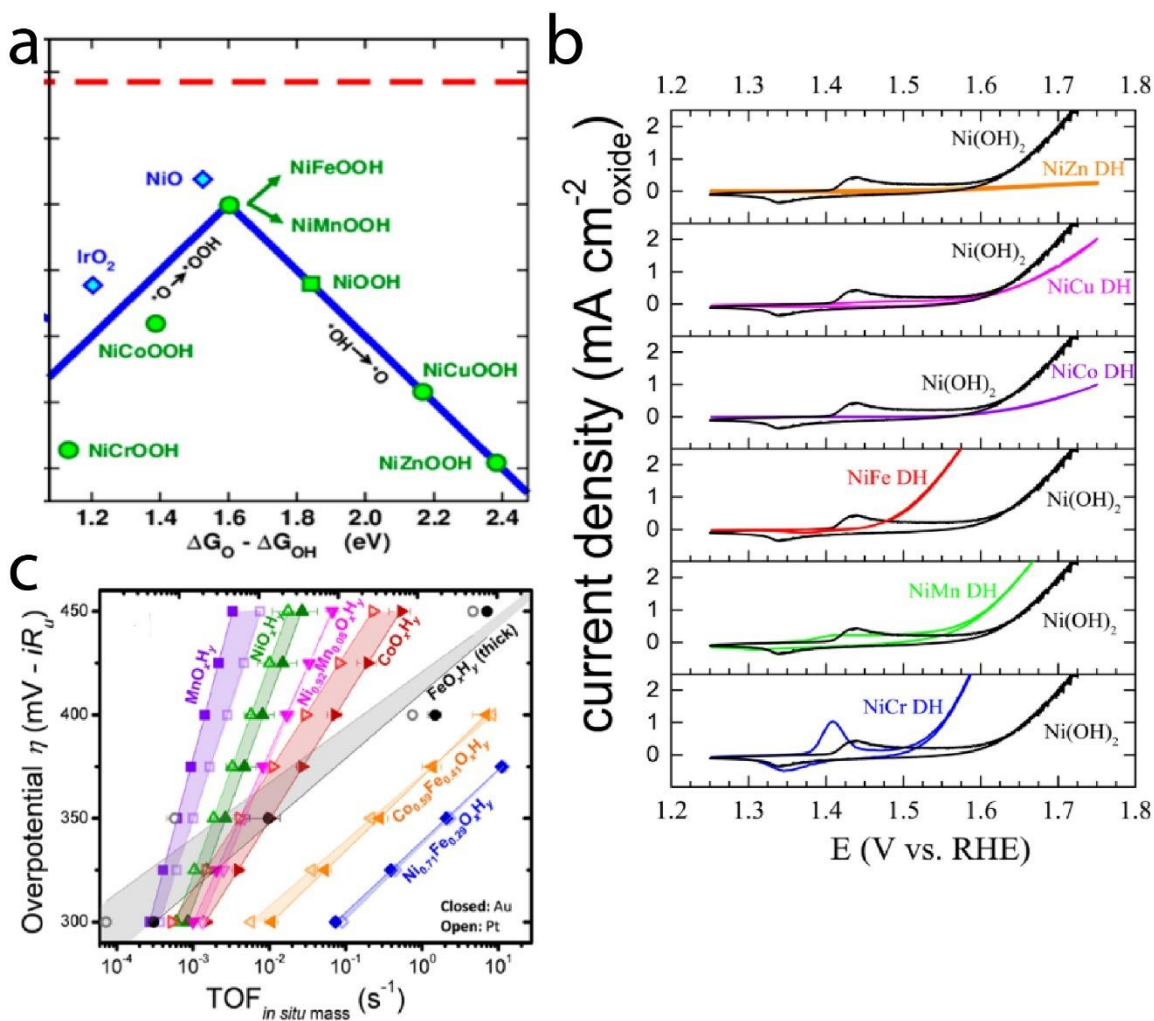


Figure 9. (a) Sabatier-type volcano plot for NiOOH doped with Cr, Mn, Fe, Co, Cu, and Zn. (b) CVs of nickel-based DH immobilized on Au in 0.1 M KOH. Reprinted from [135]. Copyright 2015, American Chemical Society. (c) Steady-state activity trends as a function of potential for (oxy)hydroxides on Au (solid) and Pt (open) quartz crystals. TOF_{in situ} is calculated from the total number of metal cations based on *in situ* mass measurements. Reprinted from [136]. Copyright 2015, American Chemical Society.

Some differences in trends reported by Diaz-Morales *et al.* and Burke *et al.* can be attributed to the different trace amounts of Fe ions in the electrolyte, as Burke *et al.* used a thoroughly purified from Fe_(aq) electrolyte. Later Chung *et al.* [120] confirmed that in Fe-purified 0.1 M KOH the order in the (oxy)hydroxides activity in OER is as follows: NiO_xH_y < CoO_xH_y < FeO_xH_y. It was found that Fe (oxy)hydroxide is the most active electrocatalyst, but also the most unstable one, due to high metal leaching rate. Once 0.1 ppm Fe was introduced into 0.1 M KOH electrolyte, the incorporation of Fe* into the Co- and Ni- (oxy)hydroxides was observed, which changed the OER activity trend: FeO_xH_y < Fe*-CoO_xH_y < Fe*-NiO_xH_y and led to increased stability. DFT results revealed the correlation between the Fe* coverage and higher OER activity [120].

2.9 Electron microscopy study of electrocatalytic surfaces after the OER

High-resolution transmission electron microscopy (HR-TEM) studies allow for an unprecedented detailing of the surface changes of the electrocatalytic materials. Figure 10 shows surface changes of La_{1-x}Sr_xCoO₃ (x=0, 0.3) perovskites after cycling up to 1.7 V in alkaline solution [119]. In the purified electrolyte after initial 50 CV cycles, the La_{1-x}Sr_xCoO₃ (x=0, 0.3) perovskites, remains crystalline to the surface, with formation of oxygen vacancies (red arrows), Figure 10b,g, while further cycling (50 CV) in the electrolyte with Fe_(aq) ions additionally to oxygen vacancies, surface becomes amorphous on the edge for the both pristine and Sr-doped sample Figure 10c,h. Note that the

captured area in Figure 10h for $x = 0.3$ is not at the edge, but there is clearly a much larger surface reconstruction (compared to $x=0$) after cycling with the formation of ordered oxygen vacancies and voids.

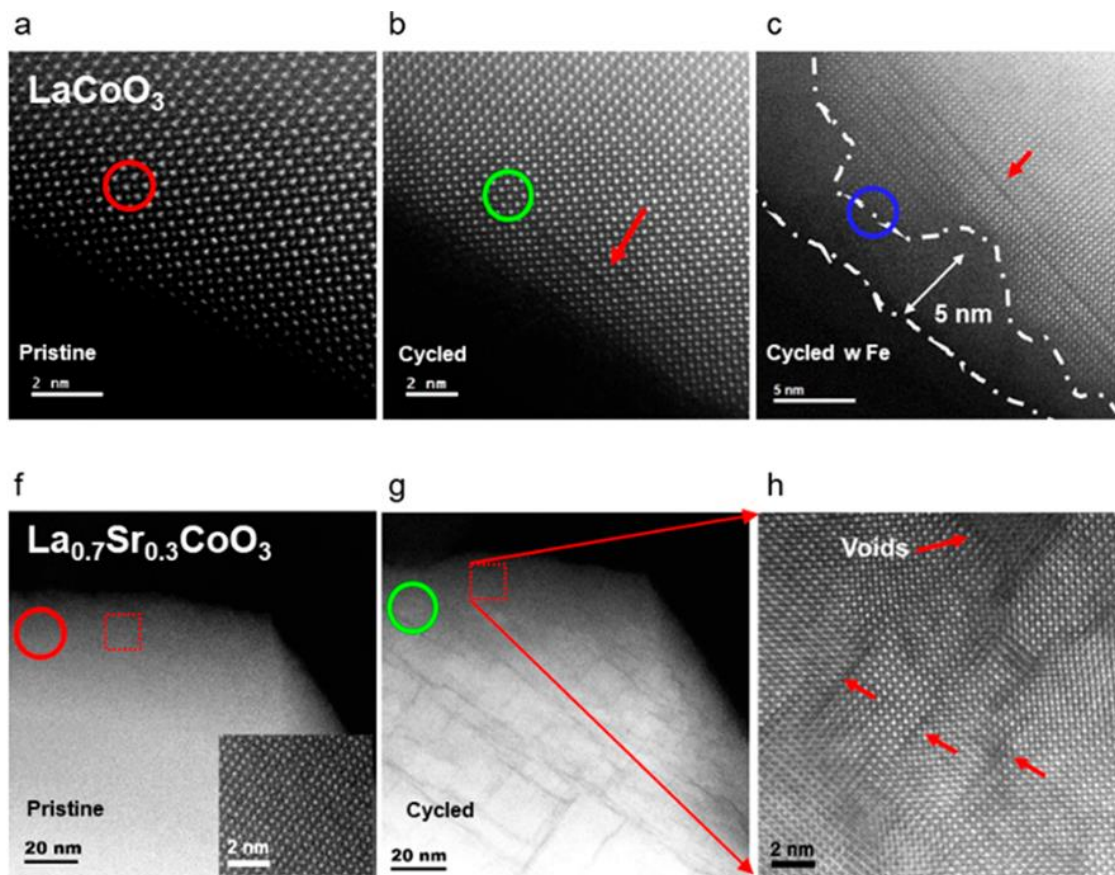


Figure 10. Surface reconstruction after cycling $\text{La}_{1-x}\text{Sr}_x\text{CoO}_3$ ($x = 0, 0.3$) materials in alkaline media. Identical location STEM images (a) of pristine LaCoO_3 , (b) after 50 cycles up to 1.7 V in Fe-free 0.1 M KOH, and (c) after an additional 50 cycles in KOH containing 0.1 ppm of Fe. STEM images (f) of pristine $\text{La}_{0.7}\text{Sr}_{0.3}\text{CoO}_3$ (inset: high magnification showing the lattice fringes indicative of the initial perovskite structure), (g) after 50 cycles up to 1.7 V in Fe-free 0.1 M KOH, and (h) after an additional 50 cycles in KOH containing 0.1 ppm of Fe. The circles represent the same area on the particle after different processing. The red square in “f” means the area that is zoomed in and pasted in the corner in the same figure. Figure “g” shows the same area for the cycled sample, but the zoomed area from the square is shown separately for illustration “h”. The arrows point to the oxygen vacancies in the crystal structure. Reprinted from ref. [119]. Copyright 2021, American Chemical Society.

The formation of oxygen vacancies was observed due to cycling in the OER region for $x=0, 0.3$ samples, and not due to the presence of Fe in the electrolyte. Since these images were taken *ex situ*, all conclusions about the dynamically restructured layer in this work were made in conjunction with the electrochemical behavior of the samples and the documented isotope exchange between ^{57}Fe in the perovskite sample and ^{56}Fe that was present in the electrolyte [119].

Nikolla *et al* have observed the similar pattern, with the formation of a surface amorphous layer in $\text{La}_{0.25}\text{Sr}_{0.75}\text{CoO}_3$ after 100 OER cycling up to 1.7 V. The ICP-MS studies and EDX analysis corroborates the Sr-deficient and Co-rich nature of the restructured surface shell, due to irreversible dissolution of alkaline-earth-metal cations [137]. This surface restructuring was observed in the Fe-free (<1 ppb Fe) electrolyte (Figure 10), yet also led to an increase in the electrocatalytic activity. It may seem that this contradicts the conclusions from Refs. [119] (Figure 7b), where no activity changes were observed for $\text{La}_{1-x}\text{Sr}_x\text{CoO}_3$ ($x = 0, 0.3$) samples in the Fe-free electrolyte. However, these two studies: [119],[137] used different Sr-substitution in the perovskite, i.e $x = 0.3$ and 0.75 , and activity was reported after a different number of OER cycles in the Fe-free electrolyte (50 and 100). Thus, from these two works, it can be emphasized that when studying the surface of the OER electrocatalyst, it is important to consider the influence of the doping level on the rate of surface restructuring, as well as the influence of the presence or absence of Fe ions on the activity and stability of the restructured layer. Previously, it was reported that Fe greatly slows down the leaching of other metal cations during OER [120], which affects the restructuring of the surface itself. With a sufficient

amount of Fe, a dynamic active layer is formed and the rearrangement of the surface layer of the initial catalyst is completed. Whereas, when Fe is absent, the dynamic layer is not formed, which provokes further leaching and the growth of an amorphous layer on the perovskite surface.

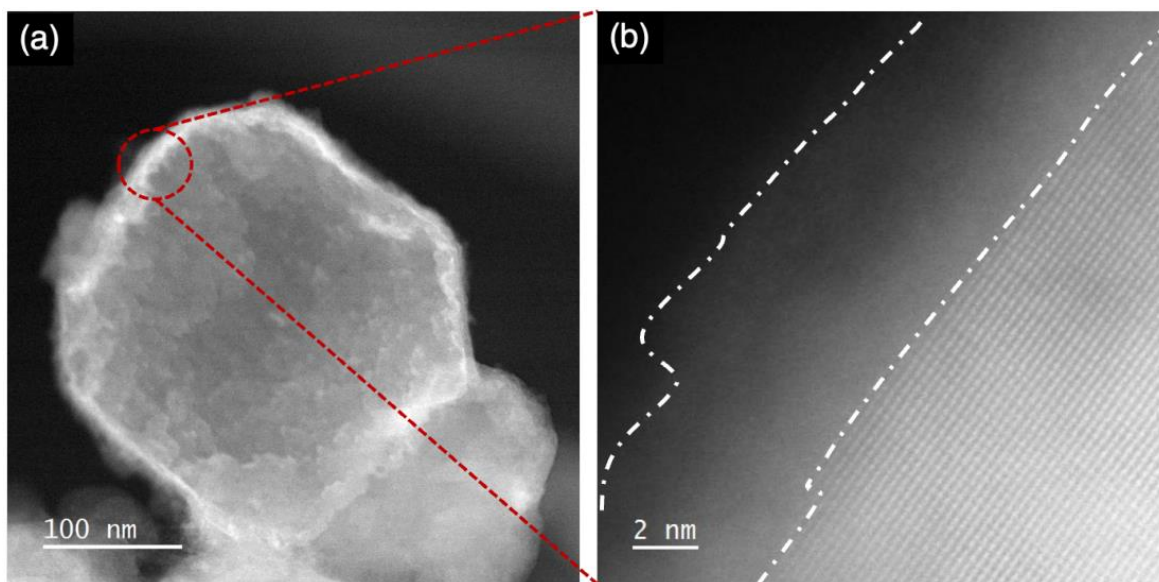


Figure 11. Surface structure of $\text{La}_{0.25}\text{Sr}_{0.75}\text{CoO}_3$ after cycling (a) HAADF-STEM and (b) atomic resolution HAADF-STEM images indicating the formation of a near-surface amorphous shell on the crystalline perovskite core, after 100 cycles in Fe-purified KOH. The amorphous shell is represented between the two white curves in (b). The thickness of the amorphous shell was found to be 6.5 ± 0.5 nm. Reprinted from [137]. Copyright 2021 The Authors. Published by American Chemical Society.

Another example of Fe-based perovskites (Figure 12) [138] demonstrates surface restructuring immediately after the deposition of the catalyst on the electrode surface (Figure 12b, e, h). An amorphous layer (~ 5 nm) was formed, most likely, at the stage of preparation of catalysts inks. Further deeper amorphization was observed after 100 OER cycles in case of Ca/SrFeO_3 resulting in a decreasing of OER activity, while

$\text{CaCu}_3\text{Fe}_4\text{O}_{12}$ material retained the initial thickness of the amorphous layer after cycling and showed an increased OER activity (Figure 12i). This emphasizes that with an identical B-site cation, and with a similar pattern of surface amorphization after deposition, further electrocatalytic OER properties still depend on the atomic and electronic structure of the host perovskite structure.

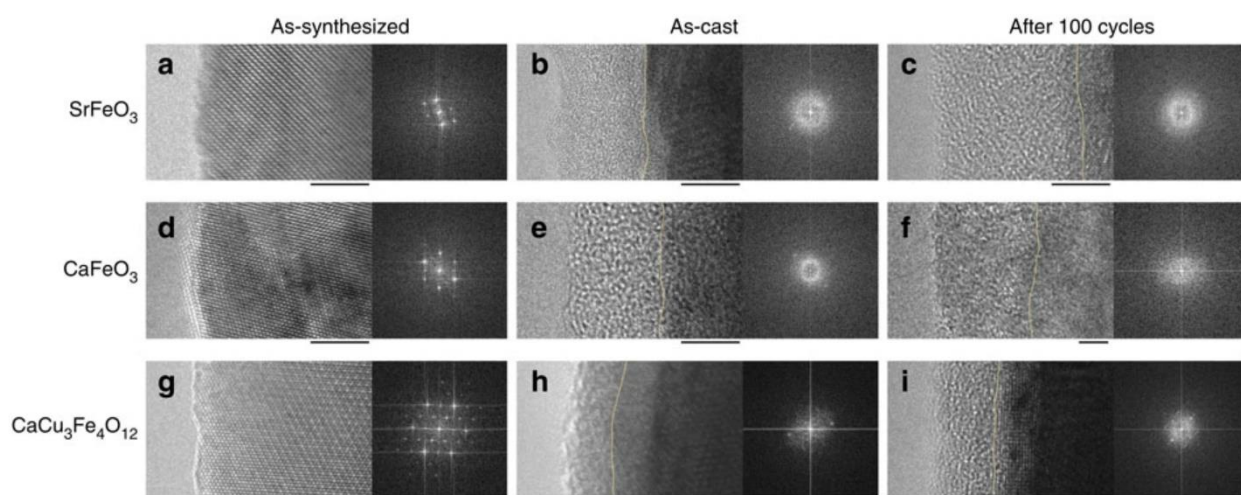


Figure 12. HRTEM and fast Fourier transform (FFT) images from surface regions of $10 \times 10 \text{ nm}^2$ of perovskite oxides before (a, d, g), after the deposition (b, e, h) and after the OER measurements (c, f, i). The boundaries between the crystalline and amorphous regions are divided by orange lines. Scale bar: 5 nm. Reprinted from ref. [138] licensed under a Creative Commons Attribution 4.0 International License.

The above images (Figures 10-12) clearly show the possibilities for characterizing the surface of electrocatalysts. By combining the capabilities of HR-TEM with electrochemical data, where changes on the surface of the electrocatalyst usually are reflected in the behavior of voltammograms, we can accurately identify the active sites and understand the nature of the catalytic activity.

2.10 Conclusions from the literature review

The OER activity of transition metal oxide-based materials, such as perovskites or oxyhydroxides can be quite successfully rationalized using such activity descriptors as M-O covalency, $\Delta G^0_{\text{O}} - \Delta G^0_{\text{OH}}$ energy difference, M-OH_{adsorbed} adsorption energy, e_g electron occupancy, etc. Each activity descriptor implies a specific electrocatalytic mechanism. However, most of the oxide surfaces are not stable under the aggressive conditions of alkaline OER. Surface structure changes may change the mechanism of the OER, which ultimately determines the activity and stability of the electrocatalyst. Currently, La_{1-x}Sr_xCoO₃ perovskites as OER catalysts have been studied in detail. Two OER mechanisms for these compounds have been hypothesized: AEM and LOM. Initially, the LOM mechanism was thought to be controlled by the nature of the A-site cation, which seemed to offer ample opportunity to tune OER activity. However, later it was shown that the perovskite surface undergoes restructuring regardless of the degree of Sr substitution, which is accompanied not only by the release of oxygen from the crystal lattice of the catalyst, but also by the leaching of cations from the perovskite structure. The presence of trace amount of Fe ions in the electrolyte turned out to be of extreme importance for both the activity and stability of the perovskite-based electrocatalysts. Current view is that the restructured surface is a thin layer of oxyhydroxides, which forms active sites once Fe is adsorbed onto it. This dynamically stable and active layer determines the OER activity of the perovskite electrocatalysts. Importantly, the timescale associated with the activity evaluation is also very important for an accurate mechanistic

analysis, as it is necessary to characterize both the long-term activity and the long-term stability of the electrocatalysts.

In this work, we focused on evaluating the electrocatalytic properties of a NiFe-based perovskite with heterovalent substitution of La^{3+} for Ca^{2+} , (since Sr-doped perovskites were mainly studied in the literature, which demonstrated ambiguous stability). In addition, this system is very promising for commercial use as an OER catalyst (because Ca is cheaper than Sr), but the reaction mechanism still remains poorly understood. In particular, it is not clear whether the same trends of surface restructuring and Fe adsorption would be important for the activity and stability of the chosen model material (La-Ca-Fe-Ni). As it was necessary to synthesize a homogeneous crystalline perovskite phase with relatively large specific surface area for correct analysis and interpretation of the nature of catalytic activity and stability, we employed a new USP synthesis method to obtain a material with high surface area and a unique hollow sphere morphology.

3. Methodology

3.1 Synthesis of perovskite catalysts (basic method)

The perovskites were synthesized using the ultrasonic spray pyrolysis (USP) method. The nitrates $\text{La}(\text{NO}_3)_3 \cdot 6\text{H}_2\text{O}$ (Neva Reactive, $\geq 99.0\%$), $\text{Ca}(\text{NO}_3)_2 \cdot 4\text{H}_2\text{O}$ (Neva Reactive, $\geq 98.5\%$), $\text{Fe}(\text{NO}_3)_3 \cdot 9\text{H}_2\text{O}$ (Alfa Aesar, $> 98.0\%$) and $\text{Ni}(\text{NO}_3)_2 \cdot 6\text{H}_2\text{O}$ (Sigma Aldrich, $\geq 97.0\%$) were dissolved in deionized water (MilliQ, $18.2 \text{ M}\Omega \cdot \text{cm}$) in the La:Fe:Ni = 1:0.25:0.75 molar ratio for $\text{LaFe}_{0.25}\text{Ni}_{0.75}\text{O}_3$; 1:0.7:0.3 molar ratio for $\text{LaFe}_{0.7}\text{Ni}_{0.3}\text{O}_3$ (LFN); La:Ca:Fe:Ni = 0.5:0.5:0.7:0.3 and 0.7:0.3:0.7:0.3 molar ratio for $\text{La}_{0.5}\text{Ca}_{0.5}\text{Fe}_{0.7}\text{Ni}_{0.3}\text{O}_{3-\delta}$ (LCFN5) and $\text{La}_{0.7}\text{Ca}_{0.3}\text{Fe}_{0.7}\text{Ni}_{0.3}\text{O}_{3-\delta}$ (LCFN3), respectively, to achieve the total concentration of 10 wt.%.

The solutions were ultrasonically sprayed using a household ultrasonic humidifier at $\nu = 2.64 \text{ MHz}$ and transferred with an air flow ($V_{\text{air flow}} = 172 \text{ mL s}^{-1}$) into a tubular furnace pre-heated to $1100 \text{ }^\circ\text{C}$ with the hot zone length of 360 mm. The resulting powders were collected with a Schott funnel with a glassy G4 filter. Then the powders were additionally annealed at 300, 450, 600, 800 and $1000 \text{ }^\circ\text{C}$ for 10 hours in air and furnace-cooled.

3.1.1 Synthesis of perovskite catalysts (modified method)

In order to prepare a homogeneous LCFN5 sample with large specific surface area (further denoted as LCFN5_m), the USP technique was further modified by adding sorbitol $\text{C}_6\text{H}_{14}\text{O}_6$ (Sigma Aldrich, $\geq 99.0\%$) to an aqueous solution of nitrates in 0.78 wt.%

concentration. Spray pyrolysis was conducted following the above-mentioned procedure, except for lower temperature of the tubular furnace of 850 °C and adding ozone O₃ to the air flow with the rate of 400 mg h⁻¹. The lower temperature of the furnace was chosen because of the exothermic reaction of sorbitol in an oxidative atmosphere of O₃. Final annealing of the powder was conducted at 600 °C for 5 hours in air.

3.1.2 Perovskite surface treatment

LCFN5_m S is the LCFN5_m sample, which was soaked for different periods of time in 1M NaOH solution in Teflon vial and further washed 3 times with water, where the soaking duration was selected based on the sensitivity of the applied analytical methods (see the description of the experiments).

3.2 Powder X-ray diffraction

Phase purity and the lattice parameters were determined by powder X-ray diffraction (PXRD) using a Huber G670 Guinier camera (transmission geometry, curved primary Ge (111) monochromator, Co K_{α1} radiation, $\lambda = 1.78896 \text{ \AA}$, image plate detector) and Bruker D8 Advance diffractometer (Bragg-Brentano geometry, Cu K_{α1,2} radiation, $\lambda = 1.54184 \text{ \AA}$, LYNXEYE XE detector). The Rietveld refinement was performed with the JANA2006 software [139].

3.3 Electron microscopy

Particle morphology was investigated using a FEI Helios NanoLab 650 scanning electron microscope. The samples for transmission electron microscopy (TEM) were prepared by grinding the powders with an agate mortar and pestle in ethyl alcohol and depositing drops of suspension onto a carbon film supported by a copper grid. Electron diffraction (ED) patterns, high-resolution TEM (HR-TEM) images, high angle annular dark field scanning transmission electron microscopy (HAADF-STEM) images, annular bright field STEM (ABF-STEM) images and energy-dispersive X-ray STEM-EDX compositional maps were acquired on a probe aberration-corrected FEI Titan Themis Z transmission electron microscope at 200 kV equipped with a Super-X system for EDX analysis.

3.4 Surface area analysis

Nitrogen adsorption analysis was performed with a Quantachrome Instruments NOVA 2000 high-speed surface area analyzer at 77 K. Prior to the measurements, the samples were degassed in dynamic vacuum for at least 12 h at 120 °C. The specific surface area was calculated using the Brunauer–Emmett–Teller (BET) method from the nitrogen adsorption data in the relative pressure range (P/P_0) from 0.05 to 0.30. For the LCFN5_m sample, the pore size distribution was calculated in the relative pressure range (P/P_0) from 0.4 to 0.98 by using the Barrett-Joyner-Halenda (BJH) method. Only the adsorption branch of the isotherm was used for the analysis.

3.5 ^{57}Fe Mössbauer spectroscopy

The ^{57}Fe Mössbauer spectra were collected using a constant acceleration spectrometer MS1104 (Rostov-na-Donu, RF) in a transmission mode with a $^{57}\text{Co}/\text{Rh}$ γ -ray source. Calibration of the spectrometer was performed using a standard α -Fe absorber. All isomer shift values (IS) are referred to α -Fe at room temperature. Spectra evaluation was performed using “UnivemMS” (Rostov-na-Donu, RF) and custom least squares fitting software with Lorentzian–Gaussian line shapes.

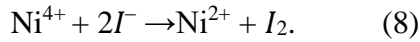
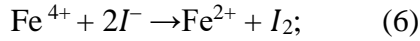
3.6 X-ray photoelectron spectroscopy

X-ray photoelectron spectroscopy (XPS) experiments were performed using PHI 500 VersaProbe II spectrometer with spherical mirror analyzer. Al K_{α} monochromatic X-ray source with 1486.6 eV X-ray energy was utilized. Survey and high-resolution spectra with pass energy of 117.4 eV and 46.95 eV were recorded with 1.0 eV and 0.1 step size, respectively. High-resolution XPS spectra were processed to obtain atomic concentrations, following a common procedure for spectra quantifications. Photoelectron background was subtracted from the high-resolution spectra using Shirley function approximation. All spectra were calibrated to the same adventitious carbon C 1s binding energy position of 284.8 eV.

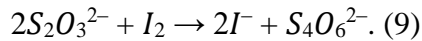
3.7 Oxygen content analysis

The oxygen content was measured using iodometric titration. 15–20 mg of perovskite were added to a flask containing 25 mL of 2M KI solution under Ar atmosphere and allowed to disperse for 3 min. Then 3 mL of 1M HCl were added to dissolve the perovskite. This solution was then titrated to a faint golden color with a 23.28 mM solution of Na₂S₂O₃, which has been pre-standardized with the titration using 0.0222 M solution of K₂Cr₂O₇. After that, starch was added as an indicator and the solution was titrated until the color of the solution changed from transparent blue to almost colorless.

The sample LCFN5_m dissolves in HCl and reacts with KI as follows:



The liberated iodine (I_2) is determined by titration with a standard Na₂S₂O₃ sodium thiosulfate solution:



3.8 Catalyst ink deposition

Oxide powders were deposited onto glassy carbon (GC) disk electrodes as thin films. GC electrodes were polished with 0.05 μm Al₂O₃ slurry on a polishing cloth,

rinsed with distilled water several times, and then dried under an air stream. In order to prepare catalysts inks, powders (perovskite + carbon) with minimum loading 60 mg were mixed for 5 min in a stainless steel vial (SPEX 303, 2.5 mL) with ca. 200 μL of isopropanol in SPEX mill 6000 to obtain a homogeneous paste. Then the paste was dried at 75 $^{\circ}\text{C}$ for 30 min. Then the appropriate amounts of perovskite powder and Vulcan carbon XC72R (VC) (at least 2.5 mg in total), were added to a water/isopropanol solution (4:1 by volume), which contained 0.06 wt.% of Na-substituted Nafion (Sigma Aldrich, 117 solution) to reach ca. 1 $\text{g}_{\text{Nafion}} \text{g}^{-1}_{\text{catalyst}}$. The resulting mixture was sonicated for 30 min to obtain a homogeneous ink. To deposit uniform catalyst layers, three portions ($\sim 3.9 \mu\text{L}$ each for a 3 mm diameter electrode) were subsequently drop-cast onto the GC disk electrode using a micropipette with intermediate drying under a weak N_2 gas stream. The total catalyst (perovskite + carbon) loadings ranged from 12.7 to 59.5 $\mu\text{g cm}^{-2}$ and the VC-to-perovskite ratios were 0/100, 30/70, 50/50 and 70/30.

3.9 Electrochemical measurements

Electrochemical measurements were performed using a Metrohm Autolab PGSTAT302N bipotentiostat equipped with a linear scan generator module. The working electrode was a Metrohm rotating GC disk electrode (RDE) with a 3 mm diameter. Rotating ring-disk electrode (RRDE) measurements were carried out with an RRDE (5 mm diameter GC disk, 7.5 mm outer diameter and 6.5 mm inner diameter gold ring, Pine Research Inst.). All the electrochemical measurements were performed in a single-compartment three-electrode PTFE cell filled with 1M NaOH at 25 $^{\circ}\text{C}$ with temperature

control by the water-cooled thermostatic bath. The reference electrode was Hg/HgO (1M NaOH, Pine Research Inst.), GC plate or platinum wire were used as counter electrodes. All potentials reported here were recalculated to the reversible hydrogen electrode (RHE) scale via the equation: $E(\text{RHE}) = E(\text{Hg/HgO in 1M NaOH}) + 0.930 \text{ V}$. 1M NaOH solution was prepared from 50 wt.% NaOH aqueous solution (Sigma-Aldrich).

In order to record the electrochemical data for the LCFN5_m S sample, the GC electrode with already prepared catalyst film of LCFN5_m was stored in 1M NaOH in the PTFE cell and then used for the electrochemical measurements without rinsing with water.

In order to evaluate the electrochemically active surface area (ECSA) before and after soaking in 1M NaOH, the Ni cathodic peak areas for LCFN_m and LCFN_m_S samples during OER were used (see Appendix).

In order to evaluate the catalyst's performance in the electrolyte after the addition of Fe ions (Fe_{aq}), aqueous solution of $\text{Fe}(\text{NO}_3)_3 \cdot 9\text{H}_2\text{O}$ was added to the 50 wt.% NaOH solution (Sigma-Aldrich) to reach Fe_{aq} concentration of 1 ppm in the 1M NaOH electrolyte.

For the OER kinetic measurements, cyclic voltammograms (CVs) at 10 mV s^{-1} were recorded in N_2/Ar -saturated 1M NaOH solution at a 1600 rpm rotation rate. The uncompensated ohmic resistance values (10-20 Ω) were determined from the high-frequency intercept of electrochemical impedance hodographs of RDE electrode recorded at OER potentials in the 0.1 - 100 kHz frequency range (5 mV amplitude). All the reported RDE voltammograms were IR-corrected, if not stated otherwise.

3.9.1 Reference electrode calibration

Electrochemical deposition of spongy black Pt on a Pt rotating disk electrode (Pt-RDE) was carried out in a two electrode cell with Pt mesh as a counter electrode. First, Pt-RDE was polarized galvanostatically in 0.1M HCl for 10 min at 2.94 mA (anodic polarization). Then, the electrode was polarized in 0.05M H₂SO₄ for 10 min at -2.94 mA (cathodic polarization). Further, H₂PtCl₆ solution was added to the cell, and Pt black was deposited at -0.588 mA for 4000 sec on the Pt-RDE. After deposition, the platinized Pt-RDE was polarized in 0.05M H₂SO₄ at -2.94 mA for 10 min. The solution was further saturated with hydrogen and the potential difference was measured between the prepared reversible hydrogen electrode and 1 M NaOH Hg/HgO electrode. The open circuit potential of the Pt-RDE stabilized at -0.92956 V ~ -0.930 V vs Hg/HgO electrode.

3.9.2 Rotating ring disk electrode calibration

For the RRDE calibration, Pt/C HiSPEC 4000 (24.5 $\mu\text{g cm}^{-2}$ Pt loading) catalyst was deposited on the RRDE disk. Firstly, the Au ring electrode was cleaned by cycling the ring potential within the range -0.90 – 0.60 V vs Hg/HgO (0.03 - 1.53 V vs RHE) at 200 mV s⁻¹ in 1M NaOH electrolyte. After that, the cell was filled with 1M NaOH + 10 mM K₃[Fe(CN)₆] solution. CVs were registered at 10 mV/s within the range 0.05-0.62 V at 400, 900, 1600, and 2500 rpm. The Au ring potential was set to +0.55 V vs Hg/HgO (1.48 V vs RHE), Figure 13a. The RRDE collection efficiency N (~25% at 900 rpm) was determined from the ring (I_{ring}) and disk current (I_{disk}) ratios, Figure 13b.

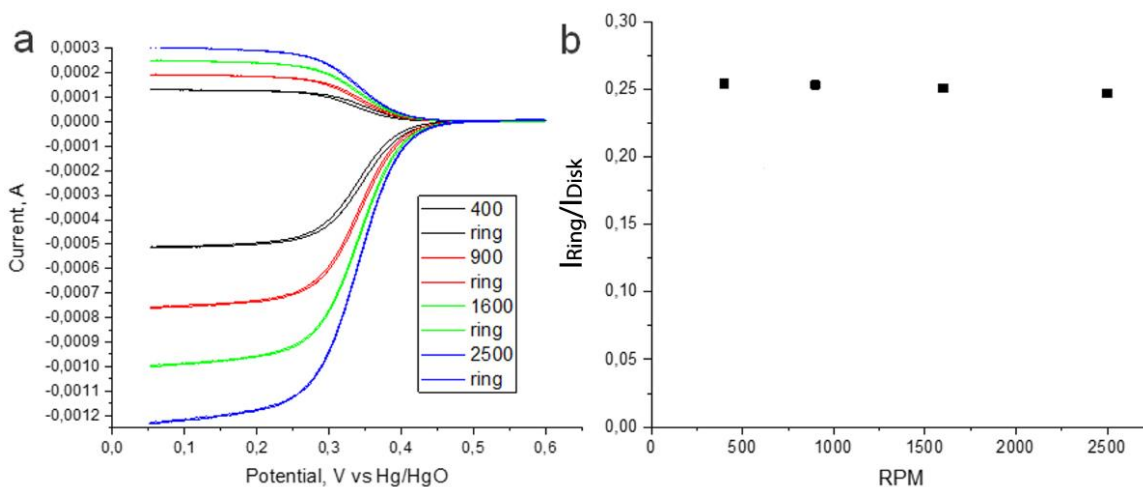


Figure 13. (a) CVs of disk (Pt/C HiSPEC) and ring (Au) electrodes at 10 mV s^{-1} at different electrode rotation rates in N_2 -saturated $1 \text{ M NaOH} + 10 \text{ mM K}_3[\text{Fe}(\text{CN})_6]$ solution. (b) The ratio of ring current to disk current at the disk potential 0.05 V vs Hg/HgO .

3.10 Inductively coupled plasma mass spectroscopy/atomic emission spectroscopy

For the inductively coupled plasma mass spectroscopy/atomic emission spectroscopy (ICP-MS/AES) experiments, the 1 M NaOH solution was collected after the electrochemical measurements of LCFN5_m catalyst film on GC electrode (total mass loading $51 \mu\text{g cm}^{-2}$; without VC). The potential was cycled between $0.93 - 1.65 \text{ V vs RHE}$ at a scan rate 10 mV s^{-1} (30 cycles). Aliquots of the solution were taken for ICP-MS analysis (Agilent Technologies). Additionally, the LCFN5_m sample was soaked for 4 days in 1 M NaOH solution ($\sim 13 \text{ mg}$ in 10 mL), and the resulting solution was analyzed by ICP-AES (Perkin Elmer Optima 5300) to determine the concentration of the leached lanthanum.

Aliquots of the solution were taken for ICP-AES analysis from 50 wt.% Sigma-Aldrich NaOH aqueous solution to determine the concentration of Fe in the reagent used for the electrolyte preparation.

3.11 DFT details

All density functional theory (DFT) calculations were performed in the VASP program by Prof. Dmitry Aksyonov [140] using the SIMAN package for high-throughput calculations [141]. The generalized gradient approximation (GGA) to exchange-correlation functional with spin polarization and standard PAW PBE potentials [142] with minimum number of valence electrons were employed. To take into account the strongly correlated character of *d*-electrons, a Hubbard-like correction is added within the Dudarev scheme [143]. The *U* values of 4.0 eV and 6.2 eV were used for Fe and Ni, based on works ref. [144] and [145] respectively. These *U* values reproduce electronic structure in good agreement with previous theoretical methods and experiment. In particular, the chosen *U* value for Fe reproduces experimental band gap and local magnetic moment of Fe in LaFeO₃. The chosen *U* value for Ni is very close to the self-consistent *U* value of 5.8 eV in LaNiO₃. The slightly larger value used in our study is due to reasons of compatibility with our previous calculations. Overall, the *U*=6.2 eV is used for Ni-based oxides in Materials Project, which we also adopt in most of our calculations. The energy cut-off was fixed at 400 eV. The 40-atom pseudocubic supercell and gamma-centered k-point 6x6x6 were used. Gaussian smearing with a smearing width of 0.1 eV was used for Brillouin-zone integrations. The optimization of atomic positions was

performed using a quasi-Newton algorithm until the maximum force permitted for any vector component was less than 0.05 eV \AA^{-1} .

4. Results and discussion

4.1 Optimization of spray pyrolysis synthesis

The $\text{LaFe}_{0.25}\text{Ni}_{0.75}\text{O}_3$ perovskite was used as basic composition from which we started the optimization route for the ultrasonic spray pyrolysis (USP) method. After ultrasonic spray pyrolysis, the powders were collected and annealed at 300, 450, 600, 800, and 1000°C for 10 hours in air. Morphologically the annealed powder mostly consists of solid spherical particles (Figure 14a-c), except for the sample annealed at 1000 °C (Figure 14d), where high-temperature annealing distorted initial spherical morphology by forming numerous links between the particles resulting in high sintering degree. Sample, annealed at 600 °C has similar morphology to those obtained at 300 and 450°C (Figure S1).

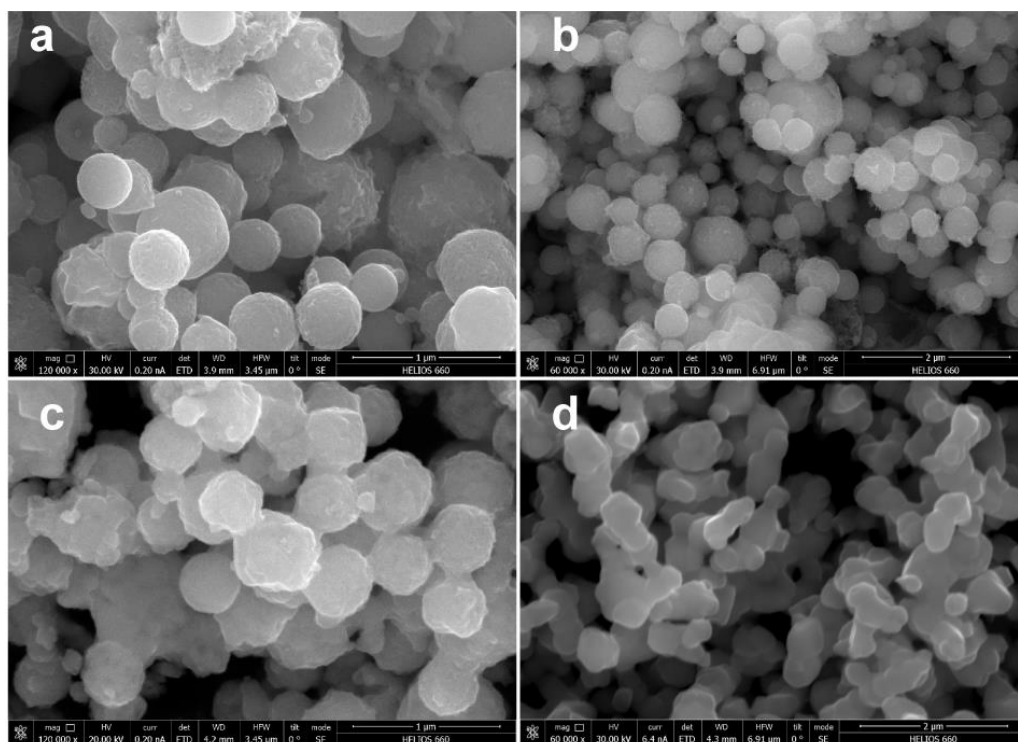


Figure 14. SEM images of spherical particles of $\text{LaFe}_{0.25}\text{Ni}_{0.75}\text{O}_3$ sample annealed at (a) 300, (b) 450, (c) 800, and (d) 1000 °C.

The spheres annealed at 800 °C demonstrate homogeneous elemental distribution. The EDX analysis (Figure 15) gives the average cationic composition of $\text{La}_{0.99}\text{Fe}_{0.24(1)}\text{Ni}_{0.76(1)}$ which corresponds to $\text{LaFe}_{0.25}\text{Ni}_{0.75}\text{O}_3$ phase (Figure 16). All diffraction peaks in PXRD pattern of the sample annealed at 800 °C correspond to the perovskite structure, while for the samples prepared at 600 °C and lower annealing temperatures there are impurity diffraction peaks. Such impurities as La_2O_3 , NiO and small undefined peaks at $\sim 24.5^\circ$ and 28.0° (2θ) are observed (Figure 16, S2). The diffraction peaks at $\sim 29.5^\circ$ (2θ) are also visible in the PXRD pattern of well-crystallized sample annealed at 1000 °C. These peaks originate from traces of Cu K_β radiation.

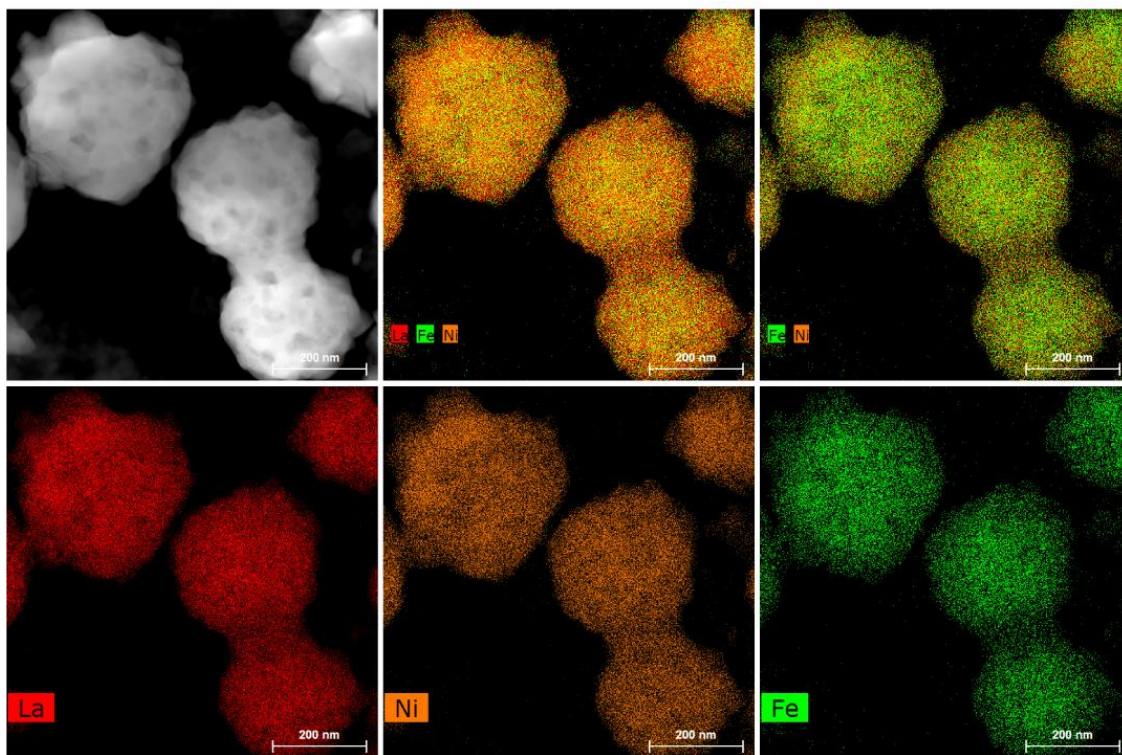


Figure 15. HAADF-STEM image of spherical particles in the $\text{LaFe}_{0.25}\text{Ni}_{0.75}\text{O}_3$ sample annealed at 800 °C, along with the La, Fe, Ni STEM-EDX maps and a mixed color-coded compositional map.

The PXRD pattern of the sample annealed at 800 °C has the rhombohedral $R-3c$ perovskite structure with the unit cell parameters $a = 5.4847(2)$ Å, $c = 13.2164(4)$ Å and unit cell volume $V = 344.30(2)$ Å³, as refined by the Rietveld method. The BET specific surface area amounts to 3.3 m²g⁻¹.

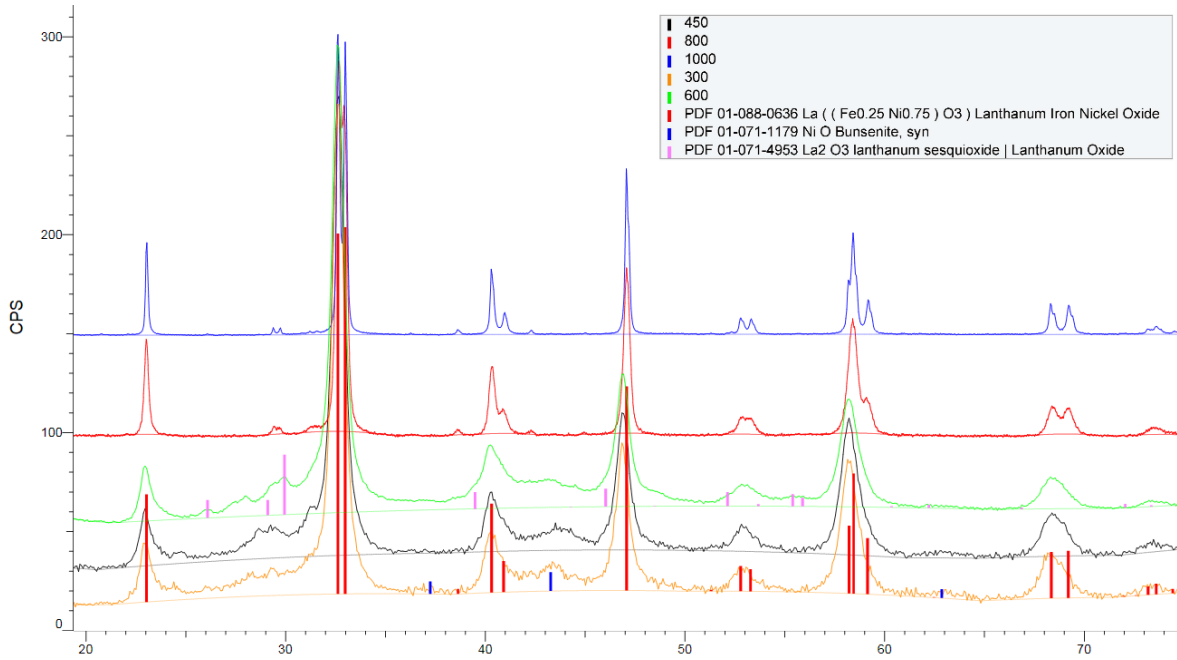


Figure 16. PXRD patterns of the $\text{LaFe}_{0.25}\text{Ni}_{0.75}\text{O}_3$ samples annealed at different temperatures: 300, 450, 600, 800, 1000 °C. The red lines indicate the PDF 01-088-0636 positions for $\text{LaFe}_{0.25}\text{Ni}_{0.75}\text{O}_3$ (Cu $K_{\alpha 1,2}$ radiation, diffractograms are normalized by maximum intensity).

We found that the optimal powder annealing conditions for $\text{LaFe}_{0.25}\text{Ni}_{0.75}\text{O}_3$ is 800 °C for 10 hours, since this allows us to obtain a homogeneous perovskite phase without impurities and preserve spherical morphology. These conditions were applied for the synthesis of the Ca-doped $\text{La}_{1-x}\text{Ca}_x\text{Fe}_{0.25}\text{Ni}_{0.75}\text{O}_3$ ($x = 0.1, 0.2$) samples. However, the formation of secondary phases such as CaO, NiO and the Ruddlesden-Popper phase was

encountered, which was also previously observed for similar systems, see Section 2.4.1. It is worth noting that additional annealing at 1000 °C for 8 hours in oxygen flow of 20 ml L⁻¹ did not allow obtaining the pure perovskite phase (Figure S3). In order to study the electrocatalytic properties of perovskite without the contribution of impurity phases, we tried to change the Ni:Fe ratio and synthesized the following compositions: La_{1-x}Ca_xFe_{0.7}Ni_{0.3}O₃ (x=0, 0.3, 0.5). The system La_{1-x}Ca_xFe_{0.25}Ni_{0.75}O₃ (x= 0, 0.1, 0.2) will not be considered further.

The results presented further in sections 4.2-4.5 are based on the following publication: Porokhin, S. V., Nikitina, V. A., Aksyonov, D. A., Filimonov, D. S., Pazhetnov, E. M., Mikheev, I. V., & Abakumov, A. M. Mixed-Cation Perovskite La_{0.6}Ca_{0.4}Fe_{0.7}Ni_{0.3}O_{2.9} as a Stable and Efficient Catalyst for the Oxygen Evolution Reaction. ACS Catalysis 11.13 (2021): 8338-8348.

4.2 Synthesis of La_{1-x}Ca_xFe_{0.7}Ni_{0.3}O_{3-δ} (x = 0, 0.3, 0.5) samples

The PXRD patterns of the as-prepared LFN, LCFN3, LCFN5 and LCFN5_m (modified USP method) samples are shown in Figure 17. Major diffraction peaks correspond to the perovskite crystal structure. The undoped LFN sample is single-phase and adopts an orthorhombically distorted perovskite structure with the *Pbnm* space group and unit cell parameters $a = 5.5482(2) \text{ \AA}$, $b = 5.5285(2) \text{ \AA}$, $c = 7.7813(4) \text{ \AA}$, $V = 238.68(2) \text{ \AA}^3$, as revealed with the Rietveld refinement. The unit cell parameters of the perovskite phases in all the synthesized samples are listed in Table 4.

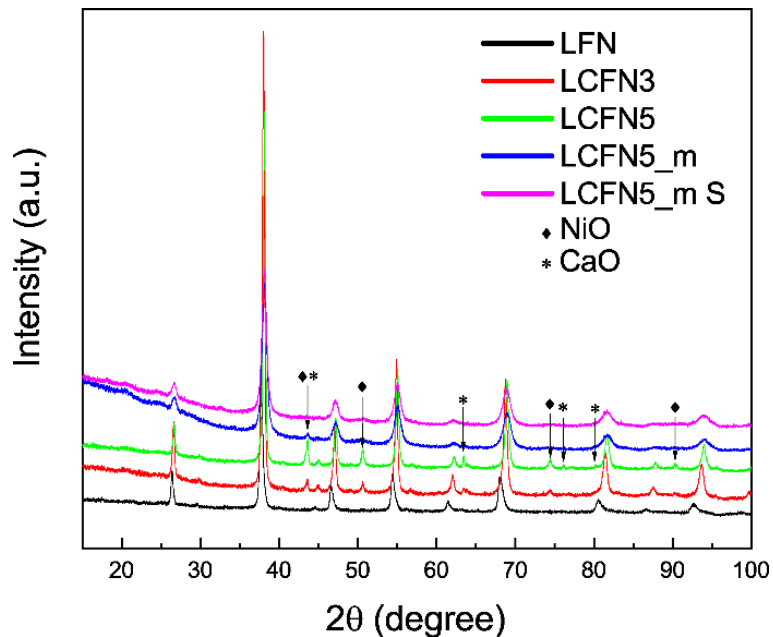


Figure 17. PXRD patterns of the $\text{La}_{1-x}\text{Ca}_x\text{Fe}_{0.7}\text{Ni}_{0.3}\text{O}_{3-\delta}$ ($x = 0, 0.3, 0.5$) samples (Co $K_{\alpha 1}$ radiation).

Table 4. Unit cell parameters of the perovskite phases in the synthesized samples.

Sample	$a, \text{\AA}$	$b, \text{\AA}$	$c, \text{\AA}$	$V, \text{\AA}^3$	S.G.
LFN	5.5482(2)	5.5285(2)	7.7813(4)	238.68(2)	<i>Pbnm</i>
LCFN3	5.4922(3)		13.4229(5)	350.65(3)	<i>R-3c</i>
LCFN5	5.4751(1)		13.4013(5)	347.91(1)	<i>R-3c</i>
LCFN5_m*	5.4798(8)		13.337(4)	346.8(1)	<i>R-3c</i>
LCFN5_m S**	5.4833(8)		13.337(4)	347.28(9)	<i>R-3c</i>

*m - modified USP synthesis **S - soaked 4 weeks in 1M NaOH solution to check stability

Increasing the Ca content results in a growing amount of CaO and NiO impurities in the LCFN3 and LCFN5 samples (Figures 18, 19) that is probably related to difficulties in stabilizing Ni^{3+} at the relatively high spray pyrolysis temperature of 1100 °C (collected powders were annealed at 800 °C for 10 hours) used for these samples. Employing a modified USP technique with sorbitol as fuel and ozone as oxidizer reduces the pyrolysis

temperature to 850 °C (collected powders were annealed at 600 °C for 5 hours) and allows obtaining the LCFN5_m sample with only traces of CaO (4.4(5) wt.% from the Rietveld refinement, while with the basic USP method the amount of impurities is higher: CaO - 7.3 wt.%, and NiO - 5.6 wt.%, (see further Table 5).

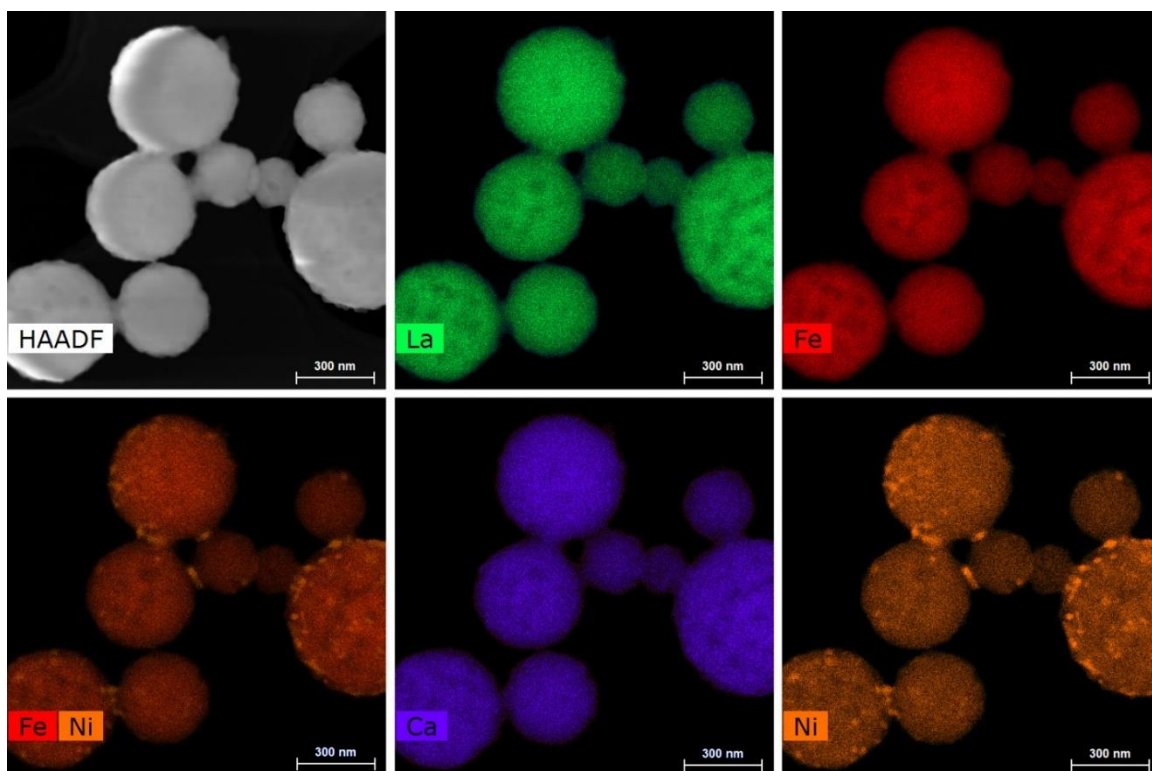


Figure 18. HAADF-STEM image of spherical particles in the LCFN3 sample along with the La, Ca, Fe, Ni STEM-EDX maps and a mixed color-coded compositional map.

The PXRD pattern of the LCFN5_m sample was indexed with the rhombohedral $R-3c$ perovskite structure with the unit cell parameters $a = 5.4797(9) \text{ \AA}$, $c = 13.338(4) \text{ \AA}$, $V = 346.8(1) \text{ \AA}^3$ (Table 4). The perovskite subcell volume decreases from 59.67 \AA^3 in the LFN sample to 57.80 \AA^3 in the LCFN5_m sample, in agreement with the difference in ionic radii between La^{3+} ($r = 1.36 \text{ \AA}$, CN = 12) and Ca^{2+} ($r = 1.34 \text{ \AA}$, CN = 12) [146].

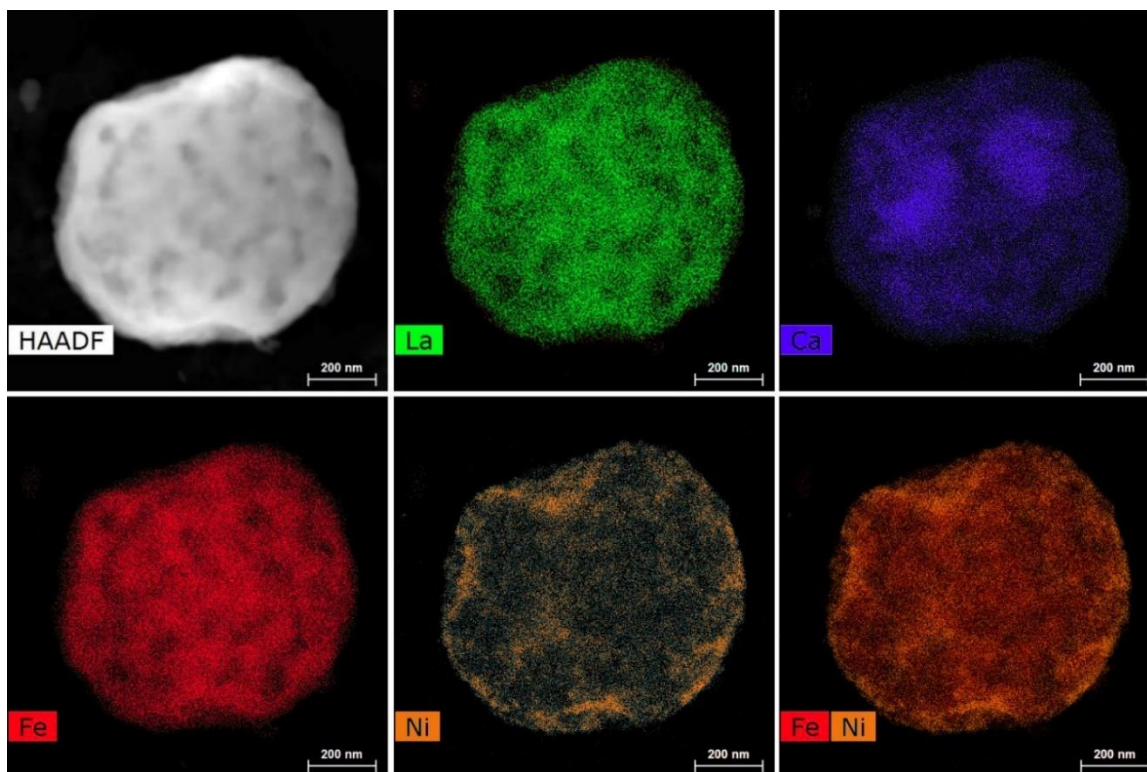


Figure 19. HAADF-STEM image of spherical particles in the LCFN5 sample along with the La, Ca, Fe, Ni STEM-EDX maps and a mixed color-coded compositional map.

Morphologically the Ca-doped samples LCFN5 and LCFN3 obtained by conventional USP technique (Figure 18,19) without sorbitol/ozone and with high-temperature annealing consist of solid spherical agglomerates. Clear exsolution of NiO is also observed, in agreement with the PXRD data. In contrast the LCFN5_m sample consists of porous hollow spherical particles with the diameters ranging between 200 and 1200 nm (Figure 20). The particle wall thickness is ca. 25 nm and the pore diameter varies from 1.5 to 140 nm. The morphology of the LCFN5_m sample demonstrates clear advantages compared to LCFN5 and LCFN3 obtained by conventional USP technique.

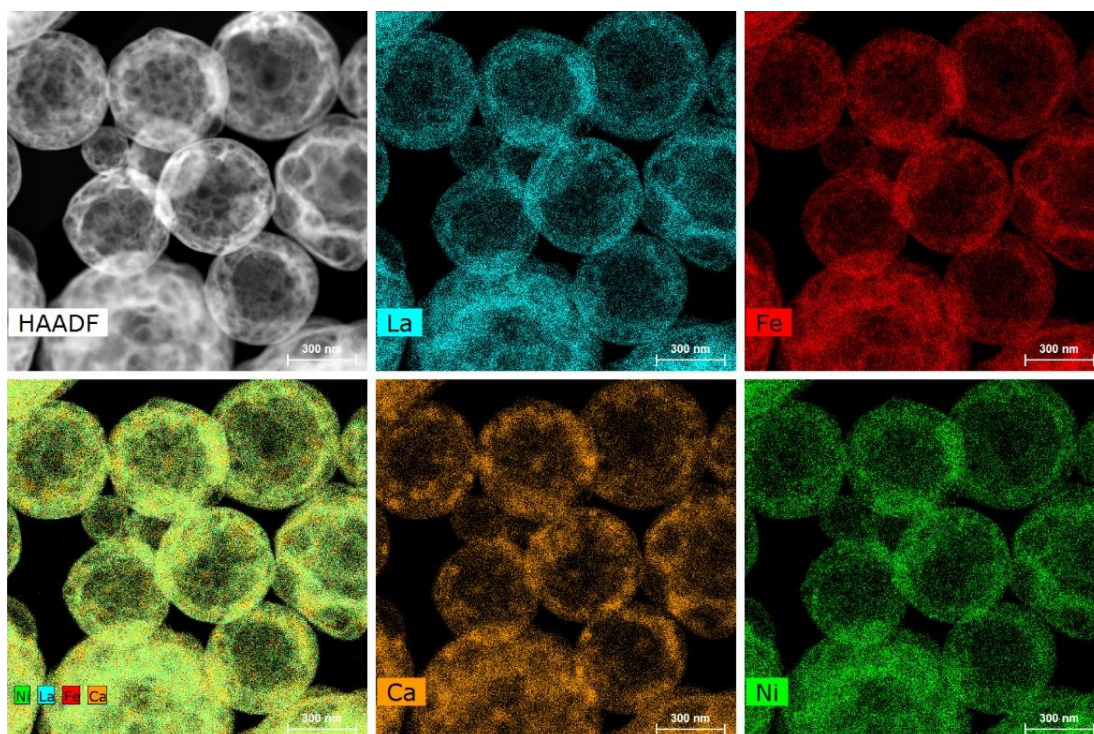


Figure 20. HAADF-STEM image of spherical hollow particles in the LCFN5_m sample along with the La, Ca, Fe, Ni STEM-EDX maps and a mixed color-coded compositional map.

The spheres demonstrate mostly homogeneous cation distribution, although crystallites with apparent Ca excess were also observed (Figure 20). The EDX analysis with the spectra integrated over the entire spherical particles revealed the average cationic composition of $\text{La}_{0.50(1)}\text{Ca}_{0.49(1)}\text{Fe}_{0.70(1)}\text{Ni}_{0.31(1)}$, in agreement with the molar ratio of nitrates used for the synthesis. However, the EDX spectra integrated over certain areas, which do not demonstrate Ca excess (presumably corresponding to the perovskite phase without CaO impurity) reveal the $\text{La}_{0.53(2)}\text{Ca}_{0.45(2)}\text{Fe}_{0.70(1)}\text{Ni}_{0.32(1)}$ composition which corroborates La excess and Ca deficiency observed in the Rietveld refinement (see occupancy factors in Table 7). The LCFN5_m spheres are the agglomerates of primary crystalline perovskite-structured nanoparticles (Figure 21).

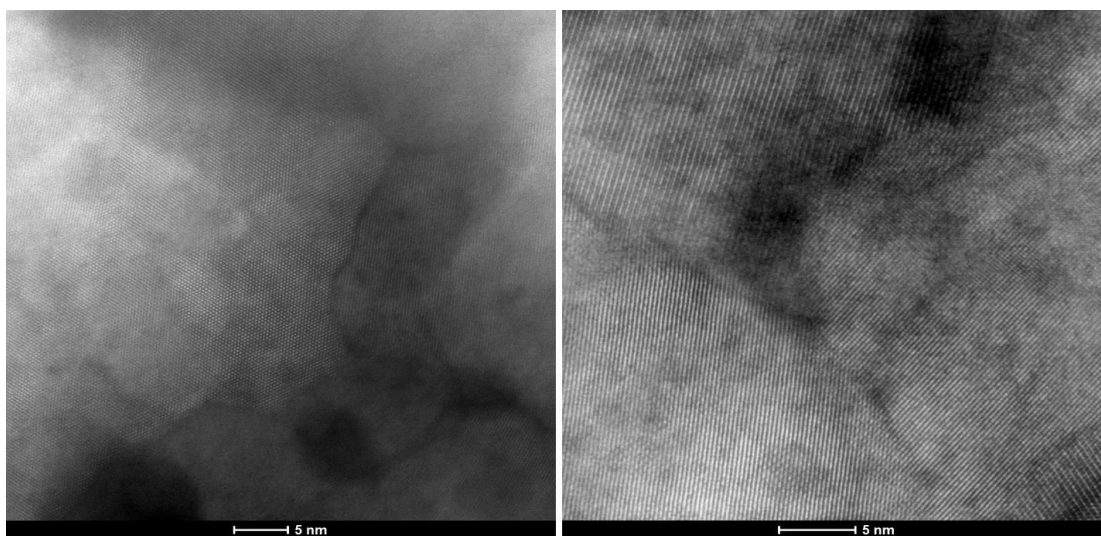


Figure 21. HAADF-STEM images of perovskite nanoparticles constituting spherical hollow agglomerates in the LCFN5_m sample.

The striking difference in morphology is also reflected in BET specific surface area, which is explained by the extensive gas evolution during the USP process due to intense sorbitol burning in the highly oxidizing atmosphere. For the LCFN5_m sample it is 5-7 times higher ($15.1\text{m}^2\text{g}^{-1}$) than for the samples prepared with the conventional USP technique (3.4 , 2.2 and $2.3\text{m}^2\text{g}^{-1}$ for the LFN, LCFN3 and LCFN5 samples, respectively). The phase compositions and surface areas are listed in Table 5.

Table 5. List of samples, their composition, preparation conditions and BET surface area.

Sample	Phase composition, wt. %	Surface area, m^2g^{-1}
LFN	100% - * $\text{LaFe}_{0.7}\text{Ni}_{0.3}\text{O}_3$	3.4
LCFN3	92.3% - * $\text{La}_{0.7}\text{Ca}_{0.3}\text{Fe}_{0.7}\text{Ni}_{0.3}\text{O}_{3-\delta}$ 4.5% - CaO 3.2% - NiO	2.2
LCFN5	87.1% - * $\text{La}_{0.5}\text{Ca}_{0.5}\text{Fe}_{0.7}\text{Ni}_{0.3}\text{O}_{3-\delta}$ 7.3% - CaO 5.6% - NiO	2.3
LCFN5_m	95.6% - $\text{La}_{0.6}\text{Ca}_{0.4}\text{Fe}_{0.7}\text{Ni}_{0.3}\text{O}_{2.9}$ 4.4% - CaO	15.1
LCFN5_m S	100% - $\text{La}_{0.6}\text{Ca}_{0.4}\text{Fe}_{0.7}\text{Ni}_{0.3}\text{O}_{2.9}$	17.1

* nominal composition, phase fraction determined by semi-quantitative PXRD method

Additionally, the LCFN5_m sample was soaked for 4 weeks in 1M NaOH solution to check the stability without polarization (denoted as LCFN5_m S). The PXRD pattern of LCFN5_m S does not reveal noticeable changes in the reflections of the perovskite phase (Figure 17), and the change in the unit cell volume amounts to 0.14% only (Table 4). The Rietveld refinement of the perovskite structure in the LCFN5_m S sample does not demonstrate noticeable changes exceeding two standard deviations (Tables 6-8) indicating high stability of the bulk $\text{La}_{0.6}\text{Ca}_{0.4}\text{Fe}_{0.7}\text{Ni}_{0.3}\text{O}_{2.9}$ structure towards alkaline solution. As a positive effect of soaking, one can also notice dissolution of the CaO impurity, as reflected by the disappearance of the admixture reflections in the PXRD patterns of the soaked sample (Figure 17).

The crystal structure of the perovskite phase in the LCFN5_m and LCFN5_m S samples were refined from PXRD data with the Rietveld method. The occupancy of the A perovskite site (the $6a$ position) with La and Ca was refined whereas the Fe and Ni contents at the B site (the $6b$ position) were fixed to their nominal values because low difference in their atomic numbers impedes the refinement of the occupancy factors. The partial occupancy of the oxygen position was fixed according to the non-stoichiometry index of $\delta = 0.1$ determined from combined iodometric titration and ^{57}Fe Mössbauer spectroscopy results (see further Figure 24). All atomic positions were refined with the common atomic displacement parameter. The refinement resulted in the $\text{La}_{0.6}\text{Ca}_{0.4}\text{Fe}_{0.7}\text{Ni}_{0.3}\text{O}_{2.9}$ chemical composition, in agreement with the CaO impurity in this

sample and with the results of EDX analysis (Figure 20). The crystallographic parameters for the $\text{La}_{0.6}\text{Ca}_{0.4}\text{Fe}_{0.7}\text{Ni}_{0.3}\text{O}_{2.9}$ structure are listed in Tables 6-8.

Table 6. Crystallographic information from Rietveld refinement for the pristine (LCFN5_m) and soaked 4 weeks (LCFN5_m_S) $\text{La}_{0.6}\text{Ca}_{0.4}\text{Fe}_{0.7}\text{Ni}_{0.3}\text{O}_{2.9}$ perovskite.

	LCFN5_m	LCFN5_m S
Space group	<i>R-3c</i>	<i>R-3c</i>
<i>a</i> , Å	5.4798(8)	5.4833(8)
<i>c</i> , Å	13.337(4)	13.337(4)
<i>V</i> , Å ³	346.8(1)	347.28(9)
<i>Z</i>	6	6
ρ , g cm ⁻³	5.76	5.89
Radiation	Co K $_{\alpha 1}$, $\lambda = 1.78892\text{\AA}$	Co K $_{\alpha 1}$, $\lambda = 1.78892\text{\AA}$
2 θ range, deg.	20 - 100	20 - 100
R _F , R _p , R _{wP}	0.021, 0.017, 0.022	0.023, 0.017, 0.021

Table 7. Fractional atomic coordinates for the pristine (LCFN5_m, first row) and soaked 4 weeks (LCFN5_m_S, second row) $\text{La}_{0.6}\text{Ca}_{0.4}\text{Fe}_{0.7}\text{Ni}_{0.3}\text{O}_{2.9}$ perovskite.

Atom	Position	Occupancy	x/a	y/b	z/c	$U_{\text{iso}}, \text{\AA}^2$
LaCa1	$6a$	0.581(9)La	0	0	1/4	0.0113(8)
		0.419(9)Ca				
FeNi1	$6b$	0.630(8)La	0	0	1/4	0.0054(7)
		0.370(8)Ca				
O1	$18e$	0.7Fe	0	0	0	0.0113(8)
		0.3Ni				
O1	$18e$	0.7Fe	0	0	0	0.0054(7)
		0.3Ni				
O1	$18e$	0.9667O	0.445(2)	0	1/4	0.0113(8)
			0.451(2)	0	1/4	0.0054(7)

Table 8. Main interatomic distances (\AA) for the pristine (LCFN5_m) and soaked 4 weeks (LCFN5_m S) $\text{La}_{0.6}\text{Ca}_{0.4}\text{Fe}_{0.7}\text{Ni}_{0.3}\text{O}_{2.9}$ perovskite.

	LCFN5_m	LCFN5_m S	
LaCa1 – O1	2.437(7) \times 3	LaCa1 – O1	2.470(7) \times 3
LaCa1 – O1	2.745(7) \times 6	LaCa1 – O1	2.742(7) \times 6
FeNi1 – O1	1.957(9) \times 6	FeNi1 – O1	1.953(9) \times 6

The experimental, calculated and difference PXRD patterns are shown in Figure 22.

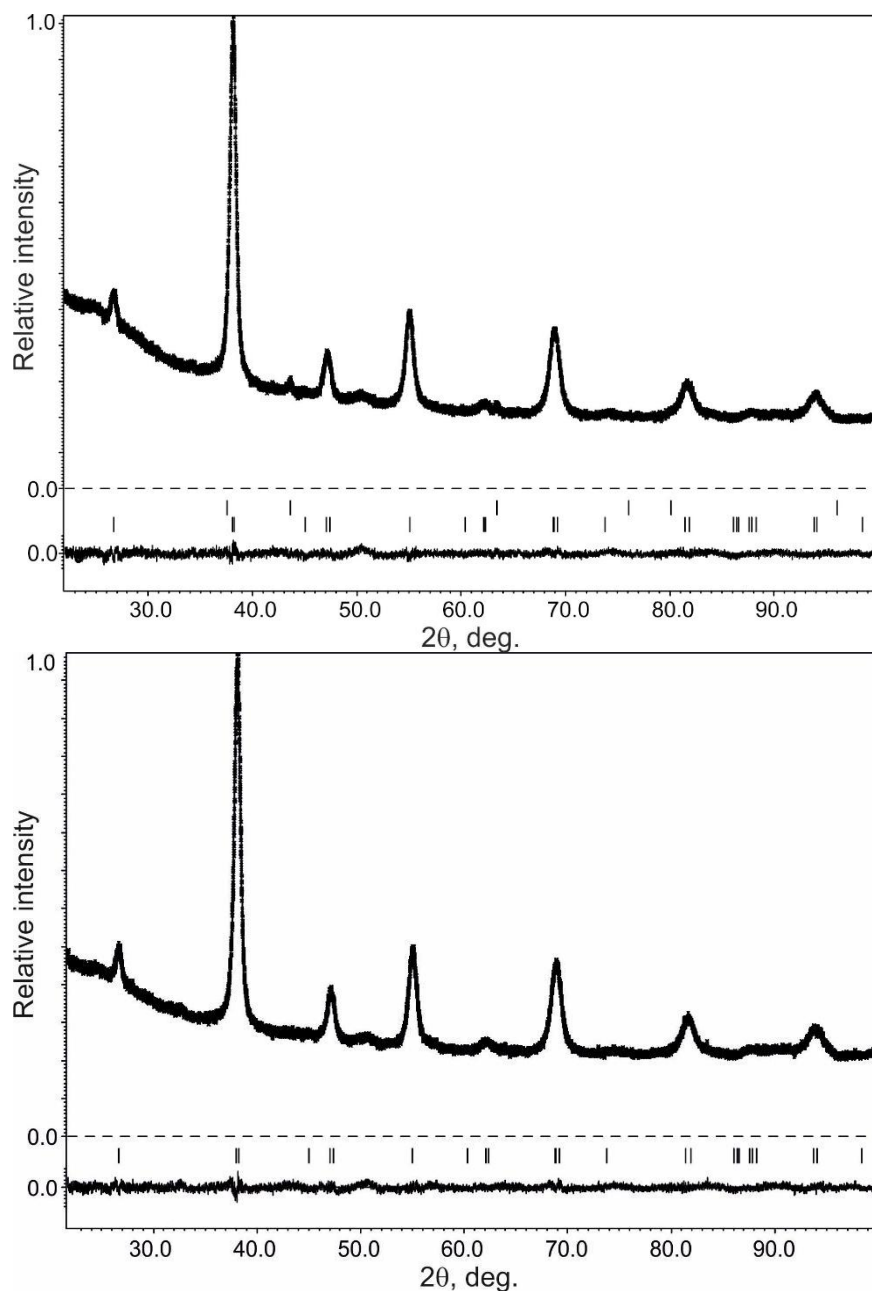


Figure 22. Experimental, calculated and difference PXRD profiles after Rietveld refinement of the (top) $\text{La}_{0.6}\text{Ca}_{0.4}\text{Fe}_{0.7}\text{Ni}_{0.3}\text{O}_{2.9}$ perovskite LCFN5_m after synthesis with the CaO admixture 4.4(5) wt. % and (bottom) LCFN5_m S sample (soaked 4 weeks). The ticks indicate the Bragg reflection positions.

Since the LCFN5_m sample showed the most homogeneous element distribution and high BET surface area among all doped samples, we focused on the detailed characterization of this sample using TEM and ^{57}Fe Mössbauer spectroscopy, for further interpretation of the OER electrocatalytic properties.

4.2.1 Characterization of $\text{La}_{0.6}\text{Ca}_{0.4}\text{Fe}_{0.7}\text{Ni}_{0.3}\text{O}_{2.9}$

The crystal structure of $\text{La}_{0.6}\text{Ca}_{0.4}\text{Fe}_{0.7}\text{Ni}_{0.3}\text{O}_{2.9}$ has been confirmed with transmission electron microscopy. The brightest spots in the ED patterns can be indexed with a pseudocubic perovskite subcell with $a \approx 3.9 \text{ \AA}$ (Figure 23a). Weak superlattice reflections corresponding to the $\mathbf{k} = [\frac{1}{2}, \frac{1}{2}, \frac{1}{2}]$ propagation vector are visible in the [110] ED pattern. These reflections indicate the $a^-a^-a^-$ octahedral tilting distortion and corroborate symmetry reduction from $Pm-3m$ to $R-3c$ [147], in agreement with the PXRD data. HAADF-STEM and ABF-STEM images (Figure 23b-e) provide direct visualization of a well-ordered perovskite structure. In the HAADF-STEM images (Figure 23b,d) the brightest dots stand for the columns of the A cations ($A = \text{La}_{0.6}\text{Ca}_{0.4}$), whereas less bright dots indicate the B-cation columns ($B = \text{Fe}_{0.7}\text{Ni}_{0.3}$). The oxygen atoms do not show up in these images due to their low atomic number, but become visible as faint grey dots in the ABF-STEM images (Figure 23c,e), because of less steep dependence of the contrast on the atomic number. Neither segregated nor ordered oxygen vacancies are observed.

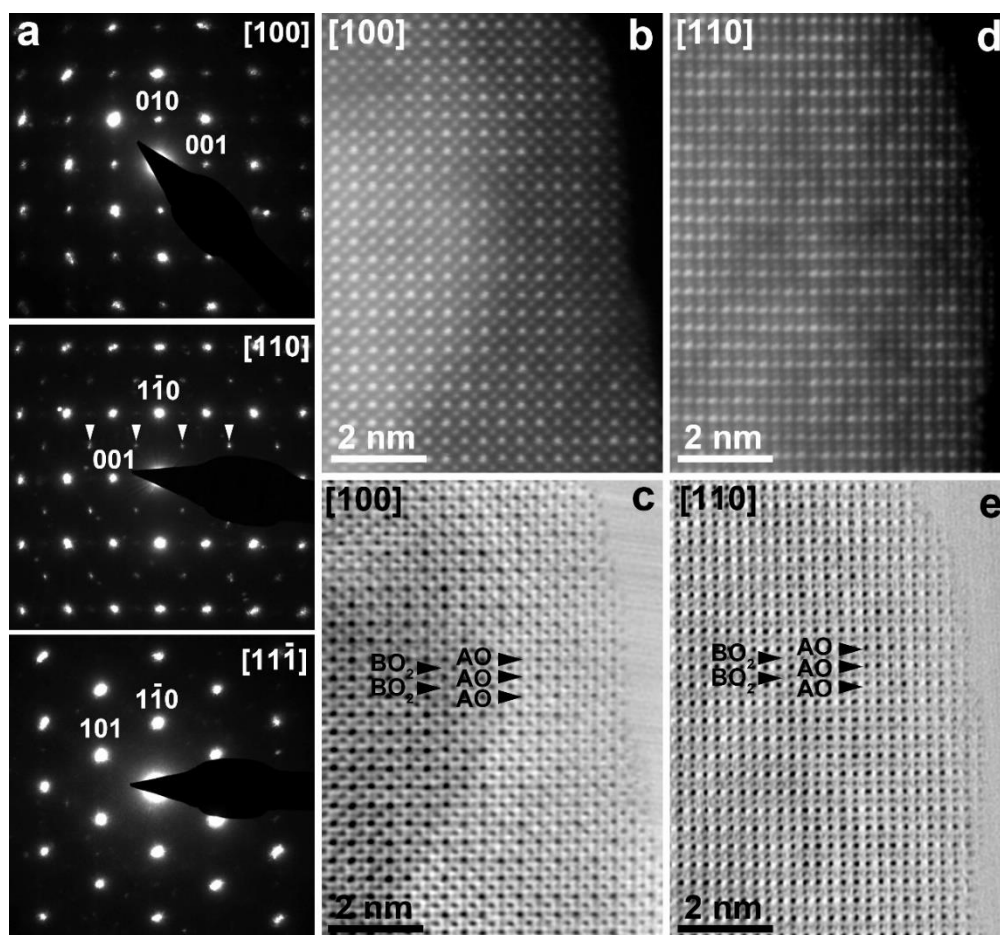


Figure 23. (a) Electron diffraction patterns of LCFN5_m. The perovskite subcell reflections are indexed, the superlattice reflections of the $\mathbf{k} = [\frac{1}{2}, \frac{1}{2}, \frac{1}{2}]$ propagation vector due to the $\bar{a}\bar{a}\bar{a}$ octahedral tilting distortion are marked with arrowheads. (b, c) [100] and (d, e) [110] (b, d) HAADF-STEM and (c, e) ABF-STEM images of the atomic structure of LCFN5_m. The perovskite AO (A = La_{0.6}Ca_{0.4}) and BO₂ (B = Fe_{0.7}Ni_{0.3}) layers are marked.

The nickel oxidation state in the LCFN5_m sample was estimated as +3.4 by iodometric titration taking into account the Fe oxidation state of +3.1 as determined by ⁵⁷Fe Mössbauer spectroscopy (Figure 24left, Table 9; due to significantly simpler spectrum, the Fe⁴⁺ fraction determined at 298 K was used for calculations) that provides the oxygen non-stoichiometry index $\delta = 0.1$, resulting in the La_{0.6}Ca_{0.4}Fe_{0.7}Ni_{0.3}O_{2.9} formula.

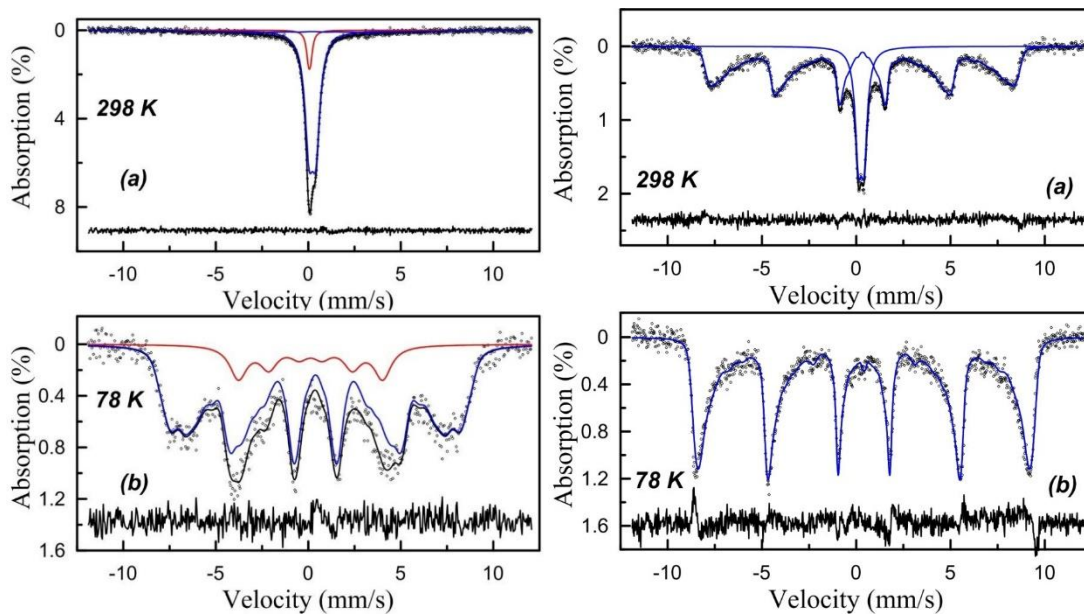


Figure 24. ^{57}Fe Mössbauer spectra at (a) $T = 298$ and (b) 78 K. (left) LCFN5_m sample and (right) LFN sample modeled with a description of the magnetically split components using hyperfine field (HF) distributions.

The refined ^{57}Fe Mössbauer hyperfine parameters for Ca-doped and pristine LFN sample are listed in Table 9. At room temperature, the spectrum of LCFN5_m is paramagnetic. The main component is doublet d11 with isomer shift $\delta = 0.27 \text{ mm s}^{-1}$ which is consistent with Fe^{3+} in Ni-substituted $\text{LaFe}_{1-x}\text{Ni}_x\text{O}_{3-\delta}$ solid solutions at high x [148]. The minor component d21 with $\delta = 0.11 \text{ mm s}^{-1}$ is consistent with Fe^{4+} ($\sim 10\%$). Another component di31 ($\sim 10\%$) corresponds to strongly broadened magnetic Fe^{3+} in perovskite cation-mixed phase.

Table 9. ^{57}Fe Mössbauer hyperfine parameters for the LCFN5_m and LFN samples.

LCFN5_m						
Component	δ (mm s $^{-1}$)	ΔEQ (mm s $^{-1}$)	H (T)	A (%)	Γ (mm s $^{-1}$)	Comments
298K						
d11	0.27	0.36	-	79	0.53	Fe $^{3+}$
di31	0.26	0.00	<10-45>	12	-	Fe $^{3+}$
d21	0.11	0.11	-	9	0.28	Fe $^{4+}$
78K						
di12	0.46	0.00	<5-55>	85	-	Fe $^{3+}$
s12	0.19	0.00	24.2	15	1.13	Fe $^{4+}$
LFN						
Component	δ (mm s $^{-1}$)	ΔEQ (mm s $^{-1}$)	H (T)	A (%)	Γ (mm s $^{-1}$)	Comments
298K						
di11	0.38	-0.06	<7-55>	77	-	Fe $^{3+}$
d11	0.31	0.29	-	23	0.41	superparamag .
78K						
di12	0.46	-0.06	<0-60>	100	-	Fe $^{3+}$

δ (mm s $^{-1}$) - isomer shift
 ΔEQ (mm s $^{-1}$) - quadrupole splitting
H (T) - hyperfine magnetic field
A (%) - relative area
 Γ (mm s $^{-1}$) - linewidth

For the LFN sample, the oxidation state of iron is +3 (Figure 24, Table 9). At room temperature the major components of the spectrum consist of a strongly broadened component of the di11 magnetic sextet which corresponds to Fe $^{3+}$ (~ 77%) and the d11 doublet, which also corresponds to Fe $^{3+}$. Thus, Ca doping provokes major increase in the Ni oxidation state whereas the Fe oxidation state is less significantly affected.

4.3 Electrochemical performance in the OER

To test the electrochemical behavior of the $\text{La}_{1-x}\text{Ca}_x\text{Fe}_{0.7}\text{Ni}_{0.3}\text{O}_{3-\delta}$ ($x = 0, 0.3, 0.5$)/VC compositions in alkaline solution, cyclic voltammograms (CVs) were registered within the potential limits of 0.93 – 1.66 V vs RHE for the LFN, LCFN3, LCFN5, and VC samples and of 0.93 - 1.63 V vs RHE for the LCFN5_m, and LCFN5_m S samples. Figure 25a compares the IR-corrected CVs with the current densities normalized to the geometric surface area of the disk electrode. The current density increases concomitantly with the degree of Ca doping. Notably, the LCFN5_m sample demonstrates higher currents if prior to the measurements the electrodes were soaked in alkaline solution. The current at 1.61 V for the LCNF5_m S sample is at least two times higher than the current for pristine LCFN5_m (Figure 25a).

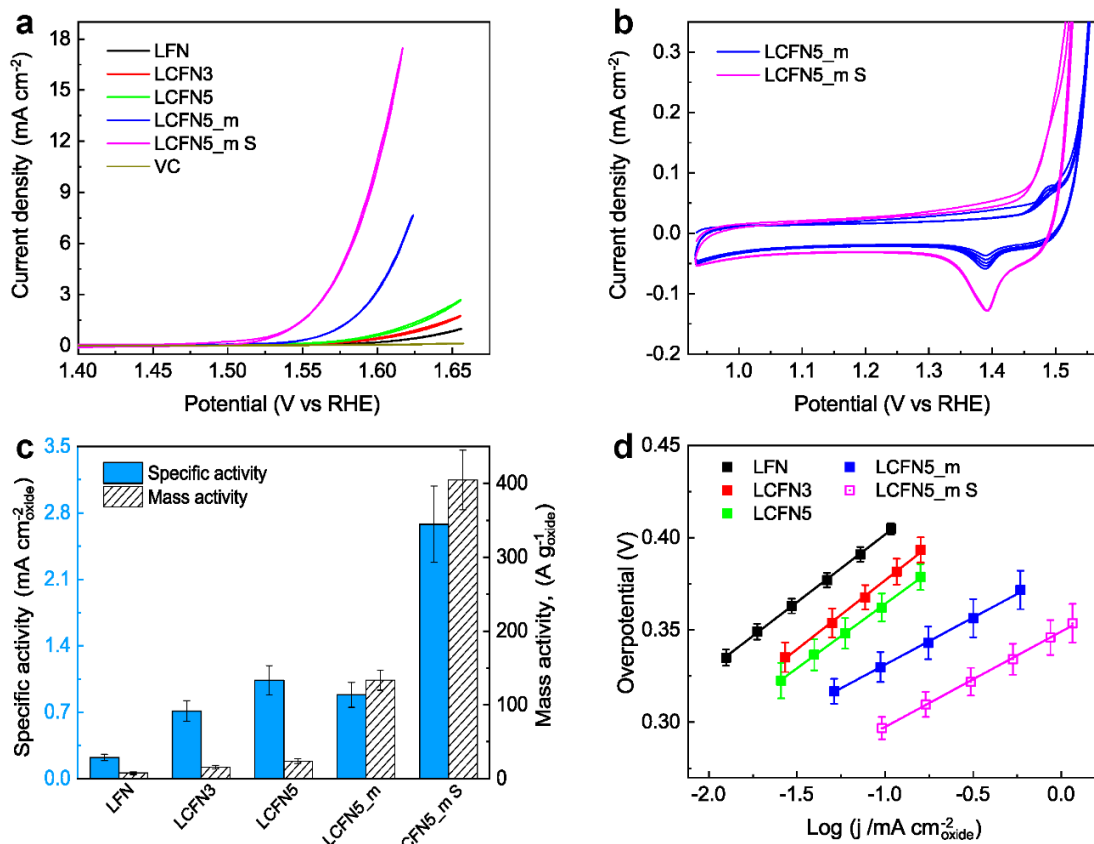


Figure 25. (a) CVs of LFN, LCFN3, LCFN5, LCFN5_m, LCFN5_m S (soaked for 48 h in 1M NaOH solution), and VC. (b) CVs of LCFN5_m in a narrow potential region (pristine and soaked electrodes). (c) Specific and mass activities at 1.61 V vs RHE. (d) Tafel plots for the catalysts. N₂ saturated 1M NaOH solution at 10 mV s⁻¹ and 1600 rpm. Total mass loading is 51 μg cm⁻², 30 wt.% VC.

To understand the origin of the electrocatalytic properties enhancement, we inspected the CVs of LCFN5_m at the potentials before the onset of O₂ evolution. In the 1.30 – 1.55 V range, the CVs demonstrate a pair of peaks at 1.49 and 1.39 V (Figure 25b). According to the analysis by Kuznetsov *et al.* [149] this is a surface redox transition associated with the activity of the Ni³⁺/Ni⁴⁺ redox couple, and consistent with the *in situ* soft X-ray absorption spectroscopy results reported by Drevon *et al.* [150]. However, in

some works this redox transition in perovskites is referred to as $\text{Ni}^{2+}/\text{Ni}^{3+}$ [133]. When cycling in alkaline solution, both anodic and cathodic peak's heights increase. Rough estimate of the number of Ni redox centers at (110) surface of the catalyst results in a surface charge density of $16 \mu\text{C cm}^{-2}_{\text{oxide}}$ for a one-electron transfer, while integration of the cathodic peak area at the first polarization cycle of the LCFN5_m sample gives $17 \mu\text{C cm}^{-2}_{\text{oxide}}$, which is close to the expected value for the surface monolayer redox transition. Calculation of charge density is described in Appendix, Figure S4. At the fifth polarization cycle the charge for the Ni redox peak is $38 \mu\text{C cm}^{-2}$. After that, the sample was kept in the PTFE cell for 48 hours in 1M NaOH and then cycled again (denoted LCFN5_m S). For the LCFN5_m S sample, the surface charge density reaches ca. $100 \mu\text{C cm}^{-2}_{\text{oxide}}$ (Figure 25b). Notably, the increase in the surface charge density in the region of $\text{Ni}^{3+}/\text{Ni}^{4+}$ redox transition was observed for LCFN5_m-based electrodes with different total mass loadings and catalyst-to-VC ratios (see further Figure 26a,b).

Such an increase in the charge density associated with surface redox would imply a surface reconstruction process, i.e. transformation of terminal layers of perovskite to (oxy)hydroxide-type $(\text{NiFe})\text{O}_x\text{H}_y$ layers. This is in a reasonable agreement with the recent observations of the formation of a Ni-(oxy)hydroxide layer for stable under the OER conditions perovskite LaNiO_3 [133]. Additionally, enhanced electrocatalytic activity after soaking Ni-based materials in alkaline electrolytes was reported previously [61],[28],[121] and attributed to the incorporation of Fe impurities present in the electrolyte (Fe_{aq}) into Ni-(oxy)hydroxide layer. Recent work also demonstrated that even small amount of Fe_{aq} can create dynamically stable interfaces with 3d transition metal

from (oxy)hydroxide layer [119],[120]. The active sites at the interface between Fe_{aq} and $(\text{Ni-Fe})\text{O}_x\text{H}_y$ layer can be responsible for the enhanced OER activity in this case. Correspondingly, high catalytic activity is to be expected for the Fe-rich materials reported in this study, where the Fe dissolution/redeposition process is likely to occur.

Relying on these considerations, the observed increase in the OER activity could be explained by such a plausible surface reconstruction and an increase in active surface area. The measured BET surface area for the soaked catalyst increases by ca. 14% from 15.1 to 17.1 $\text{m}^2 \text{g}^{-1}$, while the electrochemically active surface area (ECSA) increases by ca. 5 times (changes in ECSA were evaluated from the $\text{Ni}^{3+/4+}$ cathodic peak areas). However, much higher ECSA compared to BET surface area can be rationalized by the fact that the surface layers can be partially dissolved/detached from the surface or/and decomposed during the stages of sample preparation before BET measurement (washing/heating/drying). We assume that it is the interplay of these factors, which causes the increase of the electrocatalytic activity for the soaked samples.

Among all the samples, the electrode soaked in 1M NaOH solution prior to the measurements (LCFN5_m S) shows the highest electrocatalytic activity in OER. For this sample, the current density at 1.61 V vs RHE is roughly 17 times higher than that for the same composition prepared with the conventional USP method (LCFN5). For the LCFN5_m and LCFN5 samples, the mass activities equal to 134 and 23.6 $\text{A g}^{-1}_{\text{oxide}}$, while Tafel slopes are 51.0 ± 2.6 and $70.0 \pm 3.5 \text{ mV dec}^{-1}$, respectively (Figures 25c and 25d). The difference in the Tafel slopes might be explained by the much more homogeneous elemental distribution for the samples produced by the modified USP

technique. It should be noted however that correct experimental determination of the Tafel slope is often impacted by the insufficient conductivity of oxide-based electrocatalysts and the ensuing ohmic drop in the catalytic layer which is not easy to account for. In this context, high (close to 70 mV dec^{-1}) Tafel slopes of LFN, LCFN3 and LCFN5 samples (Figure 25c) may be attributed to their lower specific surface areas and thus poor mixing with carbon resulting in a higher ohmic resistance of the catalytic layers. Note that the highest Tafel slope ($98 \pm 4.9 \text{ mV dec}^{-1}$) was observed for the LCFN5_m sample without VC addition. The details on the activities and Tafel slopes for all the studied compositions are summarized in Table 10. The soaked LCFN5_m S sample shows the highest mass (ca. $400 \text{ A g}^{-1}_{\text{oxide}}$) and specific (ca. $2.4 \text{ mA cm}^{-2}_{\text{oxide}} / 0.5 \text{ mA cm}^{-2}_{\text{ECSA}}$) activities and a low $52 \pm 2.6 \text{ mV dec}^{-1}$ Tafel slope. Clearly, the observed trend in the increase of the specific activity implies the higher electrocatalytic activity of the Ca-doped samples.

4.3.1 Effects of catalyst loading and oxide/carbon ratio

The effect of catalyst loading (with a fixed oxide-to-carbon ratio of 70:30 wt.%) was examined for the most catalytically active LCFN5_m sample, without taking into account the soaked sample (Figure 26c,d). Currents at 1.61 V vs RHE for 12.7, 25.5 and $51 \mu\text{g cm}^{-2}$ total (oxide + VC) loadings equal to 102, 170 and $134 \text{ g}^{-1}_{\text{oxide}}$ respectively, with the sample with a relatively low loading ($25.5 \mu\text{g cm}^{-2}$) showing the best performance (Figure 26c,d).

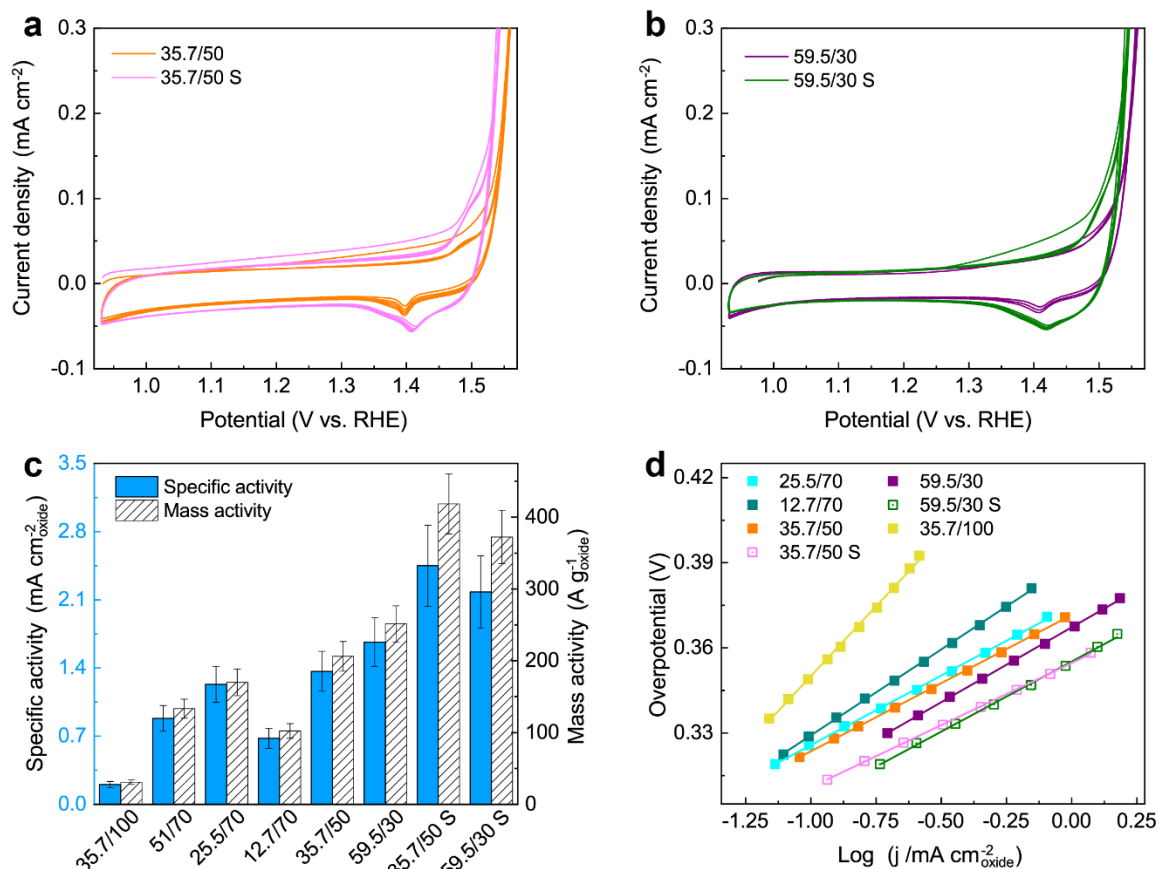


Figure 26. (a) CVs of the LCFN5_m electrodes before and after soaking for 48 hours (notation S) in 1M NaOH. Total loading 35.7 μg cm⁻²/50 wt.% oxide:50 wt.% VC; (b) total loading 59.5 μg cm⁻²/30 wt.% oxide:70 wt.% VC. N₂ saturated 1M NaOH solution, scan rate 10 mV s⁻¹, 1600 rpm. (c) Specific and mass activities of the LCFN5_m electrodes at 1.61 V vs RHE. The labels denote the total mass loading/oxide content. (d) Tafel plots for the studied compositions.

It can be speculated that the catalyst loading of 12.73 μg cm⁻² is too low to obtain a homogenous film, while for much higher loading of 51 μg cm⁻² the involvement of all the catalytic centers might be problematic due to the higher thickness of the film and blocking of the pores by oxygen bubbles.

At the next step, the optimal oxide to VC ratio was established. Apart from 70:30 wt.% ratio of perovskite to VC, we studied the electrode compositions at 50:50 and 30:70

wt.% ratios and 35.7, 59.5 $\mu\text{g cm}^{-2}$ total mass loadings. The Tafel slopes were found to slightly increase from 48 to 53 mV dec^{-1} when increasing the carbon content, yet the currents normalized to the BET surface area of the oxides are the highest for the 30:70 wt.% oxide:VC composition, which points to the higher utilization of the catalyst surface in the electrode compositions with high carbon content. For the soaked samples specific and mass activities do not show a clear correlation with the amount of VC and are approximately the same within the experimental error (15 and 10 %, respectively). We can speculate that with the increase in VC amount the problems of particle detachment from the electrode surface during prolonged soaking and poor adhesion aggravate, which inhibits direct quantitative comparison of the activities of soaked and pristine samples. Relying on the performed electrode composition optimization (Table 10, Figure 26), we conclude that the maximal activity of $420 \text{ A g}^{-1}_{\text{oxide}}$ and $2.45 \text{ mA cm}^{-2}_{\text{oxide}}$ at 1.61 V vs RHE can be reached for the 50:50 oxide:VC composition for the LCFN5_m S sample, which is higher than the activity reported for other perovskites with similar composition, such as $\text{La}_{0.4}\text{Sr}_{0.6}\text{Ni}_{0.5}\text{Fe}_{0.5}\text{O}_{3-\delta}$ ($\sim 375 \text{ A g}^{-1}_{\text{oxide}}$) [66], $\text{La}_{0.5}\text{Sr}_{0.5}\text{Ni}_{0.4}\text{Fe}_{0.6}\text{O}_{3-\delta}$ ($66 \text{ A g}^{-1}_{\text{oxide}}$ and $0.44 \text{ mA cm}^{-2}_{\text{oxide}}$) [67], $\text{La}_{0.5}\text{Sr}_{0.5}\text{Ni}_{0.8}\text{Fe}_{0.2}\text{O}_{3-\delta}$ ($68 \text{ A g}^{-1}_{\text{oxide}}$ and $1.2 \text{ mA cm}^{-2}_{\text{oxide}}$) [68], and IrO_2 ($\sim 165 \text{ A g}^{-1}_{\text{oxide}}$ and $1.1 \text{ mA cm}^{-2}_{\text{oxide}}$) [71]. Table 2 in Section 2.4 collects the reported OER activity values for other catalysts.

Table 10. OER current densities at 1.61 V vs RHE and Tafel slopes for the perovskite samples measured in different experiments.

Sample	Loading ($\mu\text{g cm}^{-2}$)	Oxide to VC ratio (wt.%)	Specific activity ($\text{mA cm}^{-2}_{\text{oxide}}$)	Mass activity ($\text{A g}^{-1}_{\text{oxide}}$)	Current density (on disk) (mA cm^{-2})	Tafel slope <i>b</i> (mV dec^{-1})
			1.61 V vs RHE			
LFN	51	70 – 30	0.22	7.55	0.28	75±3.8
LCFN3	51	70 – 30	0.70	15.5	0.56	75±3.9
LCFN5	51	70 – 30	1.03	23.6	0.85	70±3.5
LCFN5_m S*	51	70 – 30	2.37	404	14.45	52±2.6
LCFN5_m	51	70 – 30	0.89	134	4.77	51±2.6
VC	41.65	0 – 100	0.00084	1.80	0.075	NA
LCFN5_m	35.7	100 – 0	0.20	30	1.10	98±4.9
Different mass loadings						
LCFN5_m	25.5	70 – 30	1.13	170	3.03	49±2.4
LCFN5_m	12.7	70 – 30	0.68	102	0.91	60±3
Vulcan carbon content increasing at a fixed perovskite loading						
LCFN5_m	35.7	50 – 50	1.37	206	3.68	48±2.4
LCFN5_m	59.5	30 – 70	1.67	252	4.49	53±2.6
Soaked in 1M NaOH						
LCFN5_m S*	35.7	50 – 50	2.45	420	7.47	44±2.2
LCFN5_m S*	59.5	30 – 70	2.18	373	6.65	49±2.5

*S - soaked ca. 48 h in 1M NaOH solution

4.4 Catalyst stability

In section 4.2 we demonstrated the bulk stability of $\text{La}_{0.6}\text{Ca}_{0.4}\text{Fe}_{0.7}\text{Ni}_{0.3}\text{O}_{2.9}$ using PXRD after soaking in alkaline solution for 4 weeks, without polarization. In order to check surface stability and to better understand the surface transformations, that are indirectly revealed in the shape of the electrochemical curves, we examined the sample LCFN5_m without VC, which was soaked for 1 week in 1M NaOH solution without polarization, with XPS. Additionally, the electrolyte after soaking was studied with ICP-

AES for detection of the dissolved degradation products. The detected amount of dissolved La in 1M NaOH solution equal to $0.017 \pm 0.003 \text{ mg L}^{-1}$, which corresponds to ca. 0.25% of dissolved lanthanum from one surface monolayer, which is in line with the PXRD pattern of the soaked sample, where noticeable changes in the reflections and cell parameters of the perovskite phase were not observed (Figure 17, Table 6). Another LCFN5_m sample was soaked for 2 weeks with the addition of VC in the amount used for the electrode preparation (~1-2 mg) and investigated with STEM-EDX mapping (Figure 27, 28). STEM-EDX mapping also did not reveal noticeable compositional change within the sensitivity and spatial resolution limits.

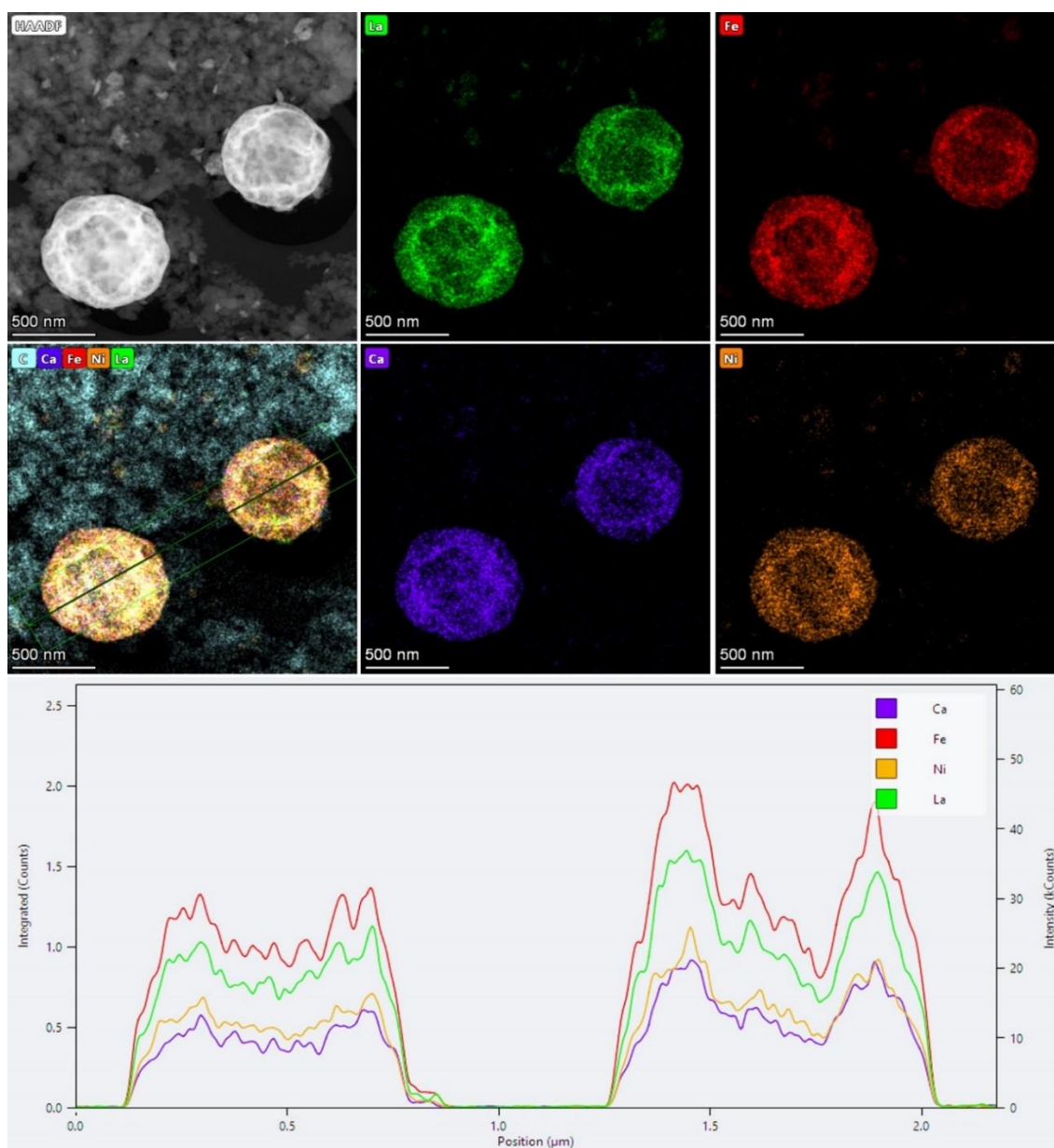


Figure 27. HAADF-STEM image of spherical particles in the LCFN5_m_S (soaked for 2 weeks) sample mixed with Vulcan carbon along with the La, Ca, Fe, Ni and a mixed color compositional STEM-EDX maps. The green line in the mixed compositional map indicates the direction for plotting the EDX signal profile. The profile does not show any cation segregation at the edges of the spherical agglomerates. Higher EDX signal at the edges of the spherical agglomerates corroborates their hollow nature.

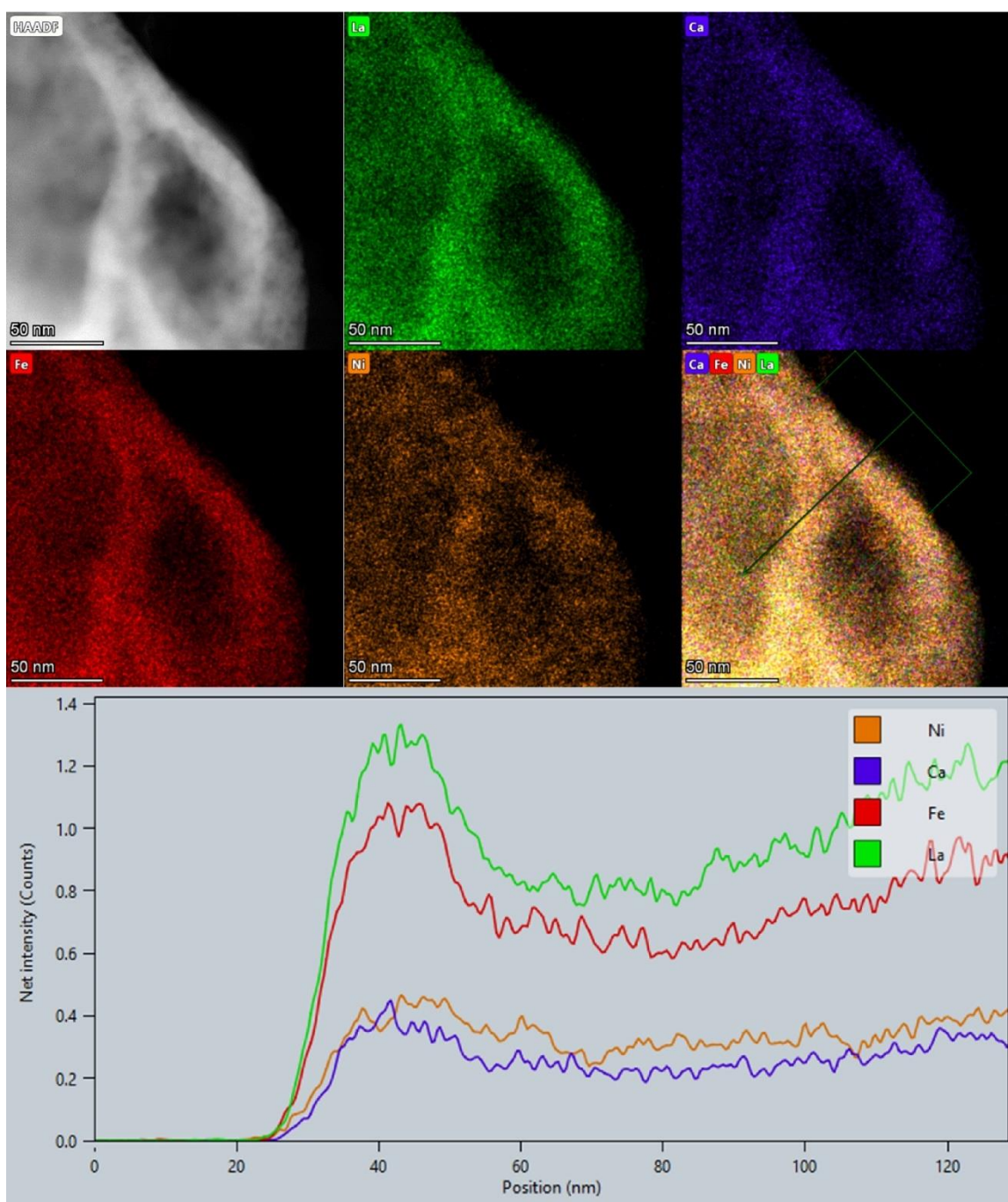


Figure 28. HAADF-STEM image of the zoomed area of a spherical particle in the LCFN5_m_S (soaked for 2 weeks) sample mixed with Vulcan carbon along with the La, Ca, Fe, Ni STEM-EDX maps and a mixed color-coded compositional map. The green line in the mixed compositional map indicates the direction for plotting the EDX signal profile. The profile does not show any cation segregation at the edge of the spherical agglomerate.

However, some changes were observed in the XPS spectra (Figure 29, 30) for the LCFN5_m S sample compared to that of the LCFN5_m. The Fe2p_{3/2} spectrum is not noticeably affected by soaking. The main Fe2p_{3/2} peak “a” is located at 710.0 eV, this position is in the range of binding energy (BE) of Fe₃O₄, Fe₂O₃ and FeOOH which can be found in National Institute of Standards and Metrology (NIST) references at the BE of 710.5 eV and 711.0 eV, respectively. But the Ni2p_{1/2} spectrum demonstrates slight increase of intensity at 873.2 eV (Ni2p_{1/2} photoelectron line has been chosen for analyses, because of the overlap between the more intense Ni2p_{3/2} with La3d_{3/2} lines).

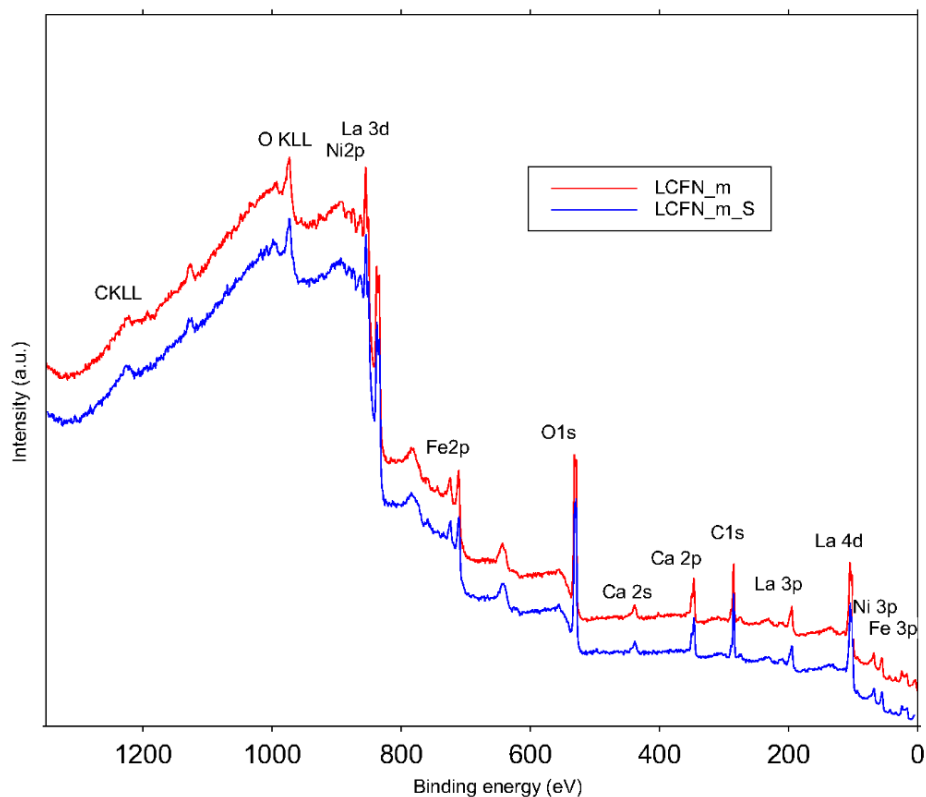


Figure 29. XPS survey spectra were taken from the LCFN5_m and LCFN5_m_S (soaked 1 week) samples. Spectra were shifted in Y-axis for presentation. NIST X-ray photoelectron spectroscopy database has been used for reference.

The position of the main peak “a” maximum of Ni2p_{1/2} is at 873.2 eV which correspond to BE of NiO, Ni(OH)₂ and NiOOH in the same range, according to NIST. This is indicative of the formation of (oxy)hydroxides on the surface of the material soaked in alkaline solution, in conjunction with the increase of the intensity at 531.2 eV in the O1s spectra after soaking [151] (Table 11) and increased Ni redox charge density on CVs.

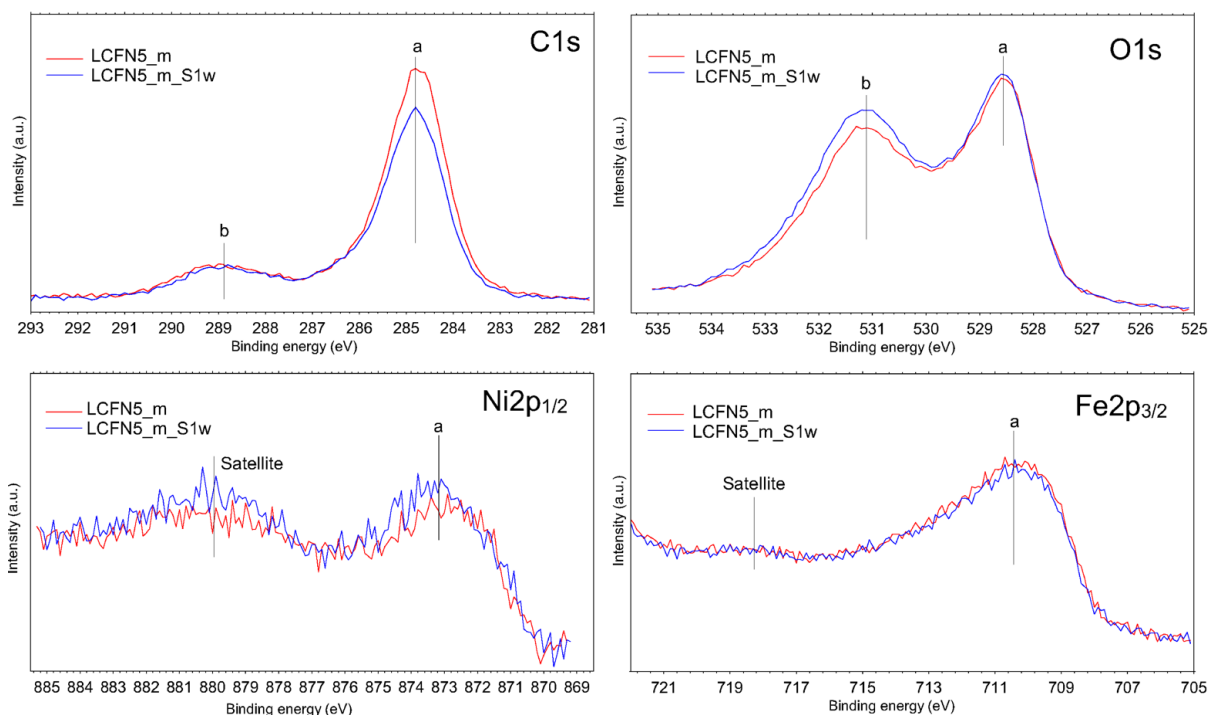


Figure 30. High-resolution XPS spectra (Al K_α ~ 5 nm information depth) taken from the LCFN5_m and LCFN5_m S (soaked 1 week) samples.

The O1s peak “a” centered at 528.6eV can be attributed to the “O²⁻” anions of the oxide crystalline framework. The second broader peak “b” at 531.1eV can be assigned to oxygen atoms incorporated in wide range of species, such as carbonates, bicarbonates, hydroxides. Additionally, the NaOH soaking reduces the height of most prominent C1s peak “a”, which comes from adventitious carbon (C-C, C=C, C-H), thus NaOH treatment

cleans the surface of the material from aliphatic carbon contamination and decreasing the hydrophobic character of the surface. An additional wide peak “b” centered at 288.9 eV can be assigned to HCO_3^- anions.

Table 11. The element concentrations on the surface of materials calculated from the XPS spectra.

Sample	Atomic concentration at. %					
	C	O	Fe	Ni	La	Ca
LCFN5_m	32.4	47.7	5.9	4.1	5.7	4.2
LCFN5_m S*	27.7	51.7	5.8	4.5	5.9	4.4

* S – soaked 1 week

The fact that this (oxy)hydroxide-like layer is not observed in extensive TEM analysis indicates that it is very thin and comprises only several monolayers. Moreover, quantification of the surface cation composition (information depth ~ 5 nm) reveals no change in the Fe/Ni ratio within the experimental accuracy (Table 12) and no change in the (La,Ca)/(Fe,Ni) atomic ratio indicating that the core-perovskite structure is preserved.

Table 12. The average stoichiometry of the cations on the surface.

Sample	Fe	Ni	La	Ca
LCFN5_m	0.6	0.4	0.6	0.4
LCFN5_m S*	0.6	0.4	0.6	0.4

* S – soaked 1 week. The total number of cations is taken as 2 to compare with bulk perovskite stoichiometry ABO_3

Thus, the analysis of the XPS spectra suggests that the NaOH-soaking cleans the surface from carbon contamination and reconstructed terminal layers which, however, does not lead to deep perovskite degradation.

4.4.1 Catalyst stability under potentiostatic and galvanostatic measurement conditions

RRDE cyclic voltammetry was performed to verify that the measured OER current is not perturbed by the side reactions and corrosion of the electrode material. RRDE CVs were registered for the LCFN5_m catalyst (30 wt.% VC). The total mass loading was $25.5 \mu\text{g cm}^{-2}$ to minimize the effect of extensive bubble formation during the OER. The Au ring was poised at 0.3 V vs RHE and the O_2 generated at the disk was reduced at the ring electrode. A typical synchronous increase of the disk and ring currents with increasing the disk potential is observed in all RRDE CVs for catalysts (Figure 31a). To accurately evaluate faradaic efficiency (FE) and to minimize capacitive contributions, RRDE experiments were performed under potentiostatic conditions at the potentials between 1.53 and 1.63 V. FE was calculated from ring and disk currents as follows:

$$FE = \frac{I_{\text{ring}} \left(\frac{4}{n_{\text{ORR}}} \right)}{NI_{\text{disk}}}, \quad (10)$$

where $n_{\text{ORR}} = 2$ (is the number of electrons for the reaction at Au ring electrode).

At all potentials (except 1.53 V where background currents interfere with the low faradaic currents) the FE is close to 100% (Figure 31b), which confirms that the registered current relates to the OER process, within the 4% accuracy of the RRDE measurements.

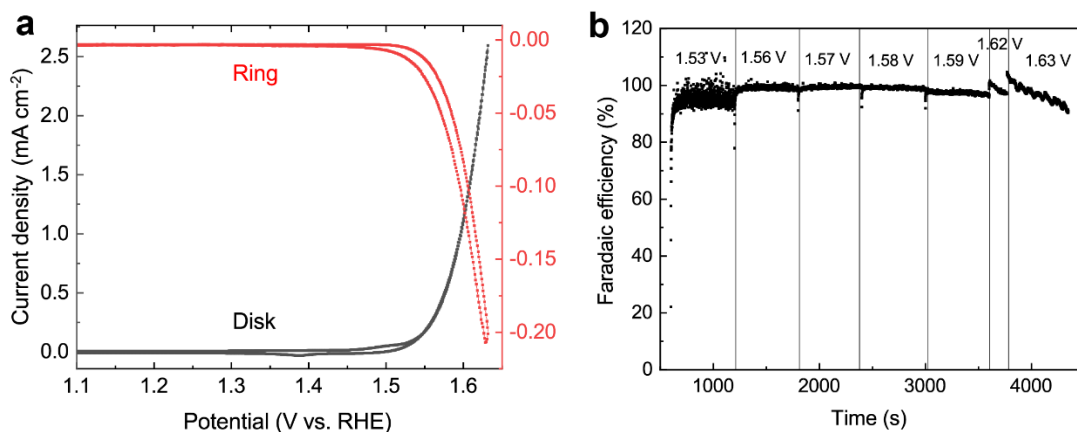


Figure 31. (a) RRDE CVs (not IR-corrected) of the GC-supported LCFN5_m catalyst (total mass loading $25.5 \mu\text{g cm}^{-2}$, 30 wt.% VC) at 10 mV s^{-1} and 1600 rpm in N_2 -saturated 1 M NaOH. (b) Faradaic efficiency measured under potentiostatic conditions at potentials ranging from 1.53 to 1.63 V. $E_{\text{Ring}} = +0.3 \text{ V vs RHE}$. Ring currents are corrected to background ring currents.

To further examine the compositional and morphological changes under the OER conditions, two electrodes consisting of the LCFN5_m catalyst mixed with 30 wt.% of VC were polarized potentiostatically at 1.53 - 1.63 V vs RHE for 2 h (Figures 31b) and galvanostatically at $10 \text{ A g}^{-1}_{\text{oxide}}$ for 8 h (Figure 32).

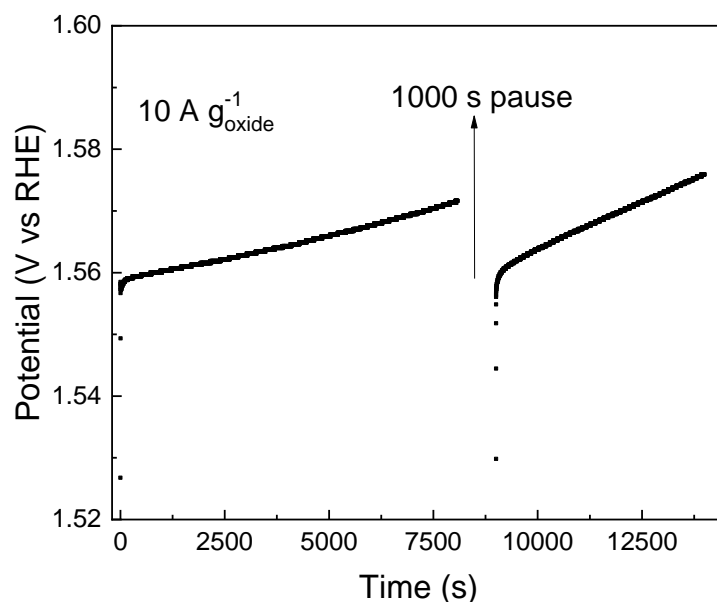


Figure 32. Constant current test of LCFN5_m at $10 \text{ A g}^{-1}_{\text{oxide}}$. Mass loading $25.5 \mu\text{g cm}^{-2}$, 30 wt.% VC. N_2 -saturated 1 M NaOH solution, 1600 rpm.

HAADF-STEM imaging and STEM-EDX maps of the LCFN5_m spherical particles reveal neither noticeable changes in the elemental distribution nor preferential segregation of the La, Ca, Fe or Ni cations at the surface of the particles within the experimental detection limit indicating that massive leaching of these cations from the perovskite structure and re-depositing in a form of another phase at the surface does not occur (Figure 33, 34).

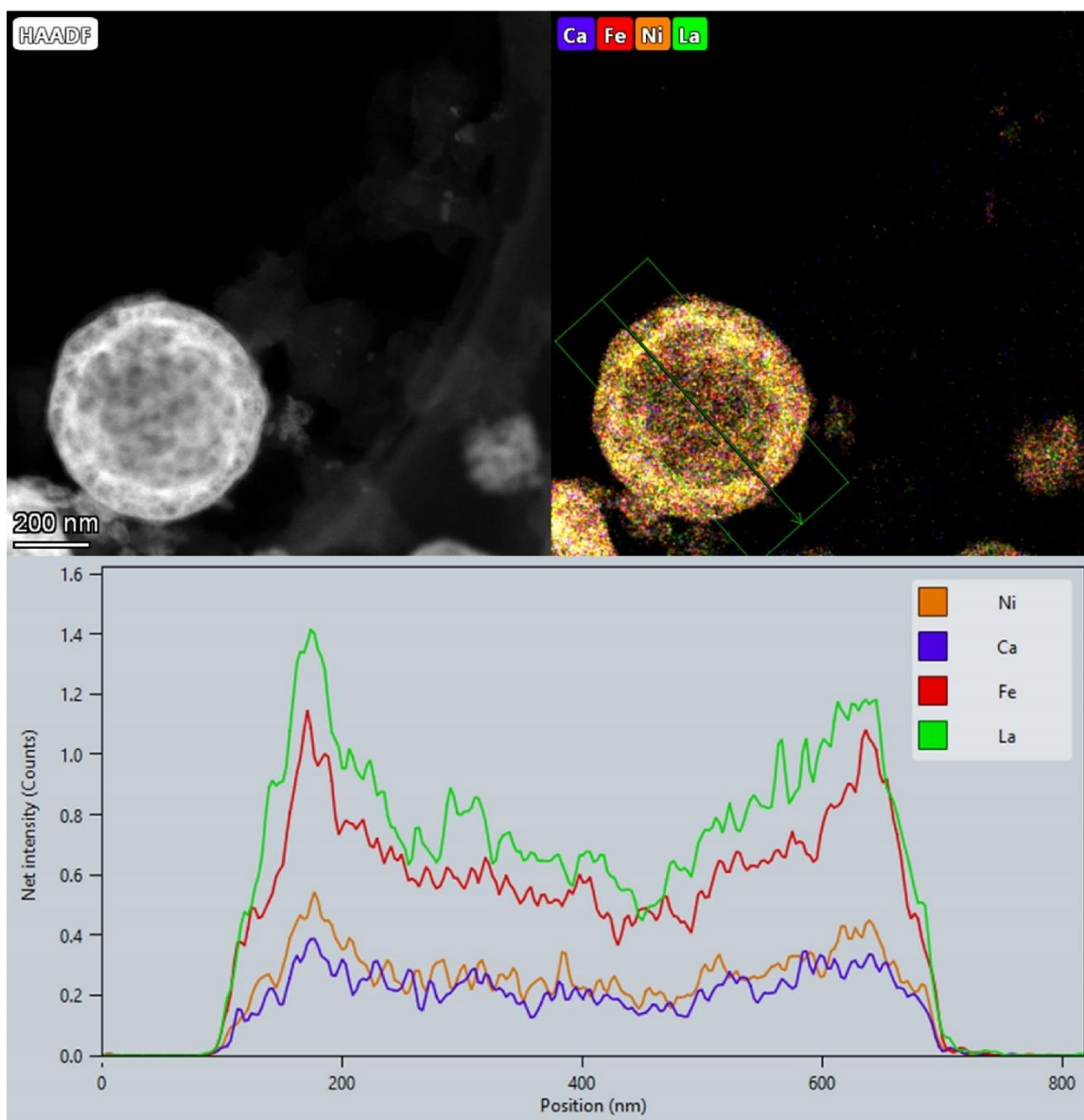


Figure 33. HAADF-STEM image along with the La, Ca, Fe, Ni STEM-EDX maps of the LCFN5_m sample mixed with Vulcan carbon after electrochemical measurements for 2 hours in chronoamperometric regime (at 1.53-1.63V vs RHE). The green line in the mixed compositional map indicates the direction for plotting the EDX signal profile. The profile does not show any cation segregation at the edges of the spherical agglomerate.

An additional ICP-MS analysis of the electrolyte (after 30 cycles from 0.93 to 1.65 V, electrode with $51 \mu\text{g cm}^{-2}$ loading) was performed for the LCFN5_m sample. The revealed La concentration in the electrolyte after cycling is $< 0.08 \mu\text{g L}^{-1}$, which is equal

to ca. 0.5% of dissolved La from the total amount in perovskite and corresponds roughly to half of monolayer. These data are in line with the suggested transformation/restructuring of the surface with the formation of a thin (oxy)hydroxide layer as observed for the perovskites and other systems [133],[152]. Such surface restructuring could be driven by shallow A-site dissolution. Similar surface transformation, which only involves a few monolayers, was demonstrated for LaNiO_3 [153]. In clear contrast, catalysts like $\text{Ba}_{0.5}\text{Sr}_{0.5}\text{Co}_{0.8}\text{Fe}_{0.2}\text{O}_{3-\delta}$ form a thick amorphous oxide layer which is several nm thick [115]. The shallow amorphous layer is, however, visible at the surface of the sphere in Figure 34. The nature of this layer was clarified from thorough TEM investigation of the potentiostatically polarized LCFN5_m electrode. The STEM-EDX maps and corresponding EDX signal profiles across the layer (indicated with an arrow Figure 34) demonstrate absence of cations composing the LCFN5_m perovskite (La, Ca, Fe and Ni), but merely the presence of C and F as the main constituents that are the components of Nafion covering the catalyst particles. No cation segregation and/or preferential leaching are observed at the surface of the particles. Thus, extensive TEM imaging and compositional mapping of the samples treated with and without polarization at different conditions in combination with the ICP-AES/MS data suggest that the $\text{La}_{0.6}\text{Ca}_{0.4}\text{Fe}_{0.7}\text{Ni}_{0.3}\text{O}_{2.9}$ perovskite undergoes only minor surface changes under the electrocatalytic conditions.

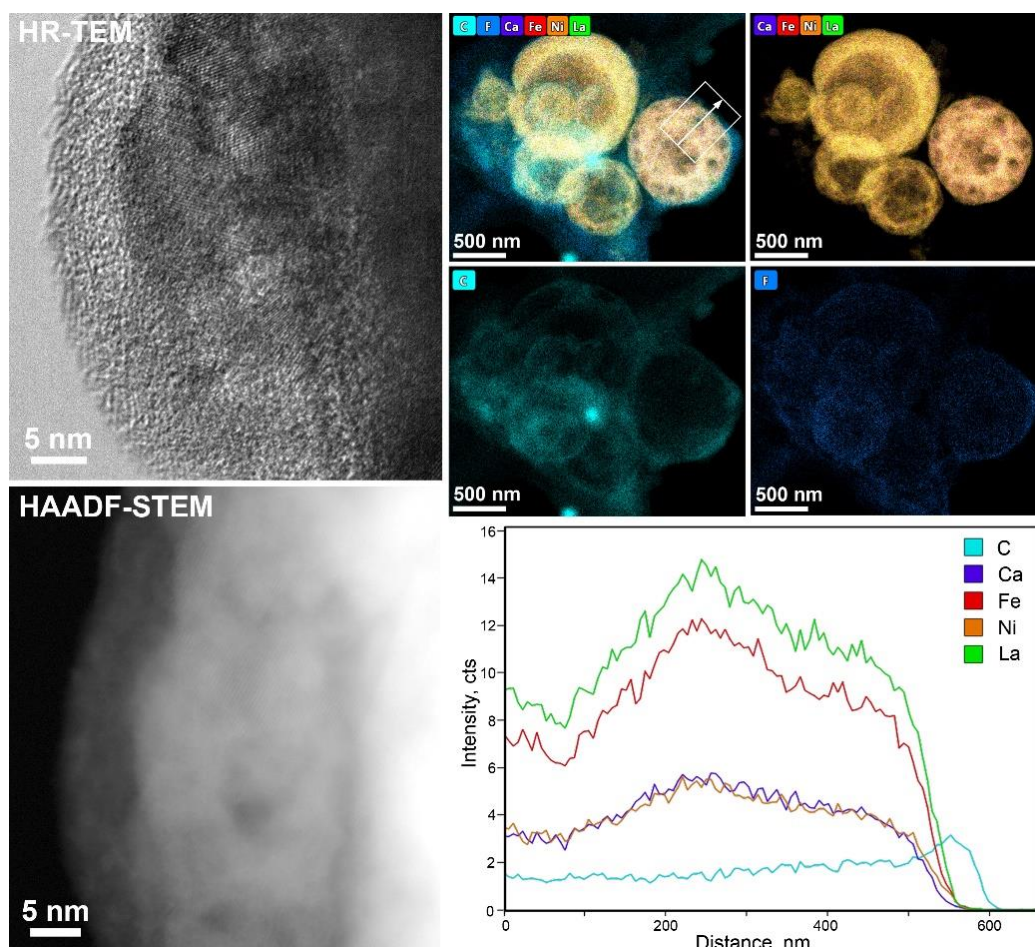


Figure 34. HR-TEM and HAADF-STEM images of the LCFN5_m catalyst polarized galvanostatically at $10 \text{ A g}^{-1}_{\text{oxide}}$ for 8 h. Amorphous layer is clearly visible at the surface of a spherical particle.

Electrochemical tests of the catalyst operation in the galvanostatic conditions ($10 \text{ A g}^{-1}_{\text{oxide}}$) show a slight increase in overpotential (Figure 32), which may be associated with two factors: blocking of the catalyst surface by oxygen bubbles or/and slight leaching of cations and loss of active sites, which, however, is not detected by HR-TEM (due to the fact that this leaching is insignificant and the surface layer of Nafion hides changes in the perovskite surface). After stopping measurements and rinsing the electrode, a low overpotential is again attained, which indicates some reversibility of the

process of increasing the overpotential, and this requires further detailed research. In the light of recent data, emphasizing the importance of $\text{Fe}_{(\text{aq})}$ for the activity and stability of catalysts during OER [119],[120], in the Section 4.6 we will consider electrochemical experiments with the most common impurity in alkaline electrolytes – Fe ions.

4.5 DFT+U calculations

To understand the origin of higher catalytic activity in the case of the Ca-substituted $\text{La}_{0.6}\text{Ca}_{0.4}\text{Fe}_{0.7}\text{Ni}_{0.3}\text{O}_{2.9}$ compared to that of the $\text{LaFe}_{0.7}\text{Ni}_{0.3}\text{O}_3$ counterpart we calculated spin-polarized PDOS using the DFT+U method. We used pseudocubic cells with 40 atoms for both structures and adopted experimental lattice vectors $a_1 = [7.733, -0.01, -0.032]$, $a_2 = [-0.022, 7.733, -0.032]$, $a_3 = [0.0, 0.0, 7.733]$ while allowing full optimization of atomic positions. As the reasonable models of the $\text{La}_{0.6}\text{Ca}_{0.4}\text{Fe}_{0.7}\text{Ni}_{0.3}\text{O}_{2.9}$ and $\text{LaFe}_{0.7}\text{Ni}_{0.3}\text{O}_3$ solid solutions, we used $\text{La}_{0.625}\text{Ca}_{0.375}\text{Fe}_{0.75}\text{Ni}_{0.25}\text{O}_3$ and $\text{LaFe}_{0.75}\text{Ni}_{0.25}\text{O}_3$ ordered phases, respectively. At the first step, the most favorable Ni positions were found by enumerating all possible non-equivalent symmetry configurations. The lowest energy structure is shown in Figure 35a. Then, using this geometry the most favorable arrangement was found for Ca atoms (Figure 35b).

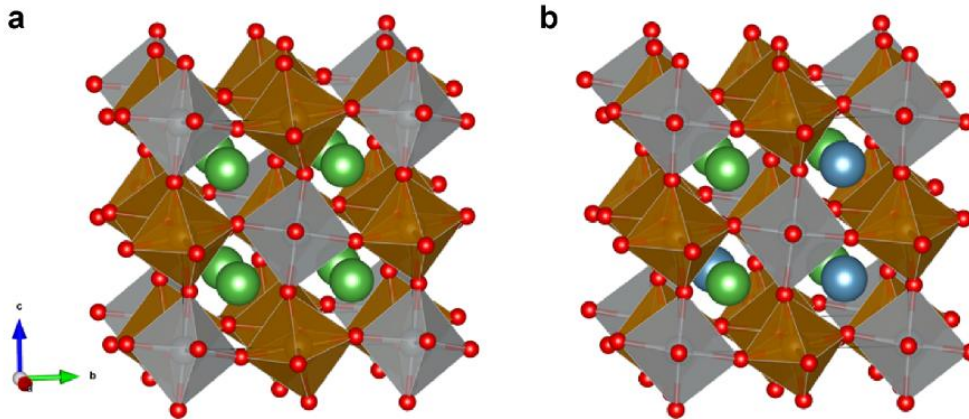


Figure 35. (a) The pseudocubic 40 atom supercells used as computational models for $\text{LaFe}_{0.75}\text{Ni}_{0.25}\text{O}_3$ ($Pbnm$) and (b) $\text{La}_{0.625}\text{Ca}_{0.375}\text{Fe}_{0.75}\text{Ni}_{0.25}\text{O}_3$ ($R-3c$). La, Ca, Fe, Ni, and oxygen are shown with green, blue, brown, grey, and red spheres, respectively.

The calculated local PDOS for d and p orbitals for the described models are shown in Figure 36. Focusing first at $\text{LaFe}_{0.75}\text{Ni}_{0.25}\text{O}_3$ (Figure 36a), both Fe and Ni have a non-zero density of states at Fermi level emphasizing the metallic behavior of this compound. The $2p$ orbitals of oxygen strongly hybridize with $3d$ orbitals of Ni and Fe. The DOS at Fermi level comes predominantly from O $2p$ orbitals. The partial filling of O $2p$ states shows that LFN can be considered as an O $2p$ metal with holes in the valence band practically not associated with Ni ions. This is in line with earlier LDA+U results obtained for nickelates [154]. By moving from LaFeO_3 , which is an insulator, to LFN the d -PDOS at the Fe atoms remains almost the same, while the main difference is due to the shifting of the Fermi level to lower energies. Overall, our local PDOS for Fe and Ni are in line with that calculated for LaFeO_3 [145] and LaNiO_3 [154],[155].

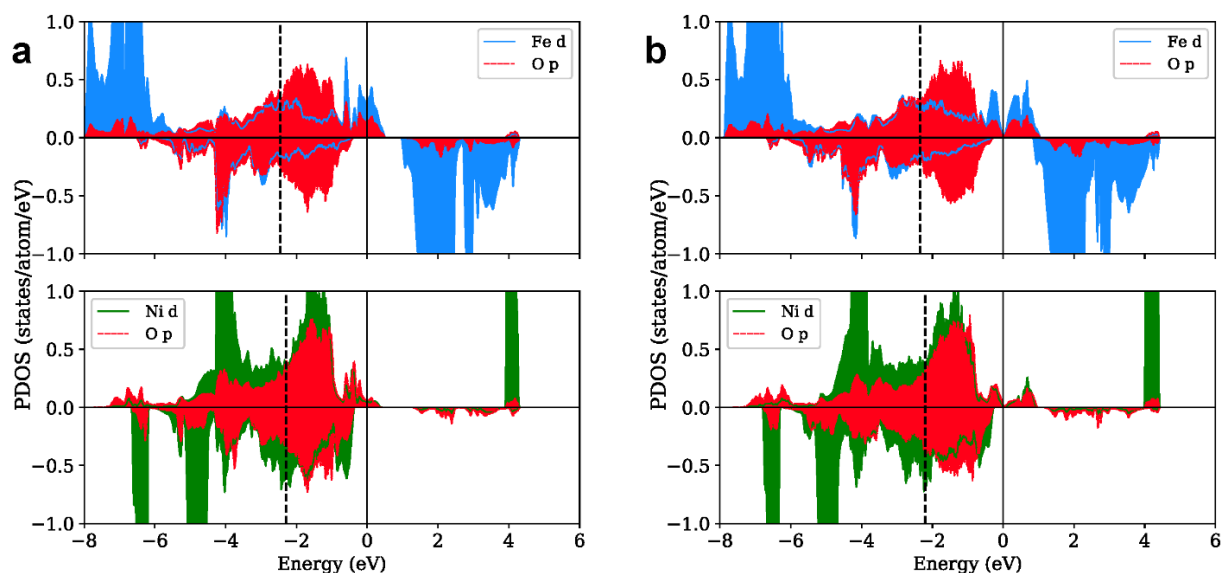


Figure 36. Local spin-polarized PDOS for (a) $\text{LaFe}_{0.75}\text{Ni}_{0.25}\text{O}_3$, (b) $\text{La}_{0.625}\text{Ca}_{0.375}\text{Fe}_{0.75}\text{Ni}_{0.25}\text{O}_3$ for O 2p and Fe, Ni 3d orbitals. The PDOS O 2p-orbitals is provided on the six oxygen atoms that form an octahedron around the corresponding Fe, Ni atom (normalized). The solid vertical line shows the Fermi level. The dashed vertical line shows the 2p-band center: (a) -2.46 and -2.30 eV, (b) -2.36 and -2.20 eV.

The partial replacement of La with Ca results in concurrent oxidation of Fe, Ni and O, causing the following changes (Figure 36b): (i) diminishing of PDOS at the Fermi level, (ii) downshift of the Fermi level relative to the O 2p-band center (dashed vertical line), (iii) increase of the number of empty states above the Fermi level and overall broadening of the band around the Fermi level. The two latter changes can explain the higher catalytic activity of $\text{La}_{0.6}\text{Ca}_{0.4}\text{Fe}_{0.7}\text{Ni}_{0.3}\text{O}_{2.9}$. Shifting the center of O 2p-band closer to the Fermi level is a direct indicator of decreasing energy of oxygen vacancy formation $\Delta E_{V(\text{O})}$ as a strong correlation is established between $\Delta E_{V(\text{O})}$ and $E_{\text{F}} - E_{\text{O}2\text{p}}$ energy difference in perovskites [114].

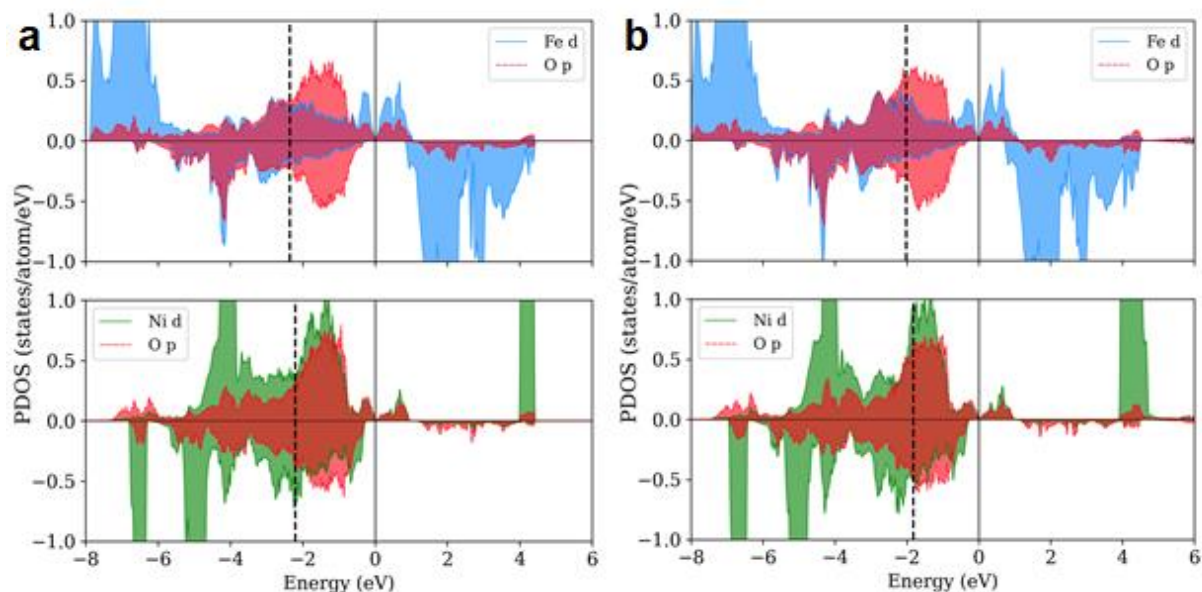


Figure 37. Local spin-polarized PDOS for (a) $\text{La}_{0.625}\text{Ca}_{0.375}\text{Fe}_{0.75}\text{Ni}_{0.25}\text{O}_3$ and (b) $\text{La}_{0.625}\text{Sr}_{0.375}\text{Fe}_{0.75}\text{Ni}_{0.25}\text{O}_3$ for O 2p and Fe, Ni 3d orbitals. The PDOS of O 2p-orbitals is provided on the six oxygen atoms that form an octahedron around the corresponding Fe, Ni atom (normalized). The solid vertical line shows the Fermi level. The dashed vertical line shows the 2p-band center: (a) -2.36 and -2.20 eV, (b) -2.11 and -1.81 eV.

It is worth noting that Sr-doped perovskites have a similar electronic structure (Figure 37b). However, the Sr for La substitution shifts the 2p-band center even closer to the Fermi level that can lead to enhanced cation leaching and surface amorphization [109], while the position of the 2p-band center in the Ca-substituted perovskites provides an optimal compromise between the stability and catalytic activity. Being combined with notable oxygen deficiency in $\text{La}_{0.6}\text{Ca}_{0.4}\text{Fe}_{0.7}\text{Ni}_{0.3}\text{O}_{2.9}$, decreasing $\Delta E_{V(\text{O})}$ results in faster lattice O_2 evolution accompanied with cation dissolution process which results in the surface restructuring [113]. Thus the primary role of Ca^{2+} doping stems from decreasing oxygen vacancy formation energy by shifting of the O 2p band towards the Fermi level, which provokes (seemingly) faster perovskite surface reconstruction with A-site cation

leaching and (oxy)hydroxide layer formation based on B-site cation, which results in stronger interaction with active Fe species than in electrolyte [119]. Additionally, the increase of the bandwidth around the Fermi level should facilitate electron exchange at the catalyst interface and, according to the Gerischer–Marcus model of the charge transfer, improve the rate of redox reactions [9],[156]. A significant lowering $\Delta E_{V(O)}$ compromises the stability of the perovskite catalyst as exemplified with the $Ba_{1-x}Sr_xCo_{1-y}Fe_yO_{3-\delta}$ perovskites when the rate of cation leaching can exceed with the rate of redeposition, which raises a question about durability of catalysts under certain conditions [115],[127],[119]. Thus, increasing catalytic activity by adjusting $\Delta E_{V(O)}$ and metal-oxygen covalence is always a compromise with catalyst stability. It seems that $La_{0.6}Ca_{0.4}Fe_{0.7}Ni_{0.3}O_{2.9}$ provides a reasonable compromise, since no massive amorphization and degradation were observed after electrochemical testing with and without polarization.

4.6 Catalyst activity and stability in the electrolyte with trace amounts of Fe

The results presented in this Section are based on the following publication: Porokhin S. V., Nikitina V. A., Abakumov A. M. Enhancement of Catalytic Activity and Stability of $La_{0.6}Ca_{0.4}Fe_{0.7}Ni_{0.3}O_{2.9}$ Perovskite with ppm Concentration of Fe in the Electrolyte for the Oxygen Evolution Reaction. *Materials* 14.21 (2021): 6403.

The OER activity of LCFN5_m was evaluated in Ar-saturated 1M NaOH solution. CVs were registered within the potential limits of 0.93 – 1.66 V vs RHE. The

IR-corrected CVs in Figure 38a,b compare the current densities normalized to the geometric surface area of the RDE. A much higher current density (12.9 mA cm^{-2} at 1.61 V vs RHE) was observed with adding Fe ions to the electrolyte in 1 ppm concentration, compared to the as-prepared pristine electrolyte (3.0 mA cm^{-2} at 1.61 V vs RHE). The Tafel slope in the Fe-modified electrolyte is significantly lower ($44.0 \pm 2.4 \text{ mV dec}^{-1}$) indicating faster reaction kinetics compared to $52.0 \pm 2.6 \text{ mV dec}^{-1}$ in the pristine electrolyte (Figure 38c).

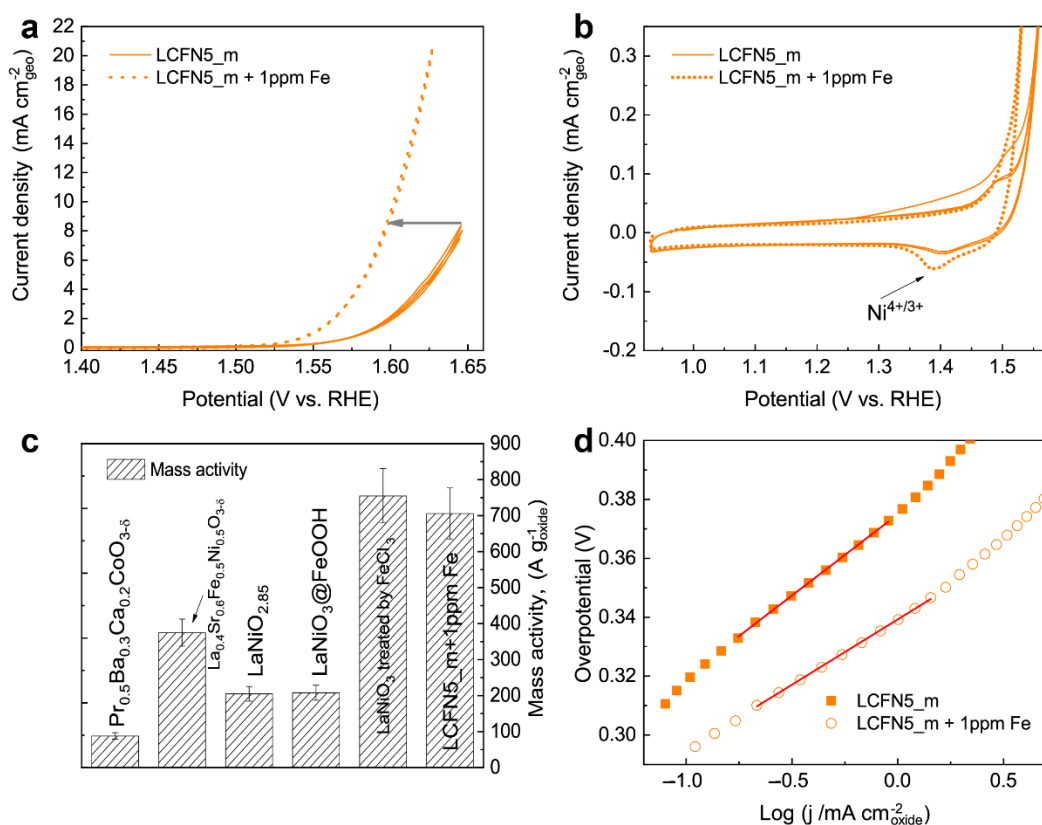


Figure 38. (a) CVs of the LCFN5_m perovskite in as-prepared pristine electrolyte and with the addition of 1 ppm Fe_{aq}. Currents are normalized to the geometric area of the electrode. (b) Enlarged regions of the CVs. (c) Mass activities at 1.61 V vs RHE of LCFN5_m+Fe_{aq} and comparison with other OER catalysts [125],[126],[157],[66],[158]. (d) Tafel plots for LCFN5_m in the as-prepared electrolyte and with the addition of 1 ppm Fe_{aq}. Ar-saturated 1M NaOH solution, scan rate 10 mV s^{-1} , rotation rate 1600 rpm, total mass loading $35.7 \mu\text{g cm}^{-2}$, 50 wt.% VC.

The LCFN5_m perovskite demonstrates a superior OER catalytic activity of $706 \pm 71 \text{ A g}^{-1}_{\text{oxide}}$ at 1.61 V vs RHE, which is comparable to that (assuming 10% uncertainty) for LaNiO_3 covered with amorphous Ni-Fe (oxy)hydroxide after post-treatment by FeCl_3 ($755 \pm 76 \text{ A g}^{-1}_{\text{oxide}}$) [125], pristine (Ni-Fe) hydroxides ($600 \pm 60 \text{ A g}^{-1}_{\text{oxide}}$) [61], and outperforms other top perovskite catalysts, such as $\text{Pr}_{0.5}\text{Ba}_{0.3}\text{Ca}_{0.2}\text{CoO}_{3-\delta}$ ($85 \pm 9 \text{ A g}^{-1}_{\text{oxide}}$) [157] and $\text{La}_{0.4}\text{Sr}_{0.6}\text{Ni}_{0.5}\text{Fe}_{0.5}\text{O}_{3-\delta}$ ($375 \pm 38 \text{ A g}^{-1}_{\text{oxide}}$) [66] (Figure 38d).

We also measured the initial amount of Fe ions in aqueous 50 wt.% solution of NaOH (Sigma-Aldrich) by ICP-AES and observed $1200 \mu\text{g L}^{-1}$ concentration that corresponds to $63.4 \mu\text{g L}^{-1}$ ($\sim 0.063 \text{ ppm}$) in the as-prepared pristine 1M NaOH electrolyte. Therefore, 1 ppm of Fe is a significant addition which substantially improves the OER activity. Moreover, the potentials of the $\text{Ni}^{4+/3+}$ redox peaks were slightly shifted after immersion in 1 ppm Fe_{aq} electrolyte (Figure 38b) [121],[159],[37] evidencing that Fe incorporates/adsorbs on the surface, increasing the capacity of the cathodic peak, which is related to the formation of thicker or more redox active Ni-Fe (oxy)hydroxide layer [37],[133]. The LCFN5_m sample demonstrates an improvement factor (ratio of current values in the 1 ppm Fe_{aq} electrolyte and in the pristine electrolyte) equal to 3.9. Such improvement, however, was not achieved immediately, but after 20 hours of soaking the LCFN5 electrode in the pristine electrolyte. If the measurements were performed without preliminary soaking or additional cycling, the improvement factor was 2.5 for few very first CV cycles, suggesting that the enhancement depends on pretreatment history, which in turn affects the surface composition [133]. For instance,

improvement of OER activity in the $\text{La}_{1-x}\text{Sr}_x\text{CoO}_3$ ($x = 0, 0.3$) system steadily rises with cycling in KOH-based electrolyte deliberately containing 0.1 ppm of Fe_{aq} compared to Fe-free solution, reaching after 1000 cycles the improvement factor of ~ 4 [119], similar to 3.9 in our case. Additionally, the NiO catalyst has also been tested under similar conditions with added $\text{Fe}(\text{NO}_3)_3$ into electrolyte, demonstrating an increase in OER activity by ~ 2.3 times [160].

To test the effect of Fe addition on the long-term stability of LCFN5_m, the electrode consisting of perovskite catalyst mixed with 50 wt.% VC was polarized galvanostatically in a stepwise mode with the 32.6, 56.0, 78.0, 56.0 and 32.6 $\text{A g}^{-1}_{\text{oxide}}$ current densities at least for 14 h (Figure 39a,b). The lower mass loading compared to CV tests was used to maximize the homogeneity of catalyst utilization, i.e. particle wetting and connectivity in the working environment. The relatively low current densities for the stability test were chosen to avoid high overvoltages, causing VC corrosion and oxygen bubble formation during OER.

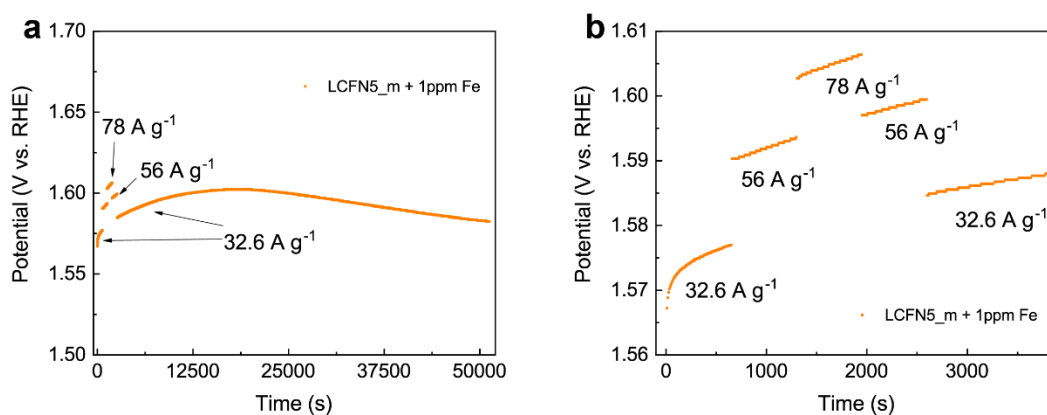


Figure 39. (a) Constant current test on LCFN5_m in 1 ppm Fe_{aq} electrolyte at stepwise changes of the current density from 32.6 to 56.0, 78.0 and back to 56 and 32.6 $\text{A g}^{-1}_{\text{oxide}}$. (b) Enlarged regions of the first 3900 seconds of the test. Ar-saturated 1M NaOH solution, 1600 rpm, mass loading of $18 \mu\text{g cm}^{-2}$, 50 wt.% VC.

The potential slope slightly increases during the constant current test in a stepwise mode at short experimental times (up to 3900 seconds, Figure 39b). Further, the slope continues increasing and finally stabilizes at ~15500 seconds, which suggests the shallow A-cation leaching and restructuring of the surface at the initial stage [161] and then the formation of dynamic equilibrium between Fe dissolution rate from perovskite during OER and redeposition rate promoted by Fe_{aq} in the electrolyte [120],[119]. After 21000 seconds overpotential starts decreasing continuously and this suggests the increase in the number of surface-active centers which enhances the OER activity.

A completely different behavior with a sharp increase in overpotential during continuous galvanostatic polarization for 40 000 seconds was observed for LCFN5_m without the addition of Fe to the electrolyte. In the electrolyte without the intentional addition of Fe ions the potential steadily rises reaching saturation at 40 000 s. This behavior can be associated with the dissolution of Fe from perovskite during OER, which does not redeposit from the electrolyte due to the very low concentrations. Under these conditions, the restructured surface layers are unable to provide sufficient amount of active sites [117],[120], which results in an increase of the overpotential and VC corrosion provoked by high overpotentials [162].

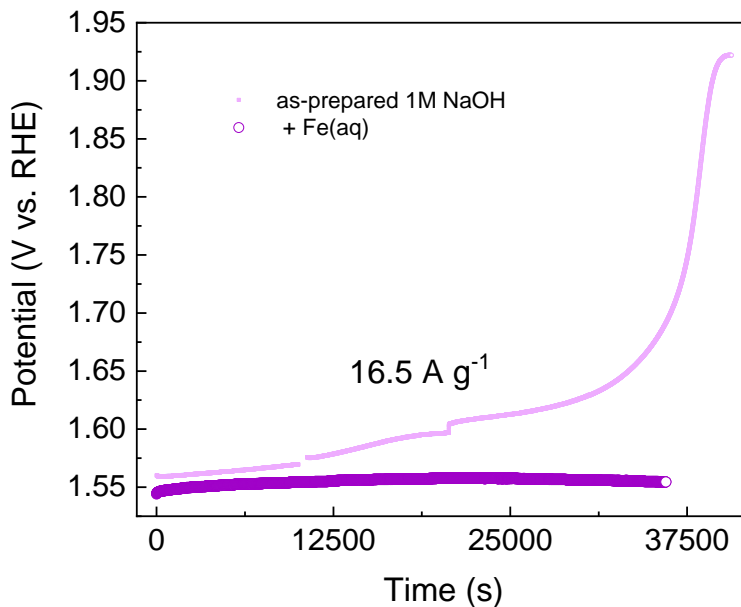


Figure 40. Constant current tests on LCFN5_m in the electrolyte containing ppm amounts of Fe_{aq} (dark line) and in the as-prepared electrolyte (bright line). Ar-saturated 1M NaOH solution, 1600 rpm, mass loading $35.7 \mu\text{g cm}^{-2}$, 50 wt.% VC.

In order to obtain a deeper insight into the changes of the perovskite surface, the LCFN5_m sample was collected directly from the electrode after constant current test. The electrode was rinsed with deionized water, then with isopropanol, and then thin catalyst film was scraped off with a micropipette and further transferred onto the TEM grid.

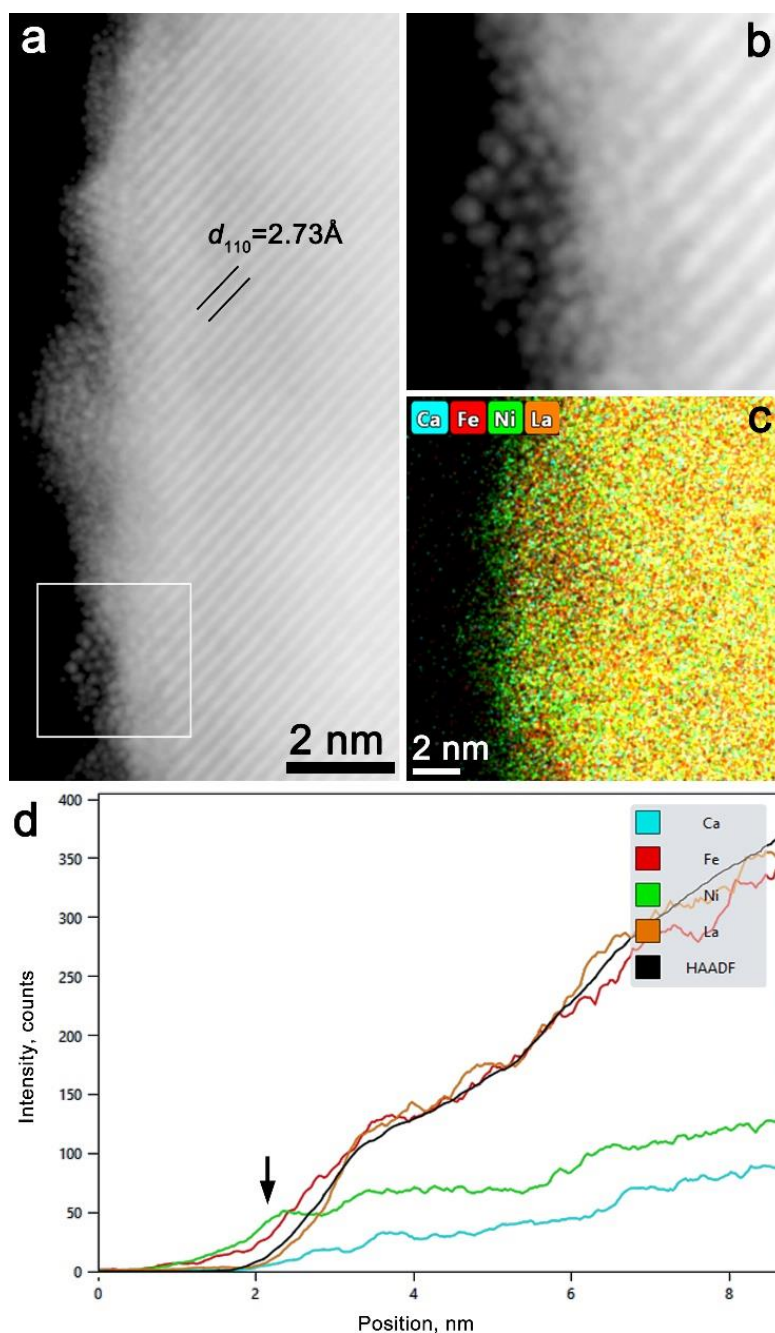


Figure 41. (a) HAADF-STEM image of the near-surface area in the LCFN5_m sample after 14 h constant current test in 1 ppm Fe_{aq} electrolyte. The LCFN5_m particle is visible by traces of the {110} crystal planes of perovskite subcell with $d \approx 2.73 \text{ \AA}$. Restructured surface layer with the thickness of 1-2 nm is visible. (b) Enlargement of the 001-oriented (Ni,Fe) (oxy)hydroxide nanoparticle in the restructured layer. (c,d) EDX-STEM compositional map and intensity profiles demonstrate that the surface layer (marked with arrow) is Ni, Fe – enriched and La, Ca – depleted.

On the very surface of the perovskite particles after the constant current test, a thin restructured layer is observed (Figure 41a). The layer is 1-2 nm thick; it is not entirely amorphous and contains ordered nanoparticles. One of the nanoparticles (outlined in Figure 41a and enlarged in Figure 41b) demonstrates a hexagonal arrangement of cationic columns with variable intercolumn distance with the average value of 2.9(3) Å. This corresponds well to the 001 projection of the $P-3m1$ crystal structure of $\text{Ni}(\text{OH})_2$ layered hydroxide [163]. In fact, the measured projected distance between the cationic columns is in between of those in $\text{Ni}(\text{OH})_2$ (3.13 Å) and in NiOOH (2.81 Å) that reflects that the actual structure is in between of hydroxide and oxyhydroxide. EDX-STEM compositional maps and intensity profiles demonstrate that the surface layer contains both Ni and Fe (Figure 41c,d) with the Ni:Fe ratio of 54(3):46(3). Thus the restructured surface layer can be classified as a mixed $\text{Ni}_{0.5}\text{Fe}_{0.5}\text{O}_x(\text{OH})_{2-x}$ (oxy)hydroxide with variable O/OH ratio. Additionally, to date the isotope labeled Ni- FeO_xH_y systems have not revealed signs of the LOM during OER [164], hence, the restructuring of the perovskite surface with the dissolution of A-site cations and the formation of a Ni-Fe(oxy)hydroxide layer, due to the interaction of B-site cations and Fe ions in the electrolyte suggest that the LOM process does not properly describe the OER mechanism in Ni-Fe perovskite. Thus, the OER mechanism for La-Ca-Fe-Ni perovskite, after the restructuring of the surface perovskite layers, occurs according to AEM (without involving the oxygen atoms of the oxide crystal lattice during reaction).

In conclusion, the Ni-Fe-based perovskite obtained by spray pyrolysis competes with the best catalysts among perovskites and iridium oxides, however, for its stable

long-term operation, the presence of Fe ion impurities in the electrolyte is necessary. This is not a strict restriction for the further design of an electrolysis cell prototype (for example AEMWE) and potential commercial use, since conditions for anode electrocatalyst are now known that will allow to establish high activity and long-term stability. The next stage of optimization should include the selection of a suitable reliable membrane and operating regimes of the electrolyzer (voltage range, temperature, pressure, etc.).

5. Conclusions

- 1) Perovskite material $\text{La}_{0.6}\text{Ca}_{0.4}\text{Fe}_{0.7}\text{Ni}_{0.3}\text{O}_{2.9}$ with surface area as high as $15 \text{ m}^2\text{g}^{-1}$ was successfully synthesized using modified ultrasonic spray pyrolysis, with sorbitol as the fuel and ozone as the oxidizer.
- 2) Analysis of the OER activity of $\text{La}_{1-x}\text{Ca}_x\text{Fe}_{0.7}\text{Ni}_{0.3}\text{O}_{3-\delta}$ ($x=0, 0.3, 0.5$) materials allowed concluding that Ca doping results in an enhancement of the perovskite materials performance in OER, which correlates with a decrease in the oxygen vacancy formation energies for Ca-doped samples. Ca doping provokes major increase in the Ni oxidation state whereas the Fe oxidation state changes to a lesser extent.
- 3) $\text{La}_{0.6}\text{Ca}_{0.4}\text{Fe}_{0.7}\text{Ni}_{0.3}\text{O}_{2.9}$ material (supported on 30 wt.% of VC) with hollow spherical particle morphology, soaked in 1M NaOH, demonstrated record specific and mass activities in OER: $2.4 \text{ mA cm}^{-2}_{\text{oxide}}$ and $400 \text{ A g}^{-1}_{\text{oxide}}$, respectively, at 1.61 V vs RHE and a low Tafel slope of $52.0 \pm 2.6 \text{ mV dec}^{-1}$.
- 4) Electrochemical, XPS, ICP-AES/MS, and HR-TEM data indicate that the enhanced OER activity of $\text{La}_{1-x}\text{Ca}_x\text{Fe}_{0.7}\text{Ni}_{0.3}\text{O}_{3-\delta}$ materials is caused by the formation of catalytically active mixed $\text{Ni}_{0.5}\text{Fe}_{0.5}\text{O}_x(\text{OH})_{2-x}$ (oxy)hydroxide layer on host-perovskite structure under electrocatalytic conditions.
- 5) The presence of Fe in the electrolyte stabilizes the dynamically active OER sites in (oxy)hydroxides and prevents deep structural changes of the perovskite particles through the formation of stable interface with the perovskite catalyst, which ensures the stability of the electrocatalyst during OER.

Appendix

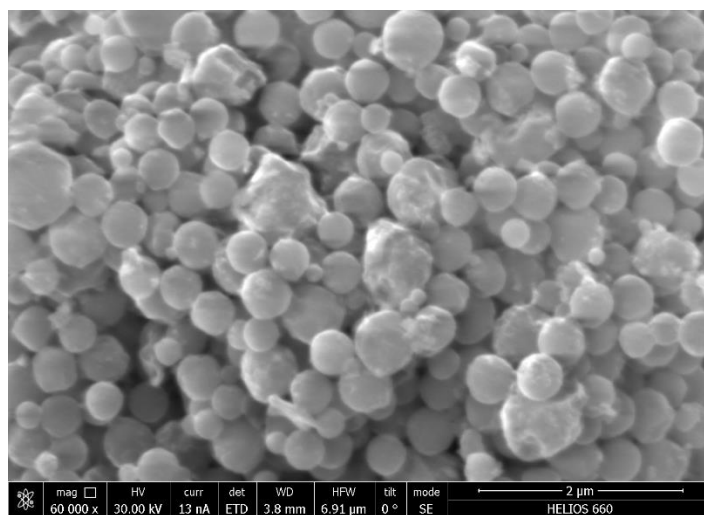


Figure S1. SEM images of spherical particles of the $\text{LaFe}_{0.25}\text{Ni}_{0.75}\text{O}_3$ sample annealed at 600 °C.

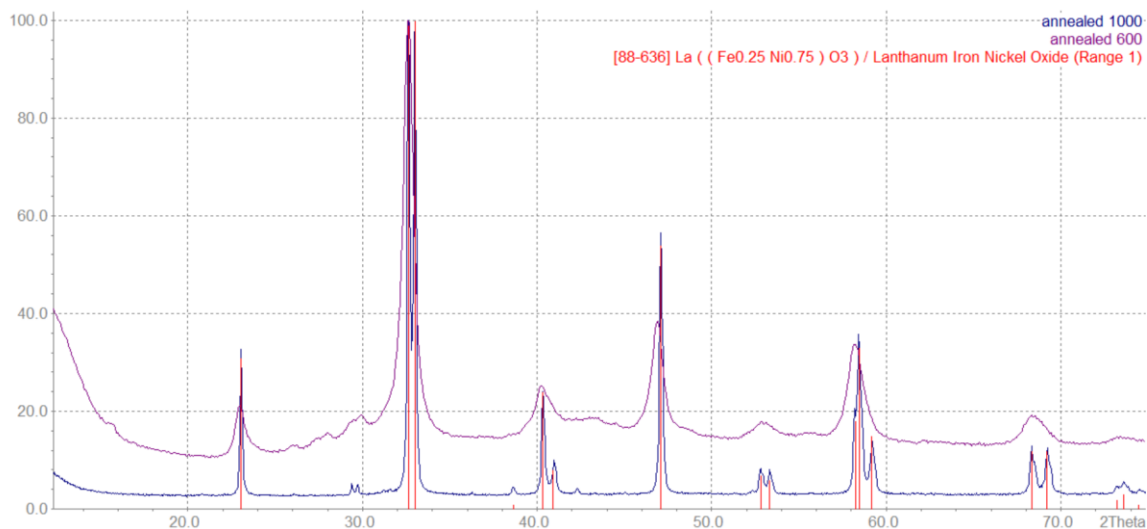


Figure S2. Juxtaposing sample annealed at 1000 and 600 °C. The red lines indicate the PDF 01-088-0636 positions for $\text{LaFe}_{0.25}\text{Ni}_{0.75}\text{O}_3$ (Cu $K_{\alpha 1,2}$ radiation).

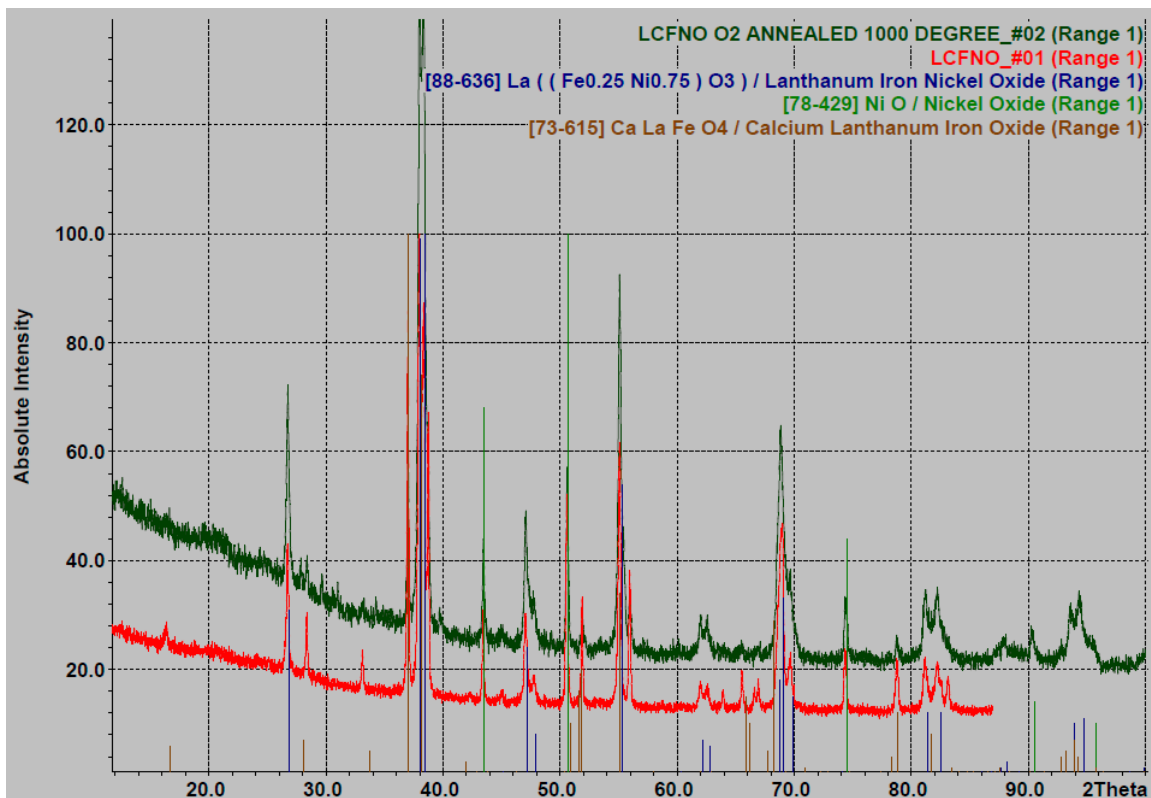


Figure S3. PXR D diffractograms ($\text{Co K}\alpha_1$ radiation) of the $\text{La}_{1-x}\text{Ca}_x\text{Fe}_{0.25}\text{Ni}_{0.75}\text{O}_{3-\delta}$ ($x = 0.2$) sample after 10-hour annealing at 1000 °C (red), and after additional annealing at 1000 °C for 8 hours in an oxygen flow (green).

Calculation of charge from redox transition

To estimate the charge from CV, we integrated the cathodic part of the first scan (Figure S4) and normalized to 10 mV s^{-1} (scan rate), which gives the charge equal $6.35 \mu\text{C}$.

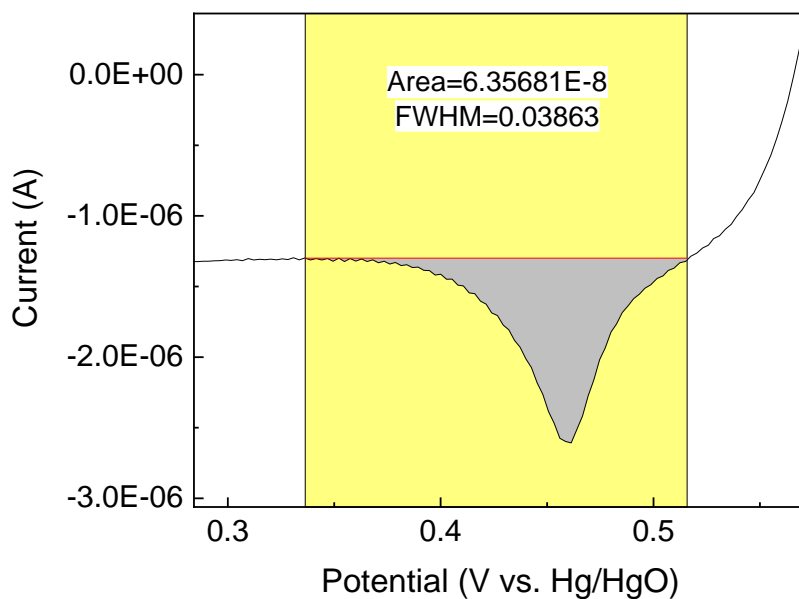


Figure S4. Integration of charge from redox transition, cathodic part of the first scan.

The normalized charge from CV was calculated as:

$$Q = 6.35 \mu\text{C} / (\text{Mass loading}_{\text{perovskite}} * \text{Area}_{\text{electrode}} * S_{\text{BET}}) = 17 \mu\text{C cm}^{-2};$$

The charge was calculated via the equation:

$$Q = z * F * \rho / N_A;$$

where $z = 1$ is the number of electrons transferred,

$$F = 96485.3 \text{ C mol}^{-1},$$

ρ – Ni (110) surface density, atoms cm^{-2} ,

$$N_A = 6.022 \times 10^{23}.$$

$Q = 23.3 \mu\text{C cm}^{-2}$, and if multiplied by $2/3$ (to convert from volume charge density to surface charge density), $Q = 16 \mu\text{C cm}^{-2}$.

Calculation of ECSA from redox transition

The ECSA was calculated via the equation from cathodic peak:

$$S_{ECSA} = \frac{Q}{N_A} / (\text{Mass loading}_{\text{perovskite}} * \text{Area}_{\text{electrode}} * F * \rho);$$

where $Q = 6.35 \mu\text{C}$ charge from CV.

Bibliography

1. Jaśkaniec, S.; Hobbs, C.; Seral-Ascaso, A.; Coelho, J.; Browne, M.P.; Tyndall, D.; Sasaki, T.; Nicolosi, V. Low-temperature synthesis and investigation into the formation mechanism of high quality Ni-Fe layered double hydroxides hexagonal platelets. *Sci. Rep.* **2018**, *8*, 4–11, doi:10.1038/s41598-018-22630-0.
2. Mavrič, A.; Cui, C. Advances and Challenges in Industrial-Scale Water Oxidation on Layered Double Hydroxides. *ACS Appl. Energy Mater.* **2021**, *4*, 12032–12055, doi:10.1021/acsaem.1c02604.
3. Xu, D.; Stevens, M.B.; Cosby, M.R.; Oener, S.Z.; Smith, A.M.; Enman, L.J.; Ayers, K.E.; Capuano, C.B.; Renner, J.N.; Danilovic, N.; et al. Earth-Abundant Oxygen Electrocatalysts for Alkaline Anion-Exchange-Membrane Water Electrolysis: Effects of Catalyst Conductivity and Comparison with Performance in Three-Electrode Cells. *ACS Catal.* **2019**, *9*, 7–15, doi:10.1021/acscatal.8b04001.
4. Burke, M.S.; Enman, L.J.; Batchellor, A.S.; Zou, S.; Boettcher, S.W. Oxygen Evolution Reaction Electrocatalysis on Transition Metal Oxides and (Oxy)hydroxides: Activity Trends and Design Principles. *Chem. Mater.* **2015**, *27*, 7549–7558, doi:10.1021/acs.chemmater.5b03148.
5. Ma, P.; Luo, S.; Luo, Y.; Huang, X.; Yang, M.; Zhao, Z.; Yuan, F.; Chen, M.; Ma, J. Vertically aligned FeOOH nanosheet arrays on alkali-treated nickel foam as highly efficient electrocatalyst for oxygen evolution reaction. *J. Colloid Interface Sci.* **2020**, *574*, 241–250, doi:10.1016/j.jcis.2020.04.058.
6. Xiao, J.; Oliveira, A.M.; Wang, L.; Zhao, Y.; Wang, T.; Wang, J.; Setzler, B.P.; Yan, Y. Water-Fed Hydroxide Exchange Membrane Electrolyzer Enabled by a Fluoride-Incorporated Nickel-Iron Oxyhydroxide Oxygen Evolution Electrode. *ACS Catal.* **2021**, *11*, 264–270, doi:10.1021/acscatal.0c04200.
7. Chatenet, M.; Pollet, B.G.; Dekel, D.R.; Dionigi, F.; Deseure, J.; Millet, P.; Braatz, R.D.; Bazant, M.Z.; Eikerling, M.; Staffell, I.; et al. Water electrolysis: from textbook knowledge to the latest scientific strategies and industrial developments. *Chem. Soc. Rev.* **2022**, doi:10.1039/D0CS01079K.
8. Egelund, S.; Caspersen, M.; Nikiforov, A.; Møller, P. Manufacturing of a LaNiO₃ composite electrode for oxygen evolution in commercial alkaline water electrolysis. *Int. J. Hydrogen Energy* **2016**, *41*, 10152–10160, doi:10.1016/j.ijhydene.2016.05.013.
9. Mefford, J.T.; Rong, X.; Abakumov, A.M.; Hardin, W.G.; Dai, S.; Kolpak, A.M.; Johnston, K.P.; Stevenson, K.J. Water electrolysis on La_{1-x}Sr_xCoO_{3-δ} perovskite electrocatalysts. *Nat. Commun.* **2016**, *7*, 11053, doi:10.1038/ncomms11053.
10. Grimaud, A.; May, K.J.; Carlton, C.E.; Lee, Y.-L.; Risch, M.; Hong, W.T.; Zhou, J.; Shao-Horn, Y. Double perovskites as a family of highly active catalysts for oxygen evolution in alkaline solution. *Nat. Commun.* **2013**, *4*, 2439, doi:10.1038/ncomms3439.
11. Gong, M.; Dai, H. A mini review of NiFe-based materials as highly active oxygen

- evolution reaction electrocatalysts. *Nano Res.* **2015**, *8*, 23–39, doi:10.1007/s12274-014-0591-z.
12. Smith, R.D.L.; Prévot, M.S.; Fagan, R.D.; Zhang, Z.; Sedach, P.A.; Siu, M.K.J.; Trudel, S.; Berlinguette, C.P. Photochemical Route for Accessing Amorphous Metal Oxide Materials for Water Oxidation Catalysis. *Science (80)*. **2013**, *340*, 60–63, doi:10.1126/science.1233638.
 13. Varcoe, J.R.; Atanassov, P.; Dekel, D.R.; Herring, A.M.; Hickner, M.A.; Kohl, P.A.; Kucernak, A.R.; Mustain, W.E.; Nijmeijer, K.; Scott, K.; et al. Anion-exchange membranes in electrochemical energy systems. *Energy Environ. Sci.* **2014**, *7*, 3135–3191, doi:10.1039/C4EE01303D.
 14. Khan, I.; Hou, F.; Le, H.P. The impact of natural resources, energy consumption, and population growth on environmental quality: Fresh evidence from the United States of America. *Sci. Total Environ.* **2021**, *754*, 142222, doi:10.1016/j.scitotenv.2020.142222.
 15. Climate Change: Global Temperature | NOAA Climate.gov Available online: <https://www.climate.gov/news-features/understanding-climate/climate-change-global-temperature> (accessed on Apr 18, 2022).
 16. Hydrogen – Analysis - IEA Available online: <https://www.iea.org/reports/hydrogen> (accessed on Feb 7, 2022).
 17. David, M.; Ocampo-Martínez, C.; Sánchez-Peña, R. Advances in alkaline water electrolyzers: A review. *J. Energy Storage* **2019**, *23*, 392–403, doi:10.1016/j.est.2019.03.001.
 18. Hydrogen Shot Summit. <https://hydrogencouncil.com/en/>.
 19. Programme Review Report 2020-2021 | www.fch.europa.eu.
 20. Lee, B.; Heo, J.; Kim, S.; Sung, C.; Moon, C.; Moon, S.; Lim, H. Economic feasibility studies of high pressure PEM water electrolysis for distributed H₂ refueling stations. *Energy Convers. Manag.* **2018**, *162*, 139–144, doi:10.1016/j.enconman.2018.02.041.
 21. Yu, Z.; Duan, Y.; Feng, X.; Yu, X.; Gao, M.; Yu, S. Clean and Affordable Hydrogen Fuel from Alkaline Water Splitting: Past, Recent Progress, and Future Prospects. *Adv. Mater.* **2021**, *33*, 2007100, doi:10.1002/adma.202007100.
 22. Durst, J.; Siebel, A.; Simon, C.; Hasché, F.; Herranz, J.; Gasteiger, H.A. New insights into the electrochemical hydrogen oxidation and evolution reaction mechanism. *Energy Environ. Sci.* **2014**, *7*, 2255–2260, doi:10.1039/c4ee00440j.
 23. Ledezma-Yanez, I.; Wallace, W.D.Z.; Sebastián-Pascual, P.; Climent, V.; Feliu, J.M.; Koper, M.T.M. Interfacial water reorganization as a pH-dependent descriptor of the hydrogen evolution rate on platinum electrodes. *Nat. Energy* **2017**, *2*, 17031, doi:10.1038/nenergy.2017.31.
 24. Lamy, C.; Millet, P. A critical review on the definitions used to calculate the energy efficiency coefficients of water electrolysis cells working under near ambient temperature conditions. *J. Power Sources* **2020**, *447*, 227350, doi:10.1016/j.jpowsour.2019.227350.
 25. Phillips, R.; Dunnill, C.W. Zero gap alkaline electrolysis cell design for renewable energy storage as hydrogen gas. *RSC Adv.* **2016**, *6*, 100643–100651,

- doi:10.1039/C6RA22242K.
26. Miller, H.A.; Bouzek, K.; Hnat, J.; Loos, S.; Bernäcker, C.I.; Weißgärber, T.; Röntzsch, L.; Meier-Haack, J. Green hydrogen from anion exchange membrane water electrolysis: A review of recent developments in critical materials and operating conditions. *Sustain. Energy Fuels* **2020**, *4*, 2114–2133, doi:10.1039/c9se01240k.
 27. Gutmann, F.; Murphy, O.J. Electrochemical Splitting of Water. *Mod. Asp. Electrochem.* **1983**, 1–82.
 28. Lyons, M.E.G.; Brandon, M.P. The Oxygen Evolution Reaction on Passive Oxide Covered Transition Metal Electrodes in Aqueous Alkaline Solution . Part 1-Nickel. **2008**, *3*, 1386–1424.
 29. Stelmachowski, P.; Duch, J.; Sebastián, D.; Lázaro, M.J.; Kotarba, A. Carbon-based composites as electrocatalysts for oxygen evolution reaction in alkaline media. *Materials (Basel)*. **2021**, *14*, 1–44, doi:10.3390/ma14174984.
 30. Renaud, R.; LeRoy, R. Separator materials for use in alkaline water electrolyzers. *Int. J. Hydrogen Energy* **1982**, *7*, 155–166, doi:10.1016/0360-3199(82)90142-2.
 31. Brauns, J.; Schönebeck, J.; Kraglund, M.R.; Aili, D.; Hnat, J.; Žitka, J.; Mues, W.; Jensen, J.O.; Bouzek, K.; Turek, T. Evaluation of Diaphragms and Membranes as Separators for Alkaline Water Electrolysis. *J. Electrochem. Soc.* **2021**, *168*, 014510, doi:10.1149/1945-7111/abda57.
 32. Henkensmeier, D.; Najibah, M.; Harms, C.; Žitka, J.; Hnat, J.; Bouzek, K. Overview: State-of-the Art Commercial Membranes for Anion Exchange Membrane Water Electrolysis. *J. Electrochem. Energy Convers. Storage* **2021**, *18*, doi:10.1115/1.4047963.
 33. Vincent, I.; Bessarabov, D. Low cost hydrogen production by anion exchange membrane electrolysis: A review. *Renew. Sustain. Energy Rev.* **2018**, *81*, 1690–1704, doi:10.1016/j.rser.2017.05.258.
 34. Manabe, A.; Kashiwase, M.; Hashimoto, T.; Hayashida, T.; Kato, A.; Hirao, K.; Shimomura, I.; Nagashima, I. Basic study of alkaline water electrolysis. *Electrochim. Acta* **2013**, *100*, 249–256, doi:10.1016/j.electacta.2012.12.105.
 35. Cao, X.; Novitski, D.; Holdcroft, S. Visualization of Hydroxide Ion Formation upon Electrolytic Water Splitting in an Anion Exchange Membrane. *ACS Mater. Lett.* **2019**, *1*, 362–366, doi:10.1021/acsmaterialslett.9b00195.
 36. Ayers, K.; Danilovic, N.; Ouimet, R.; Carmo, M.; Pivovar, B.; Bornstein, M. Perspectives on Low-Temperature Electrolysis and Potential for Renewable Hydrogen at Scale. *Annu. Rev. Chem. Biomol. Eng.* **2019**, *10*, 219–239, doi:10.1146/annurev-chembioeng-060718-030241.
 37. Krivina, R.A.; Ou, Y.; Xu, Q.; Twight, L.P.; Stovall, T.N.; Boettcher, S.W. Oxygen Electrocatalysis on Mixed-Metal Oxides/Oxyhydroxides: From Fundamentals to Membrane Electrolyzer Technology. *Accounts Mater. Res.* **2021**, *2*, 548–558, doi:10.1021/accountsmr.1c00087.
 38. Shiva Kumar, S.; Himabindu, V. Hydrogen production by PEM water electrolysis – A review. *Mater. Sci. Energy Technol.* **2019**, *2*, 442–454, doi:10.1016/j.mset.2019.03.002.

39. Lee, J.; Jung, H.; Park, Y.S.; Woo, S.; Kwon, N.; Xing, Y.; Oh, S.H.; Choi, S.M.; Han, J.W.; Lim, B. Corrosion-engineered bimetallic oxide electrode as anode for high-efficiency anion exchange membrane water electrolyzer. *Chem. Eng. J.* **2021**, *420*, doi:10.1016/j.cej.2020.127670.
40. Wu, X.; Scott, K. A Li-doped Co₃O₄ oxygen evolution catalyst for non-precious metal alkaline anion exchange membrane water electrolyzers. *Int. J. Hydrogen Energy* **2013**, *38*, 3123–3129, doi:10.1016/j.ijhydene.2012.12.087.
41. Pavel, C.C.; Cecconi, F.; Emiliani, C.; Santiccioli, S.; Scaffidi, A.; Catanorchi, S.; Comotti, M. Highly Efficient Platinum Group Metal Free Based Membrane-Electrode Assembly for Anion Exchange Membrane Water Electrolysis. *Angew. Chemie Int. Ed.* **2014**, *53*, 1378–1381, doi:10.1002/anie.201308099.
42. GB2589535A ENAPTER PATENT.
43. Gardner, G.; Al-Sharab, J.; Danilovic, N.; Go, Y.B.; Ayers, K.; Greenblatt, M.; Charles Dismukes, G. Structural basis for differing electrocatalytic water oxidation by the cubic, layered and spinel forms of lithium cobalt oxides. *Energy Environ. Sci.* **2016**, *9*, 184–192, doi:10.1039/C5EE02195B.
44. Li, D.; Motz, A.R.; Bae, C.; Fujimoto, C.; Yang, G.; Zhang, F.-Y.; Ayers, K.E.; Kim, Y.S. Durability of anion exchange membrane water electrolyzers. *Energy Environ. Sci.* **2021**, *14*, 3393–3419, doi:10.1039/D0EE04086J.
45. Hans Wedepohl, K. The composition of the continental crust. *Geochim. Cosmochim. Acta* **1995**, *59*, 1217–1232, doi:10.1016/0016-7037(95)00038-2.
46. Live PGM Prices - Price of Iridium, Rhodium, Rhenium & Osmium Available online: <https://www.metalsdaily.com/live-prices/pgms/> (accessed on Jan 31, 2022).
47. Spöri, C.; Kwan, J.T.H.; Bonakdarpour, A.; Wilkinson, D.P.; Strasser, P. The Stability Challenges of Oxygen Evolving Catalysts: Towards a Common Fundamental Understanding and Mitigation of Catalyst Degradation. *Angew. Chemie Int. Ed.* **2017**, *56*, 5994–6021, doi:10.1002/anie.201608601.
48. Man, I.C.; Su, H.; Calle-Vallejo, F.; Hansen, H.A.; Martínez, J.I.; Inoglu, N.G.; Kitchin, J.; Jaramillo, T.F.; Nørskov, J.K.; Rossmeisl, J. Universality in Oxygen Evolution Electrocatalysis on Oxide Surfaces. *ChemCatChem* **2011**, *3*, 1159–1165, doi:10.1002/cctc.201000397.
49. Grimaud, A.; Diaz-Morales, O.; Han, B.; Hong, W.T.; Lee, Y.-L.; Giordano, L.; Stoerzinger, K.A.; Koper, M.T.M.; Shao-Horn, Y. Activating lattice oxygen redox reactions in metal oxides to catalyse oxygen evolution. *Nat. Chem.* **2017**, *9*, 457–465, doi:10.1038/nchem.2695.
50. Jung, S.; McCrory, C.C.L.; Ferrer, I.M.; Peters, J.C.; Jaramillo, T.F. Benchmarking nanoparticulate metal oxide electrocatalysts for the alkaline water oxidation reaction. *J. Mater. Chem. A* **2016**, *4*, 3068–3076, doi:10.1039/c5ta07586f.
51. Yamada, I.; Takamatsu, A.; Asai, K.; Shirakawa, T.; Ohzuku, H.; Seno, A.; Uchimura, T.; Fujii, H.; Kawaguchi, S.; Wada, K.; et al. Systematic Study of Descriptors for Oxygen Evolution Reaction Catalysis in Perovskite Oxides. *J. Phys. Chem. C* **2018**, *122*, 27885–27892, doi:10.1021/acs.jpcc.8b09287.
52. Yamada, I.; Takamatsu, A.; Asai, K.; Ohzuku, H.; Shirakawa, T.; Uchimura, T.;

- Kawaguchi, S.; Tsukasaki, H.; Mori, S.; Wada, K.; et al. Synergistically Enhanced Oxygen Evolution Reaction Catalysis for Multielement Transition-Metal Oxides. *ACS Appl. Energy Mater.* **2018**, *1*, 3711–3721, doi:10.1021/acsaem.8b00511.
53. Zhang, D.; Song, Y.; Du, Z.; Wang, L.; Li, Y.; Goodenough, J.B. Active $\text{LaNi}_{1-x}\text{Fe}_x\text{O}_3$ bifunctional catalysts for air cathodes in alkaline media. *J. Mater. Chem. A* **2015**, *3*, 9421–9426, doi:10.1039/C5TA01005E.
 54. Wang, H.; Wang, J.; Pi, Y.; Shao, Q.; Tan, Y.; Huang, X. Double Perovskite $\text{LaFe}_x\text{Ni}_{1-x}\text{O}_3$ Nanorods Enable Efficient Oxygen Evolution Electrocatalysis. *Angew. Chemie* **2019**, *131*, 2338–2342, doi:10.1002/ange.201812545.
 55. Chen, G.; Zhu, Y.; Chen, H.M.; Hu, Z.; Hung, S.F.; Ma, N.; Dai, J.; Lin, H.J.; Chen, C. Te; Zhou, W.; et al. An Amorphous Nickel–Iron–Based Electrocatalyst with Unusual Local Structures for Ultrafast Oxygen Evolution Reaction. *Adv. Mater.* **2019**, *31*, doi:10.1002/adma.201900883.
 56. Zhu, Y.-X.; Jiang, M.-Y.; Liu, M.; Wu, L.-K.; Hou, G.-Y.; Tang, Y.-P. An Fe–V@NiO heterostructure electrocatalyst towards the oxygen evolution reaction. *Nanoscale* **2020**, *12*, 3803–3811, doi:10.1039/C9NR08749D.
 57. Wang, Y.; Yu, J.; Wang, Y.; Chen, Z.; Dong, L.; Cai, R.; Hong, M.; Long, X.; Yang, S. In situ templating synthesis of mesoporous Ni-Fe electrocatalyst for oxygen evolution reaction. *RSC Adv.* **2020**, *10*, 23321–23330, doi:10.1039/d0ra03111a.
 58. Yuan, S.; Peng, J.; Cai, B.; Huang, Z.; Garcia-Esparza, A.T.; Sokaras, D.; Zhang, Y.; Giordano, L.; Akkiraju, K.; Zhu, Y.G.; et al. Tunable metal hydroxide–organic frameworks for catalysing oxygen evolution. *Nat. Mater.* **2022**, doi:10.1038/s41563-022-01199-0.
 59. Liang, C.; Zou, P.; Nairan, A.; Zhang, Y.; Liu, J.; Liu, K.; Hu, S.; Kang, F.; Fan, H.J.; Yang, C. Exceptional performance of hierarchical Ni-Fe oxyhydroxide@NiFe alloy nanowire array electrocatalysts for large current density water splitting. *Energy Environ. Sci.* **2020**, *13*, 86–95, doi:10.1039/c9ee02388g.
 60. Ma, W.; Ma, R.; Wang, C.; Liang, J.; Liu, X.; Zhou, K.; Sasaki, T. A superlattice of alternately stacked Ni-Fe hydroxide nanosheets and graphene for efficient splitting of water. *ACS Nano* **2015**, *9*, 1977–1984, doi:10.1021/nn5069836.
 61. Louie, M.W.; Bell, A.T. An Investigation of Thin-Film Ni–Fe Oxide Catalysts for the Electrochemical Evolution of Oxygen. *J. Am. Chem. Soc.* **2013**, *135*, 12329–12337, doi:10.1021/ja405351s.
 62. Bates, M.K.; Jia, Q.; Doan, H.; Liang, W.; Mukerjee, S. Charge-Transfer Effects in Ni-Fe and Ni-Fe-Co Mixed-Metal Oxides for the Alkaline Oxygen Evolution Reaction. *ACS Catal.* **2016**, *6*, 155–161, doi:10.1021/acscatal.5b01481.
 63. Yu, M.; Moon, G.; Bill, E.; Tüysüz, H. Optimizing Ni–Fe Oxide Electrocatalysts for Oxygen Evolution Reaction by Using Hard Templating as a Toolbox. *ACS Appl. Energy Mater.* **2019**, *2*, 1199–1209, doi:10.1021/acsaem.8b01769.
 64. Görlin, M.; Chernev, P.; Paciok, P.; Tai, C.W.; Ferreira de Araújo, J.; Reier, T.; Heggen, M.; Dunin-Borkowski, R.; Strasser, P.; Dau, H. Formation of unexpectedly active Ni-Fe oxygen evolution electrocatalysts by physically mixing Ni and Fe oxyhydroxides. *Chem. Commun.* **2019**, *55*, 818–821,

doi:10.1039/c8cc06410e.

65. Xiao, H.; Shin, H.; Goddard, W.A. Synergy between Fe and Ni in the optimal performance of (Ni,Fe)OOH catalysts for the oxygen evolution reaction. *Proc. Natl. Acad. Sci.* **2018**, *115*, 5872–5877, doi:10.1073/pnas.1722034115.
66. Guo, Q.; Li, X.; Wei, H.; Liu, Y.; Li, L.; Yang, X.; Zhang, X.; Liu, H.; Lu, Z. Sr, Fe co-doped perovskite oxides with high performance for oxygen evolution reaction. *Front. Chem.* **2019**, *7*, 1–8, doi:10.3389/fchem.2019.00224.
67. Wang, C.C.; Cheng, Y.; Ianni, E.; Jiang, S.P.; Lin, B. A highly active and stable $\text{La}_{0.5}\text{Sr}_{0.5}\text{Ni}_{0.4}\text{Fe}_{0.6}\text{O}_{3-\delta}$ perovskite electrocatalyst for oxygen evolution reaction in alkaline media. *Electrochim. Acta* **2017**, *246*, 997–1003, doi:10.1016/j.electacta.2017.06.161.
68. Li, M.; Insani, A.R.; Zhuang, L.; Wang, Z.; Rehman, A. ur; Liu, L.X.; Zhu, Z. Strontium-doped lanthanum iron nickelate oxide as highly efficient electrocatalysts for oxygen evolution reaction. *J. Colloid Interface Sci.* **2019**, *553*, 813–819, doi:10.1016/j.jcis.2019.06.054.
69. Wei, C.; Rao, R.R.; Peng, J.; Huang, B.; Stephens, I.E.L.; Risch, M.; Xu, Z.J.; Shao-Horn, Y. Recommended Practices and Benchmark Activity for Hydrogen and Oxygen Electrocatalysis in Water Splitting and Fuel Cells. *Adv. Mater.* **2019**, *31*, 1806296, doi:10.1002/adma.201806296.
70. Filimonenkov, I.S.; Tsirlina, G.A.; Savinova, E.R. Conductive additives for oxide-based OER catalysts: A comparative RRDE study of carbon and silver in alkaline medium. *Electrochim. Acta* **2019**, *319*, 227–236, doi:10.1016/j.electacta.2019.06.154.
71. Hardin, W.G.; Mefford, J.T.; Slanac, D.A.; Patel, B.B.; Wang, X.; Dai, S.; Zhao, X.; Ruoff, R.S.; Johnston, K.P.; Stevenson, K.J. Tuning the Electrocatalytic Activity of Perovskites through Active Site Variation and Support Interactions. *Chem. Mater.* **2014**, *26*, 3368–3376, doi:10.1021/cm403785q.
72. McBean, C.L.; Liu, H.; Scofield, M.E.; Li, L.; Wang, L.; Bernstein, A.; Wong, S.S. Generalizable, Electroless, Template-Assisted Synthesis and Electrocatalytic Mechanistic Understanding of Perovskite LaNiO_3 Nanorods as Viable, Supportless Oxygen Evolution Reaction Catalysts in Alkaline Media. *ACS Appl. Mater. Interfaces* **2017**, *9*, 24634–24648, doi:10.1021/acsami.7b06855.
73. Forslund, R.P.; Hardin, W.G.; Rong, X.; Abakumov, A.M.; Filimonov, D.; Alexander, C.T.; Mefford, J.T.; Iyer, H.; Kolpak, A.M.; Johnston, K.P.; et al. Exceptional electrocatalytic oxygen evolution via tunable charge transfer interactions in $\text{La}_{0.5}\text{Sr}_{1.5}\text{Ni}_{1-x}\text{Fe}_x\text{O}_{4\pm\delta}$ Ruddlesden-Popper oxides. *Nat. Commun.* **2018**, *9*, 3150, doi:10.1038/s41467-018-05600-y.
74. Song, F.; Hu, X. Exfoliation of layered double hydroxides for enhanced oxygen evolution catalysis. *Nat. Commun.* **2014**, *5*, 4477, doi:10.1038/ncomms5477.
75. Soares, C.O.; Silva, R.A.; Carvalho, M.D.; Jorge, M.E.M.; Gomes, A.; Rangel, C.M.; Da Silva Pereira, M.I. Oxide loading effect on the electrochemical performance of LaNiO_3 coatings in alkaline media. *Electrochim. Acta* **2013**, *89*, 106–113, doi:10.1016/j.electacta.2012.11.040.
76. Mohamed, R.; Cheng, X.; Fabbri, E.; Levecque, P.; Kötz, R.; Conrad, O.; Schmidt,

- T.J. Electrocatalysis of Perovskites: The Influence of Carbon on the Oxygen Evolution Activity. *J. Electrochem. Soc.* **2015**, *162*, F579–F586, doi:10.1149/2.0861506jes.
77. Pecchi, G.; Morales, R.; Salinas, D.; Delgado, E.J.; Fierro, J.L.G. Catalytic Performance of $\text{La}_{0.6}\text{Ca}_{0.4}\text{Fe}_{1-x}\text{Ni}_x\text{O}_3$ Perovskites in DME Oxidation. *Mod. Res. Catal.* **2015**, *04*, 97–106, doi:10.4236/mrc.2015.44012.
 78. Cihlar, J.; Vrba, R.; Castkova, K.; Cihlar, J. Effect of transition metal on stability and activity of La-Ca-M-(Al)-O (M = Co, Cr, Fe and Mn) perovskite oxides during partial oxidation of methane. *Int. J. Hydrogen Energy* **2017**, *42*, 19920–19934, doi:10.1016/j.ijhydene.2017.06.075.
 79. Lopez, K.; Park, G.; Sun, H.-J.; An, J.-C.; Eom, S.; Shim, J. Electrochemical characterizations of LaMO_3 (M = Co, Mn, Fe, and Ni) and partially substituted $\text{LaNi}_x\text{M}_{1-x}\text{O}_3$ (x = 0.25 or 0.5) for oxygen reduction and evolution in alkaline solution. *J. Appl. Electrochem.* **2015**, *45*, 313–323, doi:10.1007/s10800-015-0798-z.
 80. Adolphsen, J.Q.; Sudireddy, B.R.; Gil, V.; Chatzichristodoulou, C. Oxygen Evolution Activity and Chemical Stability of Ni and Fe Based Perovskites in Alkaline Media. *J. Electrochem. Soc.* **2018**, *165*, F827–F835, doi:10.1149/2.0911810jes.
 81. Li, M.; Insani, A.R.; Zhuang, L.; Wang, Z.; Rehman, A. ur; Liu, L.X.; Zhu, Z. Strontium-doped lanthanum iron nickelate oxide as highly efficient electrocatalysts for oxygen evolution reaction. *J. Colloid Interface Sci.* **2019**, *553*, 813–819, doi:10.1016/j.jcis.2019.06.054.
 82. Yang, G.; Su, C.; Chen, Y.; Tadé, M.O.; Shao, Z. Nano $\text{La}_{0.6}\text{Ca}_{0.4}\text{Fe}_{0.8}\text{Ni}_{0.2}\text{O}_{3-\delta}$ decorated porous doped ceria as a novel cobalt-free electrode for “symmetrical” solid oxide fuel cells. *J. Mater. Chem. A* **2014**, *2*, 19526–19535, doi:10.1039/c4ta03485f.
 83. Tsai, C.; Dixon, A.G.; Moser, W.R.; Ma, Y.H. Dense perovskite membrane reactors for partial oxidation of methane to syngas. *AIChE J.* **1997**, *43*, 2741–2750, doi:10.1002/aic.690431320.
 84. Shao-Horn et al. US Patent US 10,553,866 B2. **2020**.
 85. Pecchi, G.; Reyes, P.; Zamora, R.; Campos, C.; Cadús, L.E.; Barbero, B.P. Effect of the preparation method on the catalytic activity of $\text{La}_{1-x}\text{Ca}_x\text{FeO}_3$ perovskite-type oxides. *Catal. Today* **2008**, *133–135*, 420–427, doi:10.1016/j.cattod.2007.11.011.
 86. Chen, S.Q.; Li, Y.D.; Liu, Y.; Bai, X. Regenerable and durable catalyst for hydrogen production from ethanol steam reforming. *Int. J. Hydrogen Energy* **2011**, *36*, 5849–5856, doi:10.1016/j.ijhydene.2011.01.126.
 87. Ortiz-Vitoriano, N.; Ruiz de Larramendi, I.; Ruiz de Larramendi, J.I.; Arriortua, M.I.; Rojo, T. Synthesis and electrochemical performance of $\text{La}_{0.6}\text{Ca}_{0.4}\text{Fe}_{1-x}\text{Ni}_x\text{O}_3$ (x = 0.1, 0.2, 0.3) material for solid oxide fuel cell cathode. *J. Power Sources* **2009**, *192*, 63–69, doi:10.1016/j.jpowsour.2008.12.009.
 88. Ortiz-Vitoriano, N.; de Larramendi, I.R.; Cook, S.N.; Burriel, M.; Aguadero, A.; Kilner, J.A.; Rojo, T. The Formation of Performance Enhancing Pseudo-

- Composites in the Highly Active $\text{La}_{1-x}\text{Ca}_x\text{Fe}_{0.8}\text{Ni}_{0.2}\text{O}_3$ System for IT-SOFC Application. *Adv. Funct. Mater.* **2013**, *23*, 5131–5139, doi:10.1002/adfm.201300481.
89. Huang, Y.; Zhang, S.L.; Lu, X.F.; Wu, Z.; Luan, D.; Lou, X.W. (David) Trimetallic Spinel $\text{NiCo}_{2-x}\text{Fe}_x\text{O}_4$ Nanoboxes for Highly Efficient Electrocatalytic Oxygen Evolution. *Angew. Chemie Int. Ed.* **2021**, *60*, 11841–11846, doi:10.1002/anie.202103058.
 90. Feng, J.; Lv, F.; Zhang, W.; Li, P.; Wang, K.; Yang, C.; Wang, B.; Yang, Y.; Zhou, J.; Lin, F.; et al. Iridium-Based Multimetallic Porous Hollow Nanocrystals for Efficient Overall-Water-Splitting Catalysis. *Adv. Mater.* **2017**, *29*, 1–8, doi:10.1002/adma.201703798.
 91. Maiyalagan, T.; Chemelewski, K.R.; Manthiram, A. Role of the Morphology and Surface Planes on the Catalytic Activity of Spinel $\text{LiMn}_{1.5}\text{Ni}_{0.5}\text{O}_4$ for Oxygen Evolution Reaction. *ACS Catal.* **2014**, *4*, 421–425, doi:10.1021/cs400981d.
 92. Deepu, P.; Peng, C.; Moghaddam, S. Dynamics of ultrasonic atomization of droplets. *Exp. Therm. Fluid Sci.* **2018**, *92*, 243–247, doi:10.1016/j.expthermflusci.2017.11.021.
 93. Bang, J.H.; Suslick, K.S. Applications of ultrasound to the synthesis of nanostructured materials. *Adv. Mater.* **2010**, *22*, 1039–1059, doi:10.1002/adma.200904093.
 94. Leng, J.; Wang, Z.; Wang, J.; Wu, H.; Yan, G.; Li, X.; Guo, H.; Liu, Y.; Zhang, Q.; Guo, Z. Advances in nanostructures fabricated via spray pyrolysis and their applications in energy storage and conversion. *Chem. Soc. Rev.* **2019**, *48*, 3015–3072, doi:10.1039/C8CS00904J.
 95. Suh, W.H.; Suslick, K.S. Magnetic and porous nanospheres from ultrasonic spray pyrolysis. *J. Am. Chem. Soc.* **2005**, *127*, 12007–12010, doi:10.1021/ja050693p.
 96. Kodas, T.T.; Hampden-Smith, M.J. *Aerosol Processing of Materials*; Wiley, 1999; ISBN 0471246697.
 97. Robert J. Lang Ultrasonic Atomization of Liquids. *J. Acoust. Soc. Am.* **1962**, *34*, 6–8.
 98. Stopić, S.; Friedrich, B. Synthesis of nanosized metallic and core-shell particles by ultrasonic spray pyrolysis. *Contemp. Mater.* **2017**, *8*, 111–120, doi:10.7251/COMEN1702111S.
 99. Firmansyah, D.A.; Kim, S.-G.; Lee, K.-S.; Zahaf, R.; Kim, Y.H.; Lee, D. Microstructure-Controlled Aerosol–Gel Synthesis of ZnO Quantum Dots Dispersed in SiO_2 Nanospheres. *Langmuir* **2012**, *28*, 2890–2896, doi:10.1021/la203730a.
 100. Atkinson, J.D.; Fortunato, M.E.; Dastgheib, S.A.; Rostam-Abadi, M.; Rood, M.J.; Suslick, K.S. Synthesis and characterization of iron-impregnated porous carbon spheres prepared by ultrasonic spray pyrolysis. *Carbon N. Y.* **2011**, *49*, 587–598, doi:10.1016/j.carbon.2010.10.001.
 101. Rossmeisl, J.; Qu, Z.-W.; Zhu, H.; Kroes, G.-J.; Nørskov, J.K. Electrolysis of water on oxide surfaces. *J. Electroanal. Chem.* **2007**, *607*, 83–89, doi:10.1016/j.jelechem.2006.11.008.

102. Dau, H.; Limberg, C.; Reier, T.; Risch, M.; Roggan, S.; Strasser, P. The Mechanism of Water Oxidation: From Electrolysis via Homogeneous to Biological Catalysis. *ChemCatChem* **2010**, *2*, 724–761, doi:10.1002/cctc.201000126.
103. Rüetschi, P.; Delahay, P. Influence of electrode material on oxygen overvoltage: A theoretical analysis. *J. Chem. Phys.* **1955**, *23*, 556–560, doi:10.1063/1.1742029.
104. Subbaraman, R.; Tripkovic, D.; Chang, K.C.; Strmcnik, D.; Paulikas, A.P.; Hirunsit, P.; Chan, M.; Greeley, J.; Stamenkovic, V.; Markovic, N.M. Trends in activity for the water electrolyser reactions on 3d M(Ni,Co,Fe,Mn) hydr(oxy)oxide catalysts. *Nat. Mater.* **2012**, *11*, 550–557.
105. Trasatti, S. Electrocatalysis in the anodic evolution of oxygen and chlorine. *Electrochim. Acta* **1984**, *29*, 1503–1512, doi:10.1016/0013-4686(84)85004-5.
106. Bockris, J.O.; Otagawa, T. The Electrocatalysis of Oxygen Evolution on Perovskites. *J. Electrochem. Soc.* **1984**, *131*, 290–302, doi:10.1149/1.2115565.
107. Matsumoto, Y.; Sato, E. Electrocatalytic properties of transition metal oxides for oxygen evolution reaction. *Mater. Chem. Phys.* **1986**, *14*, 397–426, doi:10.1016/0254-0584(86)90045-3.
108. Suntivich, J.; May, K.J.; Gasteiger, H.A.; Goodenough, J.B.; Shao-Horn, Y. A Perovskite Oxide Optimized for Oxygen Evolution Catalysis from Molecular Orbital Principles. *Science (80)*. **2011**, *334*, 1383–1385, doi:10.1126/science.1212858.
109. Han, B.; Grimaud, A.; Giordano, L.; Hong, W.T.; Diaz-Morales, O.; Yueh-Lin, L.; Hwang, J.; Charles, N.; Stoerzinger, K.A.; Yang, W.; et al. Iron-Based Perovskites for Catalyzing Oxygen Evolution Reaction. *J. Phys. Chem. C* **2018**, *122*, 8445–8454, doi:10.1021/acs.jpcc.8b01397.
110. Hong, W.T.; Stoerzinger, K.A.; Lee, Y.-L.; Giordano, L.; Grimaud, A.; Johnson, A.M.; Hwang, J.; Crumlin, E.J.; Yang, W.; Shao-Horn, Y. Charge-transfer-energy-dependent oxygen evolution reaction mechanisms for perovskite oxides. *Energy Environ. Sci.* **2017**, *10*, 2190–2200, doi:10.1039/C7EE02052J.
111. Hong, W.T.; Welsch, R.E.; Shao-Horn, Y. Descriptors of Oxygen-Evolution Activity for Oxides: A Statistical Evaluation. *J. Phys. Chem. C* **2016**, *120*, 78–86, doi:10.1021/acs.jpcc.5b10071.
112. Yamada, I.; Kinoshita, M.; Oda, S.; Tsukasaki, H.; Kawaguchi, S.; Oka, K.; Mori, S.; Ikeno, H.; Yagi, S. Enhanced Catalytic Activity and Stability of the Oxygen Evolution Reaction on Tetravalent Mixed Metal Oxide. *Chem. Mater.* **2020**, *32*, 3893–3903, doi:10.1021/acs.chemmater.0c00061.
113. Rong, X.; Parolin, J.; Kolpak, A.M. A Fundamental Relationship between Reaction Mechanism and Stability in Metal Oxide Catalysts for Oxygen Evolution. *ACS Catal.* **2016**, *6*, 1153–1158, doi:10.1021/acscatal.5b02432.
114. Deml, A.M.; Stevanović, V.; Holder, A.M.; Sanders, M.; O’Hayre, R.; Musgrave, C.B. Tunable Oxygen Vacancy Formation Energetics in the Complex Perovskite Oxide $\text{Sr}_x\text{La}_{1-x}\text{Mn}_y\text{Al}_{1-y}\text{O}_3$. *Chem. Mater.* **2014**, *26*, 6595–6602, doi:10.1021/cm5033755.
115. May, K.J.; Carlton, C.E.; Stoerzinger, K.A.; Risch, M.; Suntivich, J.; Lee, Y.-L.; Grimaud, A.; Shao-Horn, Y. Influence of Oxygen Evolution during Water

- Oxidation on the Surface of Perovskite Oxide Catalysts. *J. Phys. Chem. Lett.* **2012**, *3*, 3264–3270, doi:10.1021/jz301414z.
116. Song, J.; Wei, C.; Huang, Z.F.; Liu, C.; Zeng, L.; Wang, X.; Xu, Z.J. A review on fundamentals for designing oxygen evolution electrocatalysts. *Chem. Soc. Rev.* **2020**, *49*, 2196–2214, doi:10.1039/c9cs00607a.
 117. Klaus, S.; Cai, Y.; Louie, M.W.; Trotochaud, L.; Bell, A.T. Effects of Fe Electrolyte Impurities on Ni(OH)₂/NiOOH Structure and Oxygen Evolution Activity. *J. Phys. Chem. C* **2015**, *119*, 7243–7254, doi:10.1021/acs.jpcc.5b00105.
 118. Corrigan, D.A. The Catalysis of the Oxygen Evolution Reaction By Iron Impurities in Thin Film Nickel Oxide Electrodes. *J. Electrochem. Soc.* **1987**, *134*, 337–384.
 119. Lopes, P.P.; Chung, D.Y.; Rui, X.; Zheng, H.; He, H.; Farinazzo Bergamo Dias Martins, P.; Strmcnik, D.; Stamenkovic, V.R.; Zapol, P.; Mitchell, J.F.; et al. Dynamically Stable Active Sites from Surface Evolution of Perovskite Materials during the Oxygen Evolution Reaction. *J. Am. Chem. Soc.* **2021**, *143*, 2741–2750, doi:10.1021/jacs.0c08959.
 120. Chung, D.Y.; Lopes, P.P.; Farinazzo Bergamo Dias Martins, P.; He, H.; Kawaguchi, T.; Zapol, P.; You, H.; Tripkovic, D.; Strmcnik, D.; Zhu, Y.; et al. Dynamic stability of active sites in hydr(oxy)oxides for the oxygen evolution reaction. *Nat. Energy* **2020**, *5*, 222–230, doi:10.1038/s41560-020-0576-y.
 121. Trotochaud, L.; Young, S.L.; Ranney, J.K.; Boettcher, S.W. Nickel–Iron Oxyhydroxide Oxygen-Evolution Electrocatalysts: The Role of Intentional and Incidental Iron Incorporation. *J. Am. Chem. Soc.* **2014**, *136*, 6744–6753, doi:10.1021/ja502379c.
 122. Cheng, X.; Kim, B.-J.; Fabbri, E.; Schmidt, T.J. Co/Fe Oxyhydroxides Supported on Perovskite Oxides as Oxygen Evolution Reaction Catalyst Systems. *ACS Appl. Mater. Interfaces* **2019**, *11*, 34787–34795, doi:10.1021/acsami.9b04456.
 123. Kim, B.-J.; Cheng, X.; Abbott, D.F.; Fabbri, E.; Bozza, F.; Graule, T.; Castelli, I.E.; Wiles, L.; Danilovic, N.; Ayers, K.E.; et al. Highly Active Nanoperovskite Catalysts for Oxygen Evolution Reaction: Insights into Activity and Stability of Ba_{0.5}Sr_{0.5}Co_{0.8}Fe_{0.2}O_{2+δ} and PrBaCo₂O_{5+δ}. *Adv. Funct. Mater.* **2018**, *28*, 1804355, doi:10.1002/adfm.201804355.
 124. Zhu, Y.; Chen, G.; Zhong, Y.; Chen, Y.; Ma, N.; Zhou, W.; Shao, Z. A surface-modified antiperovskite as an electrocatalyst for water oxidation. *Nat. Commun.* **2018**, *9*, 2326, doi:10.1038/s41467-018-04682-y.
 125. Chen, G.; Zhu, Y.; Chen, H.M.; Hu, Z.; Hung, S.; Ma, N.; Dai, J.; Lin, H.; Chen, C.; Zhou, W.; et al. An Amorphous Nickel–Iron-Based Electrocatalyst with Unusual Local Structures for Ultrafast Oxygen Evolution Reaction. *Adv. Mater.* **2019**, *31*, 1900883, doi:10.1002/adma.201900883.
 126. Li, Z.; Lv, L.; Ao, X.; Li, J.G.; Sun, H.; An, P.; Xue, X.; Li, Y.; Liu, M.; Wang, C.; et al. An effective method for enhancing oxygen evolution kinetics of LaMO₃ (M = Ni, Co, Mn) perovskite catalysts and its application to a rechargeable zinc–air battery. *Appl. Catal. B Environ.* **2020**, *262*, doi:10.1016/j.apcatb.2019.118291.
 127. Fabbri, E.; Nachttegaal, M.; Binninger, T.; Cheng, X.; Kim, B.J.; Durst, J.; Bozza,

- F.; Graule, T.; Schäublin, R.; Wiles, L.; et al. Dynamic surface self-reconstruction is the key of highly active perovskite nano-electrocatalysts for water splitting. *Nat. Mater.* **2017**, *16*, 925–931, doi:10.1038/nmat4938.
128. Medway, S.L.; Lucas, C.A.; Kowal, A.; Nichols, R.J.; Johnson, D. In situ studies of the oxidation of nickel electrodes in alkaline solution. *J. Electroanal. Chem.* **2006**, *587*, 172–181, doi:10.1016/j.jelechem.2005.11.013.
129. Hahn, F.; Beden, B.; Croissant, M.J.; Lamy, C. In situ uv visible reflectance spectroscopic investigation of the nickel electrode-alkaline solution interface. *Electrochim. Acta* **1986**, *31*, 335–342, doi:10.1016/0013-4686(86)80087-1.
130. Van der Ven, A.; Morgan, D.; Meng, Y.S.; Ceder, G. Phase Stability of Nickel Hydroxides and Oxyhydroxides. *J. Electrochem. Soc.* **2006**, *153*, A210, doi:10.1149/1.2138572.
131. Dionigi, F.; Zeng, Z.; Sinev, I.; Merzdorf, T.; Deshpande, S.; Lopez, M.B.; Kunze, S.; Zegkinoglou, I.; Sarodnik, H.; Fan, D.; et al. In-situ structure and catalytic mechanism of NiFe and CoFe layered double hydroxides during oxygen evolution. *Nat. Commun.* **2020**, *11*, 1–10, doi:10.1038/s41467-020-16237-1.
132. Juodkazis, K.; Juodkazytė, J.; Vilkauskaitė, R.; Jasulaitienė, V. Nickel surface anodic oxidation and electrocatalysis of oxygen evolution. *J. Solid State Electrochem.* **2008**, *12*, 1469–1479, doi:10.1007/s10008-007-0484-0.
133. Baeumer, C.; Li, J.; Lu, Q.; Liang, A.Y.-L.; Jin, L.; Martins, H.P.; Duchoň, T.; Glöß, M.; Gericke, S.M.; Wohlgemuth, M.A.; et al. Tuning electrochemically driven surface transformation in atomically flat LaNiO₃ thin films for enhanced water electrolysis. *Nat. Mater.* **2021**, *20*, 674–682, doi:10.1038/s41563-020-00877-1.
134. Chen, F.Y.; Wu, Z.Y.; Adler, Z.; Wang, H. Stability challenges of electrocatalytic oxygen evolution reaction: From mechanistic understanding to reactor design. *Joule* **2021**, *5*, 1704–1731, doi:10.1016/j.joule.2021.05.005.
135. Diaz-Morales, O.; Ledezma-Yanez, I.; Koper, M.T.M.; Calle-Vallejo, F. Guidelines for the Rational Design of Ni-Based Double Hydroxide Electrocatalysts for the Oxygen Evolution Reaction. *ACS Catal.* **2015**, *5*, 5380–5387, doi:10.1021/acscatal.5b01638.
136. Burke, M.S.; Zou, S.; Enman, L.J.; Kellon, J.E.; Gabor, C.A.; Pledger, E.; Boettcher, S.W. Revised Oxygen Evolution Reaction Activity Trends for First-Row Transition-Metal (Oxy)hydroxides in Alkaline Media. *J. Phys. Chem. Lett.* **2015**, *6*, 3737–3742, doi:10.1021/acs.jpcllett.5b01650.
137. Samira, S.; Hong, J.; Camayang, J.C.A.; Sun, K.; Hoffman, A.S.; Bare, S.R.; Nikolla, E. Dynamic Surface Reconstruction Unifies the Electrocatalytic Oxygen Evolution Performance of Nonstoichiometric Mixed Metal Oxides. *JACS Au* **2021**, doi:10.1021/jacsau.1c00359.
138. Yagi, S.; Yamada, I.; Tsukasaki, H.; Seno, A.; Murakami, M.; Fujii, H.; Chen, H.; Umezawa, N.; Abe, H.; Nishiyama, N.; et al. Covalency-reinforced oxygen evolution reaction catalyst. *Nat. Commun.* **2015**, *6*, 1–6, doi:10.1038/ncomms9249.
139. Petříček, V.; Dušek, M.; Palatinus, L. Crystallographic Computing System JANA2006: General features. *Zeitschrift für Krist. - Cryst. Mater.* **2014**, *229*, 345–

- 352, doi:10.1515/zkri-2014-1737.
140. Kresse, G.; Furthmüller, J. Efficiency of ab-initio total energy calculations for metals and semiconductors using a plane-wave basis set. *Comput. Mater. Sci.* **1996**, *6*, 15–50, doi:10.1016/0927-0256(96)00008-0.
 141. Aksyonov, D.A.; Fedotov, S.S.; Stevenson, K.J.; Zhugayevych, A. Understanding migration barriers for monovalent ion insertion in transition metal oxide and phosphate based cathode materials: A DFT study. *Comput. Mater. Sci.* **2018**, *154*, 449–458, doi:10.1016/j.commatsci.2018.07.057.
 142. Perdew, J.P.; Burke, K.; Ernzerhof, M. Generalized Gradient Approximation Made Simple. *Phys. Rev. Lett.* **1996**, *77*, 3865–3868, doi:10.1103/PhysRevLett.77.3865.
 143. Dudarev, S.L.; Botton, G.A.; Savrasov, S.Y.; Humphreys, C.J.; Sutton, A.P. Electron-energy-loss spectra and the structural stability of nickel oxide: An LSDA+U study. *Phys. Rev. B* **1998**, *57*, 1505–1509, doi:10.1103/PhysRevB.57.1505.
 144. Javaid, S.; Javed Akhtar, M. Pressure-induced magnetic, structural, and electronic phase transitions in LaFeO₃: A density functional theory (generalized gradient approximation) + U study. *J. Appl. Phys.* **2014**, *116*, 023704, doi:10.1063/1.4887802.
 145. Jain, A.; Hautier, G.; Moore, C.J.; Ping Ong, S.; Fischer, C.C.; Mueller, T.; Persson, K.A.; Ceder, G. A high-throughput infrastructure for density functional theory calculations. *Comput. Mater. Sci.* **2011**, *50*, 2295–2310, doi:10.1016/j.commatsci.2011.02.023.
 146. Shannon, R.D. Revised effective ionic radii and systematic studies of interatomic distances in halides and chalcogenides. *Acta Crystallogr. Sect. A* **1976**, *32*, 751–767, doi:10.1107/S0567739476001551.
 147. Howard, C.J.; Stokes, H.T. Group-Theoretical Analysis of Octahedral Tilting in Perovskites. *Acta Crystallogr. Sect. B Struct. Sci.* **1998**, *54*, 782–789, doi:10.1107/S0108768198004200.
 148. Ohzeki, T.; Hashimoto, T.; Shozugawa, K.; Matsuo, M. Preparation of LaNi_{1-x}Fe_xO₃ single phase and characterization of their phase transition behaviors. *Solid State Ionics* **2010**, *181*, 1771–1782, doi:10.1016/j.ssi.2010.09.041.
 149. Kuznetsov, D.A.; Han, B.; Yu, Y.; Rao, R.R.; Hwang, J.; Román-Leshkov, Y.; Shao-Horn, Y. Tuning Redox Transitions via Inductive Effect in Metal Oxides and Complexes, and Implications in Oxygen Electrocatalysis. *Joule* **2018**, *2*, 225–244, doi:10.1016/j.joule.2017.11.014.
 150. Drevon, D.; Görlin, M.; Chernev, P.; Xi, L.; Dau, H.; Lange, K.M. Uncovering The Role of Oxygen in Ni-Fe(O_xH_y) Electrocatalysts using In situ Soft X-ray Absorption Spectroscopy during the Oxygen Evolution Reaction. *Sci. Rep.* **2019**, *9*, 1532, doi:10.1038/s41598-018-37307-x.
 151. Biesinger, M.C.; Payne, B.P.; Lau, L.W.M.; Gerson, A.; Smart, R.S.C. X-ray photoelectron spectroscopic chemical state quantification of mixed nickel metal, oxide and hydroxide systems. *Surf. Interface Anal.* **2009**, *41*, 324–332, doi:10.1002/sia.3026.
 152. Hubert, M.A.; Patel, A.M.; Gallo, A.; Liu, Y.; Valle, E.; Ben-Naim, M.; Sanchez,

- J.; Sokaras, D.; Sinclair, R.; Nørskov, J.K.; et al. Acidic Oxygen Evolution Reaction Activity–Stability Relationships in Ru-Based Pyrochlores. *ACS Catal.* **2020**, *10*, 12182–12196, doi:10.1021/acscatal.0c02252.
153. Liu, J.; Jia, E.; Stoerzinger, K.A.; Wang, L.; Wang, Y.; Yang, Z.; Shen, D.; Engelhard, M.H.; Bowden, M.E.; Zhu, Z.; et al. Dynamic Lattice Oxygen Participation on Perovskite LaNiO₃ during Oxygen Evolution Reaction. *J. Phys. Chem. C* **2020**, *124*, 15386–15390, doi:10.1021/acs.jpcc.0c04808.
154. Anisimov, V.I.; Bukhvalov, D.; Rice, T.M. Electronic structure of possible nickelate analogs to the cuprates. *Phys. Rev. B* **1999**, *59*, 7901–7906, doi:10.1103/PhysRevB.59.7901.
155. Gou, G.; Grinberg, I.; Rappe, A.M.; Rondinelli, J.M. Lattice normal modes and electronic properties of the correlated metal LaNiO₃. *Phys. Rev. B* **2011**, *84*, 144101, doi:10.1103/PhysRevB.84.144101.
156. Bard, a. J.; Faulkner, L.R. *Electrochemical Methods - Fundamentals and Applications second edition*; 2000; ISBN 3175723993.
157. He, D.; He, G.; Jiang, H.; Chen, Z.; Huang, M. Enhanced durability and activity of the perovskite electrocatalyst Pr_{0.5}Ba_{0.5}CoO_{3-δ} by Ca doping for the oxygen evolution reaction at room temperature. *Chem. Commun.* **2017**, *53*, 5132–5135, doi:10.1039/c7cc00786h.
158. Jin, Y.; Huo, W.; Zhang, L.; Li, Y.; Chen, Q.; Zhang, X.; Yang, S.; Nie, H.; Zhou, X.; Yang, Z. NaBH₄ -reduction induced tunable oxygen vacancies in LaNiO_{2.7} to enhance the oxygen evolution reaction. *Chem. Commun.* **2021**, *57*, 7168–7171, doi:10.1039/D1CC02598H.
159. Kawashima, K.; Márquez-Montes, R.A.; Li, H.; Shin, K.; Cao, C.L.; Vo, K.M.; Son, Y.J.; Wygant, B.R.; Chunangad, A.; Youn, D.H.; et al. Electrochemical behavior of a Ni₃N OER precatalyst in Fe-purified alkaline media: The impact of self-oxidation and Fe incorporation. *Mater. Adv.* **2021**, *2*, 2299–2309, doi:10.1039/d1ma00130b.
160. Nardi, K.L.; Yang, N.; Dickens, C.F.; Strickler, A.L.; Bent, S.F. Creating Highly Active Atomic Layer Deposited NiO Electrocatalysts for the Oxygen Evolution Reaction. *Adv. Energy Mater.* **2015**, *5*, 1–10, doi:10.1002/aenm.201500412.
161. Porokhin, S. V.; Nikitina, V.A.; Aksyonov, D.A.; Filimonov, D.S.; Pazhetnov, E.M.; Mikheev, I. V.; Abakumov, A.M. Mixed-cation perovskite La_{0.6}Ca_{0.4}Fe_{0.7}Ni_{0.3}O_{2.9} as a stable and efficient catalyst for the oxygen evolution reaction. *ACS Catal.* **2021**, *11*, 8338–8348, doi:10.1021/acscatal.1c00796.
162. Filimonenkov, I.S.; Bouillet, C.; Kéranguéven, G.; Simonov, P.A.; Tsirlina, G.A.; Savinova, E.R. Carbon materials as additives to the OER catalysts: RRDE study of carbon corrosion at high anodic potentials. *Electrochim. Acta* **2019**, *321*, doi:10.1016/j.electacta.2019.134657.
163. Kazimirov, V.Y.; Smirnov, M.B.; Bourgeois, L.; Guerlou-Demourgues, L.; Servant, L.; Balagurov, A.M.; Natkaniec, I.; Khasanova, N.R.; Antipov, E. V. Atomic structure and lattice dynamics of Ni and Mg hydroxides. *Solid State Ionics* **2010**, *181*, 1764–1770, doi:10.1016/j.ssi.2010.10.002.
164. Roy, C.; Sebok, B.; Scott, S.B.; Fiordaliso, E.M.; Sørensen, J.E.; Bodin, A.;

Trimarco, D.B.; Damsgaard, C.D.; Vesborg, P.C.K.; Hansen, O.; et al. Impact of nanoparticle size and lattice oxygen on water oxidation on NiFeOxHy. *Nat. Catal.* **2018**, *1*, 820–829, doi:10.1038/s41929-018-0162-x.